UNIVERSITY OF OKLAHOMA
GRADUATE COLLEGE

# OBSERVATIONS AND SIMULATIONS OF A MULTISTATIC WEATHER RADAR NETWORK

A THESIS
SUBMITTED TO THE GRADUATE FACULTY
in partial fulfillment of the requirements for the
Degree of
MASTER OF SCIENCE IN METEOROLOGY

By
SAMUEL WARREN EMMERSON
Norman, Oklahoma
2022

OBSERVATIONS AND SIMULATIONS OF A MULTISTATIC WEATHER RADAR NETWORK

A THESIS APPROVED FOR THE
SCHOOL OF METEOROLOGY

BY THE COMMITTEE CONSISTING OF

Dr. Robert Palmer, Chair

Dr. David Bodine

Dr. Howard Bluestein

Dr. Patrick Skinner

*Dedicated to Nic, Drake, and Gavin*

## Acknowledgments

I would like to extend my gratitude to my advisors, Dr. Bob Palmer and Dr. David Bodine, for their continuous support and for granting me the opportunity to work on such an intellectually stimulating subject. My thanks also go out to the other members of my committee, Dr. Pat Skinner and Dr. Howie Bluestein, for their valuable insights everywhere from research meetings to field deployments. Finally, this work simply could not have been possible without the love and support of my family, both at home and here at OU. It's been a long road through the past two years, but we've weathered the storm and the future is iridescently bright with opportunity.

Funding was provided by NOAA/Office of Oceanic and Atmospheric Research under NOAA–University of Oklahoma Cooperative Agreement #NA21OAR4320204, U.S. Department of Commerce.

# Table of Contents

## List of Tables

# List of Figures

## Abstract

Multistatic radar architectures have the potential to provide a cost-effective source of 3D wind information from both operational and research radars, owing to a system design of one transmitter and several receivers. A prototype multistatic network consisting of two passive receivers and the KTLX WSR-88D has been constructed in the Oklahoma City metropolitan area. To achieve sufficiently precise Doppler frequency estimates while reducing cost, transmitter/receiver synchronization is done through measurements of the WSR-88D's sidelobe radiation, rather than an expensive GPS-based system. This yields an exceptionally simple system capable of producing bistatic moment data with virtually no cooperation from the transmitting radar system.

However, the main factor inhibiting the usage of such systems in 3D dual-Doppler wind retrievals is sidelobe contamination arising from the use of low-gain antennae with broad receive beams. Therefore, mitigation of sidelobe contamination should be paramount for those seeking to use this type of radar system. To this end, simulations of multistatic radar systems with varying receiver network layouts and transmitting techniques are performed to evaluate several strategies for reducing the effects of sidelobe contamination. One such strategy is to simply increase the number of receivers, which is shown to improve retrieval quality, albeit with diminishing returns. Another strategy is sidelobe whitening, which uses varying sidelobe phases to greatly reduce the coherent signal from the sidelobes. This technique

alone is shown to markedly improve measured Doppler velocities and subsequent retrievals, especially in simulations of convective systems. Since sidelobe whitening can only be done with a phased array weather radar, the potential associated with a phased array-bistatic radar system is tremendous, particularly when coupled with the rapid-scan capabilities intrinsic to phased array systems.

Since the initial deployment of the prototype multistatic system, several datasets of severe convection have been collected, including several instances of quasi-linear convective systems (QLCSs) and supercells. Multi-Doppler retrievals done with the multistatic data are able to resolve important structures in the horizontal and vertical wind fields, including mesocyclones and horizontal rotors. These retrievals are shown to be comparable in accuracy to simultaneous multi-Doppler retrievals done with only monostatic radar data, though the deleterious effects of sidelobe contamination are apparent in the multistatic retrievals in some cases.

# Chapter 1

# Introduction

A bistatic multiple-Doppler radar network is comprised of one transmitting Doppler radar and at least one separate passive radar receiver. Past research on these systems in the realm of weather detection began in earnest with Doherty (1964), demonstrating the forward scattering characteristics of varying rain rates in the Rayleigh scattering regime with a narrow-aperture forward-scattering bistatic radar. Later came Atlas et al. (1968); Doviak and Weil (1972); Doviak et al. (1972), who largely focused on the elementary detection of clear-air and weather echoes. Crane (1974) was the first to produce proper Doppler shifts from weather echoes with a bistatic system, laying the groundwork for later Doppler radar systems. All of these systems utilized narrow receive beamwidths, which allowed for high sensitivity to both clear-air and weather echoes, but greatly limited weather surveillance capabilities. The archetypal bistatic system for weather surveillance was outlined by Wurman et al. (1993), which used multiple low-gain receivers to measure apparent Doppler velocities from multiple angles, allowing for the retrieval of the full three-dimensional wind field across a broad volume in convection. Similar systems were developed at McGill University (de Elia, 2000), Deutsches Zentrum für Luft und Raumfahrt (DLR) (Hagen et al., 1999; Friedrich and Caumont, 2003), and the Communications Research Laboratory (CRL) (Nakagawa et al., 2002), with all

systems utilizing two passive receivers alongside a preexisting monostatic radar. However, only a handful of new systems have been developed since the advent of the previously mentioned networks and the networks listed in Wurman et al. (2001). While all of these systems were able to observe many types of weather with much success, the intrinsic limitations and weaknesses of bistatic radars have somewhat tempered the pace of research into these systems. These limitations include spatial variations in range resolution and Doppler shift, lower sensitivity compared to monostatic radars, greater uncertainty in measured Doppler shifts/velocity, difficulty in proper synchronization between transmitter and receiver, and particularly sidelobe contamination. More recently, the efforts from Byrd et al. (2020); Byrd (2020) reinvigorated research in the bistatic weather radar realm by developing an extremely low-cost, bistatic receiver suitable for use with the WSR-88D network and deployed a prototype system around the KTLX WSR-88D radar.

# Chapter 2

# Background

## 2.1 Fundamental Theory of Bistatic Radar

Figure 2.1: Image of the bistatic receiver system at the Radar Innovations Laboratory.

### 2.1.1 Characteristics

Unlike a monostatic radar, a bistatic receiver is spatially separated from the transmitter, meaning that synchronization of the carrier signal between the two is considerably more difficult. The most direct way of achieving synchronization is to physically connect the two, though this is only feasible for systems with extremely short baselines. Otherwise, synchronization can be achieved through interception of the direct-path signal or through reception of a separate synchronization signal (i.e., GPS) (Wurman et al., 1993, 1994). The former method is attractive due to the lack of additional hardware required, but it does introduce additional uncertainty in the received data, especially if the exact transmitting characteristics are unknown. The latter is the preferred method for all of the previously described systems, but it does require modifications to the transmit hardware to incorporate the remote synchronization signal. Wurman et al. (1993) was able to demonstrate both methods, though the GPS-based method was ultimately chosen. It should be noted that timing synchronization must be within $\pm 100$ ns for proper range localization, and frequency coherence must be within $10^{-10}$ of the carrier frequency for proper Doppler frequencies. This high degree of required precision is the primary reason why most bistatic systems use a GPS-based synchronization method (Wurman et al., 1993; George et al., 2006), though Byrd et al. (2020) was able to achieve similar precision with the sidelobe-interception method by leveraging known characteristics of the transmitting radar.

### 2.1.2 Bistatic Spatial Resolution

For a bistatic system with a broad low-gain receiving antenna, the position of a scatterer in space is generally determined by the transmitter pointing angle and the

time delay between transmission and reception, which constrains scatterers onto an ellipsoid intersected by the transmitting beam. It should be noted that the true resolution volume is not this intersection, but rather the full volumetric convolution of the transmitted beam and receiving beam (de Elia, 2000), though the former is generally acceptable for receivers with broad beam widths. The shape of resolution volumes in range varies chiefly due to geometric variations in the measured time delay as the scattering angle decreases from backscattering to forward scattering geometries, where the resolution length degenerates to the baseline length (Wurman et al., 1993; de Elía and Zawadzki, 2001). Otherwise, the overall bistatic resolution volume tends towards twice the volume of a corresponding monostatic resolution volume as range tends to infinity, or conversely as bistatic angle tends to 0° (de Elia, 2000). The same principle also holds in elevation, though this would only be a factor for systems with a non-horizontal baseline and for sweeps at high elevation angles. The variation in range resolution results in geometric dilution of precision, yielding an increase in systematic error (Takaya and Nakazato, 2003), though the full velocity is still theoretically recoverable despite irregular sampling by multiple receiver locations (Soh et al., 2018).

### 2.1.3 Doppler Frequency and Velocity Shift

The nuances of bistatic geometry means that the measured Doppler velocity is not purely radial velocity ($V_r$), but rather the projection of the scatterer motion onto the unit vector formed by the linear combination of the transmitter ($e_{tx}$) and receiver ($e_{rx}$) unit vectors, meaning that measured motion is perpendicular to the range ellipsoids (Figure 2.3). This geometry extends in all three dimensions, thus proper analysis of all motion components of scatterers by a ground-based multi-

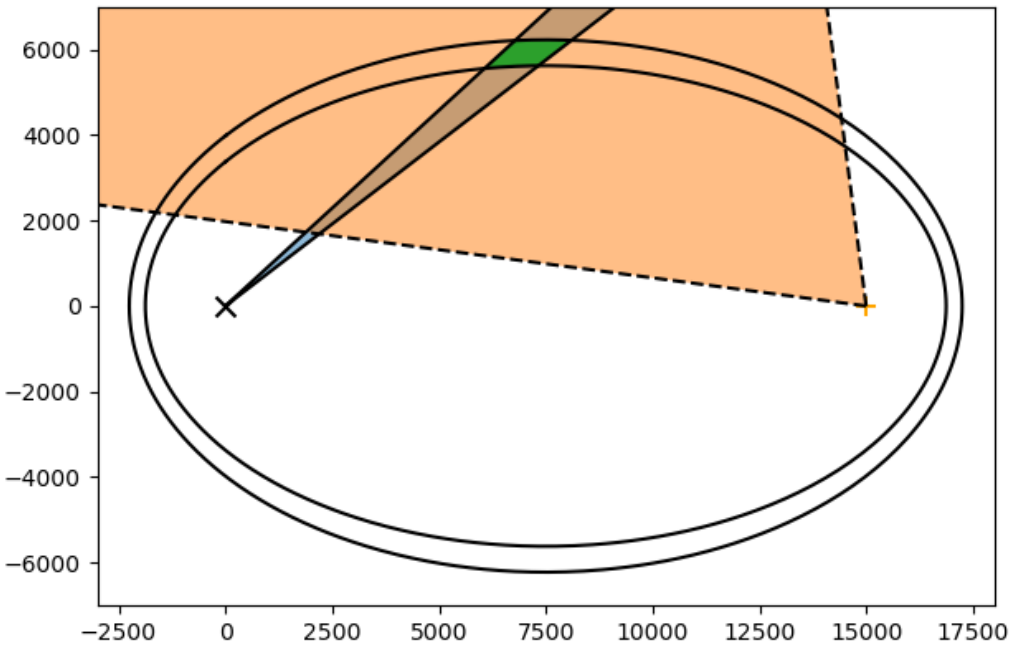


Figure 2.2: Simplified diagram of a bistatic resolution volume (green) as the intersection of constant-phase range ellipses (black), the monostatic one-way transmit beam (blue), and the bistatic receive beam (orange).

static system requires at least 3 independent measurements of apparent velocity at sufficiently high elevation angles (Wurman et al., 1993; Nishimura et al., 2006). The variation in apparent path length with bistatic angle also affects the Doppler Nyquist velocity, which increases from the monostatic Doppler Nyquist velocity at far ranges to effectively infinity at the baseline, since scatterers cannot produce a phase shift wherever the time delay is zero, regardless of their true velocity. Thus, the Doppler Nyquist velocity interval for a bistatic system is *(*always) larger than the corresponding monostatic interval. The spatial variation in unambiguous Doppler velocities stands to be troublesome for dealiasing purposes, but this can be circumvented by instead dealiasing the Doppler frequency shift field (which retains a constant Nyquist interval), then converting to the bistatic Doppler velocity field (Friedrich and Caumont, 2003). A curious application of the improved Nyquist velocities in bistatic configurations could be in the dealiasing of monostatic Doppler velocities, particularly in systems with low Nyquist velocities (i.e., X-band systems). The spatial variation in unambiguous Doppler velocities also naturally extends to the standard error in Doppler velocity, which is given by Equation 2.1 for the monostatic case (Doviak and Zrnić, 1993). The $\frac{1}{\cos\beta/2}$ term means that bistatic systems also contend with higher standard errors in Doppler velocity compared to monostatic systems in addition to the greater spatial uncertainty discussed previously.

$$\sigma_{\hat{V}} = \frac{\lambda}{2\sqrt{M}T_s}\left(\frac{\sigma_{V_{norm}}}{4\sqrt{\pi}} + \frac{2\sigma^2_{V_{norm}}}{SNR} + \frac{1}{12\cdot SNR^2}\right)^{1/2} \tag{2.1}$$

Substituting for bistatic velocity using $V_{bi} = \frac{V_a}{\cos\beta/2}$ yields

$$\sigma_{\hat{V_{bi}}} = \frac{\lambda}{2\sqrt{M}T_s\cos\beta/2}\left(\frac{\sigma_{V_{norm}}}{4\sqrt{\pi}} + \frac{2\sigma^2_{V_{norm}}}{SNR} + \frac{1}{12\cdot SNR^2}\right)^{1/2} \tag{2.2}$$

Thus, the standard error in bistatic velocity increases both with decreasing SNR and increasing bistatic angle, though the former will have a more general impact than the latter. Tulu et al. (2006) showed that SNRs above 0 dB were generally sufficient for uncertainties at or below 1 $\mathrm{m\,s^{-1}}$ across most bistatic geometries outside of near forward-scattering geometries.

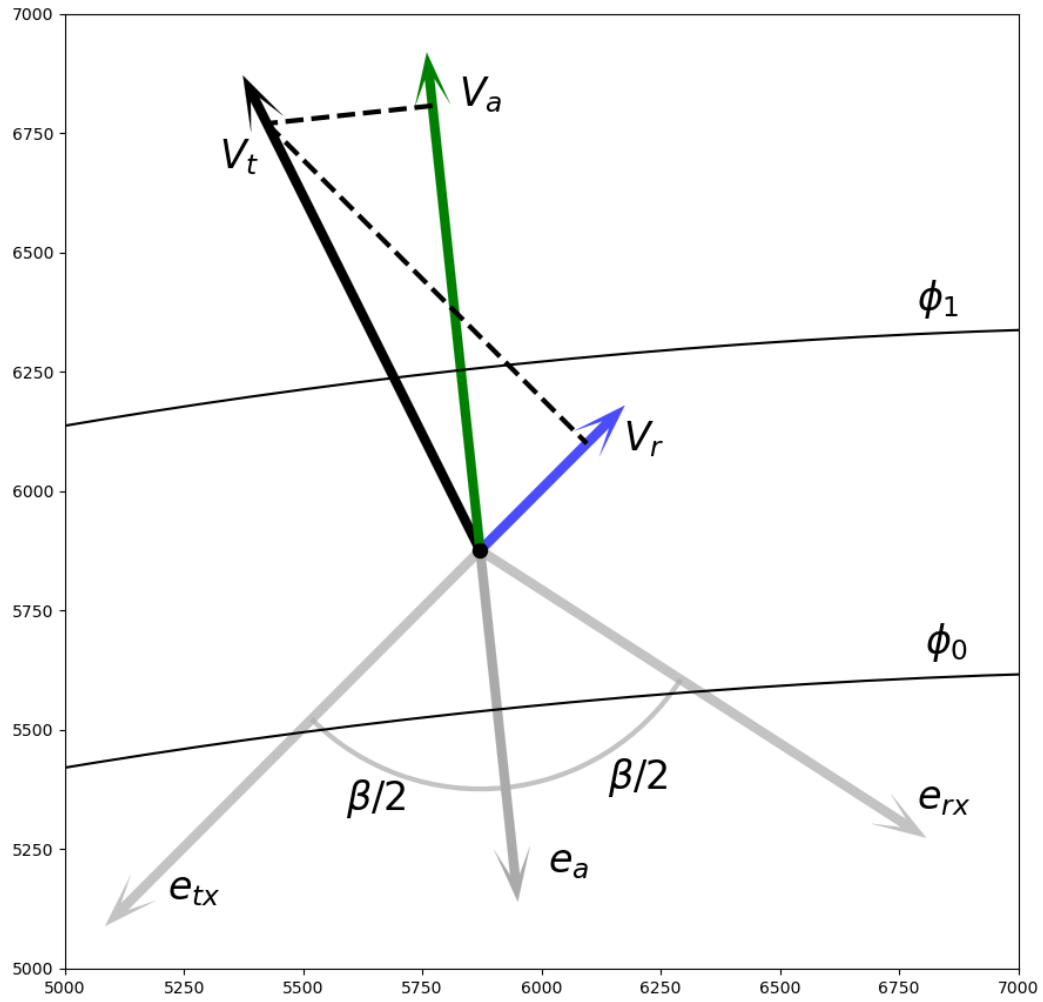


Figure 2.3: A simplified diagram of a bistatic scattering geometry. The radial velocity vector ($V_r$) is given by the projection of the scatterer velocity vector ($V_t$) onto the unit vector pointing towards the transmitter ($e_{tx}$), while the apparent bistatic velocity vector ($V_a$) is given by the projection onto the gradient of the path length ($e_a$), which is always orthogonal to ellipses of constant range ($\phi_0$, $\phi_1$).

Another issue unique to bistatic systems is proper phase control relative to the transmitter, since both relative motion of the transmitting antenna's phase center Byrd et al. (2020) and imperfections in the phase pattern of the antenna Feng and Fabry (2016) can introduce large errors in the measured Doppler frequency shift and velocity. In addition, any phase coding applied to the transmitted pulse train (i.e., SZ-2 Sachidananda and Zrnic (1999) for the WSR-88D) must be properly decoded on receive for proper frequency coherence.

### 2.1.4 Sensitivity and Polarization

For Rayleigh scattering, the intensity of scattered radiation can be generalized as a simple function of the incoming radiation intensity and the angle between the incident electric field vector and the propagation vector of the scattered radiation, which manifests as a toroidal region about the scatterer oriented perpendicular to the polarization vector of the incoming radiation. This means that vertically polarized transmissions have essentially isotropic scattering in the horizontal plane, while horizontal polarization varies from zero scattering at angles around 90 degrees to full scattering in the forward and backscattering geometries. It is for this reason that all bistatic radar systems employ vertically-polarized transmissions and receive antennae, since horizontally polarized transmissions would have a "notch" of negligible returns around a bistatic angle of $90^\circ$ , forming broad arcs between the transmitter and receiver. Likewise, the notch for vertical polarization extends in a vertical arc, with little effect at low elevation angles. This is also a reason why bistatic radars have generally lagged behind monostatic radars, since vertical polarization in monostatic radars was generally not widely implemented until dual-polarization came to maturity. Even with vertically-polarized transmissions

and Rayleigh scatterers, bistatic radars generally have worse sensitivity than monostatic radars, as bistatics typically employ low-gain receive antennae with large beamwidths to simplify receiving operations. However, the primary objective for bistatic radars is to measure Doppler velocity rather than received power, and the former can be reasonably estimated at an SNR of 0 dB (Wurman et al., 1993; Tulu et al., 2006), meaning that sensitivity is not as critical.

Of course, all of these considerations apply only under Rayleigh scattering conditions, which would not be met for S-band systems observing large hail, or for higher frequency systems observing large raindrops Aydin et al. (1998). As a result, areas of hail would have noticeably different patterns in received power at horizontal polarization, which Wurman et al. (1993) and Aydin et al. (1998) suggest could be used for effective hail discrimination. Further, if both vertical and horizontal polarization echoes are detected from multiple angles, then a multitude of polarimetric measurements would be possible, which could allow for sophisticated hydrometeor classification techniques, as well as quantitative precipitation estimates. Aydin et al. (1998) demonstrated that the bistatic-to-backscatter ratio (BBR) was mostly independent of variations in axial ratio and orientation of raindrops and hailstones, providing a potentially robust method of estimating $D_0$. Dibbern (1987) demonstrated that the best bistatic angles for determining drop size distribution parameters using polarimetric measurements were between 90–100$^\circ$ , which also roughly correspond to the most effective angles for 3D wind retrievals. Thus, a polarmetric multistatic system could provide simultaneous dynamical and microphysical retrievals on timescales determined by the volumetric scanning capability of the transmitting monostatic radar system. However, a truly polarimetric bistatic system has yet to be demonstrated.

### 2.1.5 Sidelobe Contamination

For a monostatic radar with a high-gain antenna, the return power from sidelobes are generally negligible for most situations. However, the wide viewing angle and scattering geometry of typical bistatic antennae means that they are susceptible to multiple scattering and sidelobe contamination (SICO). Put in terms of antenna patterns, the monostatic receiving case is described by the two-way antenna pattern, but the bistatic receiving case over a given area within the broad main lobe would have a nearly isotropic receive pattern, so the effective two-way pattern is proportional to the one-way pattern. The net result of this is that the returned power from sidelobes is twice as intense. To properly calibrate received bistatic power to equivalent reflectivity, the receive antenna pattern would have to be known *a priori* (de Elía and Zawadzki, 2000). For echoes with small spatial extent within the main lobe of the receive pattern, the received power is essentially matched to the monostatic power, assuming the pattern is relatively uniform in the region. For echoes with a large spatial extent, the decrease in power associated with rolloff in the antenna pattern are apparent, but are typically left uncorrected due to computation complexities of estimating the true size of the bistatic resolution volumes. The effect of the first sidelobe coupling are usually seen in regions with a strong radial gradient in reflectivity (i.e., convection), typically manifesting as an azimuthally-aligned flare echo. However, the sidelobe returns also bleed into the true weather echo, contaminating the Doppler spectrum. The effects of this contamination can be quite severe in regions with strong gradients in reflectivity and velocity, resulting in dire implications for any dual-Doppler retrievals. Wurman et al. (1993) also discusses the possibility of multipath scattering in bistatic systems, where the transmitted signal is obliquely scattered multiple times in areas of high reflectivity before propagating

to the receive antenna. At S-band, the proportion of reflected energy (and resultant echo power) from this process would be exceedingly small, but it is shown to become problematic at smaller wavelengths as a larger proportion of energy is scattered back to the receiver. In addition, hail and other non-Rayleigh scatterers would likely be more efficient at this process.

### 2.1.6 Bistatic Multi-Doppler Retrievals

Using modified dual-Doppler equations (Wurman et al., 1993; Byrd et al., 2020), the procedure for retrieving 3D winds from bistatic and monostatic data is shown in Equation 2.3, where $\phi$ and $\theta$ denote the azimuthal and elevation angles from receiver $rn$ or the transmitter $t$, $\beta$ denotes the bistatic angle, $v_rn$ denotes the bistatic velocity, and $v_t$ denotes the monostatic radial velocity.

$$\begin{bmatrix} \frac{\sin\phi_{r1}\cos\theta_{r1}+\sin\phi_t\cos\theta_t}{2\cos\beta_1/2} & \frac{\cos\phi_{r1}\cos\theta_{r1}+\cos\phi_t\cos\theta_t}{2\cos\beta_1/2} & \frac{\sin\phi_{r1}+\sin\phi_t}{2\cos\beta_1/2} \\ \frac{\sin\phi_{r2}\cos\theta_{r2}+\sin\phi_t\cos\theta_t}{2\cos\beta_2/2} & \frac{\cos\phi_{r2}\cos\theta_{r2}+\cos\phi_t\cos\theta_t}{2\cos\beta_2/2} & \frac{\sin\phi_{r_2}+\sin\phi_t}{2\cos\beta_1/2} \\ \vdots & \vdots & \vdots \\ \sin\phi_t\cos\theta_t & \cos\phi_t\cos\theta_t & \sin\phi_t \end{bmatrix} \begin{bmatrix} u \\ v \\ w \end{bmatrix} = \begin{bmatrix} v_{r1} \\ v_{r2} \\ \vdots \\ v_t \end{bmatrix} \tag{2.3}$$

The intrinsic uncertainty in velocities from bistatic systems due to variations in receive geometries means that a retrieval from a bistatic system will have approximately double the uncertainty of a similar monostatic retrieval (Wurman et al., 1993; Takaya and Nakazato, 2002). This is due to uncertainty in both the transmitting pointing angle and the bistatic angle, which combine to produce an anisotropy in the error field of bistatic dual-Doppler fields (Takaya and Nakazato, 2003). As noted before, the resolution volumes from a bistatic system have considerable spatial variability, both across a single bistatic sweep and on a receiver-to-receiver

basis for a given bin. As a result, the gates must be analyzed to a common Cartesian grid before any dual-Doppler analysis is done. If data are available from more than one bistatic receiver, then the full reflectivity-weighted particle velocity field can be retrieved Testud and Chong (1983). Further, if data from many receivers is available, then the system of equations becomes overdetermined and the field can be estimated via error minimization (Soh et al., 2018). However, the direct determination of $w$ at low elevation angles is generally intractable for ground-based radar networks, since a small component of $w$ is resolved at such angles. Instead, $w$ must be derived either from vertical integration of the continuity equation or through variational techniques (Protat and Zawadzki, 1999). A notable advantage of bistatic multi-Doppler networks over similar monostatic networks is the simultaneity of observations, since bistatic networks use a single source of illumination. As a result, monostatic networks typically have poor temporal resolution in 2D/3D wind syntheses, owing to the need for temporal interpolation between individual monostatic volumes. On the other hand, bistatic networks are only limited in temporal resolution by the scanning rate of the transmitter. Given the advent of rapidly-scanning phased array weather radars, it's evident that bistatic systems have incredible potential in conjunction with these systems in the near future.

## 2.2 Reduction of Sidelobe Contamination

de Elía and Zawadzki (2000) explored the previously discussed factors as how they relate to the optimal layout of a bistatic network through simulations of a preexisting network. In general, first-order sidelobe contamination is maximized in close proximity to the baseline, while received power is highest near the receiver Wurman et al. (1993). As a result, the location index defined by these factors is highest in

an arc along a region corresponding to $\beta = 90°$–$100°$. To test the effectiveness of this location index, a simulated convective cell is observed with varying numbers of receivers across all possible positions given a fixed transmitter. It is demonstrated that a single receiver is capable of providing effective coverage over the convective cell, albeit with some sidelobe contamination. The notable finding is that placing an additional receiver into this network leads to little improvement in terms of the number of gates affected by sidelobe contamination, regardless of location. However, it should be noted that the metric for improvement was simply the coverage of gates with a threshold amount of returned sidelobe power, rather than any improvement in the Doppler velocity or wind retrieval over the region of interest. In addition, there was no attempt to simultaneously optimize the placement of both receivers. This does raise some questions about the generality of these results, since the region of interest is relatively small compared to the surveillance domain of the transmitting radar. Instead, the authors suggest that the optimal strategy for observing a larger domain of interest is to split the domain into smaller storm-scale domains, then position receivers such that each subdomain has an "optimal" combination of two receivers. However, Ray and Sangren (1983) noted that this strategy is generally suboptimal compared to a simultaneous optimization of an entire network.

Sidelobe whitening is a method introduced by Sachidananda et al. (1985) to "whiten" the sidelobe pattern on transmit for phased array weather radars, varying the amplitude and phase of the sidelobe regions while leaving the main lobe untouched, resulting in a generally incoherent sidelobe signal and coherent main beam signal. The resulting spectral moments would not be biased, but would have greater standard error compared to the unwhitened moments. In essence, this spreads the coherent sidelobe signal into the entire incoherent Doppler spectrum, thereby greatly reducing the amount of sidelobe present in the coherent signal. Ideally, the

transmission of $M$ pulses would have $M$ designed transmit patterns, but it is not typically feasible to do so for large values of $M$ (i.e., 40–64 for current WSR-88D VCPs (ROC, 2021). However, using just 2 transmit patterns with antisymmetric sidelobe phases, a whitening power of –17.8 dB is achievable. This degree of improvement is hard to overlook, especially considering the fact that the main beam remains fixed in width. Taking into account that sidelobe whitening is only possible with phased array radars, the potential of bistatic systems with rapidly-scanning phased arrays appears greater and greater.

While it is possible to reject spurious sidelobe echoes with little effort, correcting true meteorological echoes with additional sidelobe contamination is much more difficult. Chong et al. (2008) proposed a variational method of correcting the observed bistatic Doppler velocity using both bistatic and monostatic reflectivity and velocity. However, such a technique would not necessarily be feasible for real-time applications, since it is possible that AI/ML methods could be used to detect areas of pure sidelobe contamination and possibly correct meteorological echoes as well. A spectral-based method could also be used by detecting bins of pure sidelobe contamination, estimating the location of the dominant meteorological echo causing it, and gradually removing the sidelobe portion of the spectrum from the meteorological echoes, restoring the Doppler velocity estimates to some degree.

## 2.3 Motivation

The recent development of a low-cost passive receiver design for use with essentially any pulse-Doppler weather radar by Byrd et al. (2020) implies the ability to easily field a large network of bistatic receivers about any in-band radar capable of transmitting pointing angle information. A prototype network of two such re-

ceivers has been constructed, but the accuracy of the retrieved 2D and 3D wind fields in convection have not been validated. In addition, while de Elía and Zawadzki (2000) found that there is little advantage to having more than two bistatic receivers for a storm-scale region of interest, it remains to be seen what number of bistatic receivers would be most effective for a domain encompassing the transmitting radar's surveillance area, what the layout for that network would be, and how the network could be arranged to reduce the effects of sidelobe contamination. Byrd (2020) investigated the prospects of sidelobe whitening for reducing sidelobe contamination to some degree, but did not quantify how much benefit sidelobe whitening could bring to bistatic networks, particularly for networks with a large number of receivers and how these improvements impact any incipient wind retrievals. Further, the ability to leverage the intrinsic spatial diversity of multistatic networks within the multi-Doppler retrieval process has yet to be explored, as all previous studies have assumed that the optimal method would be to include data from all receivers in an over-determined retrieval. This presents another opportunity to suppress sidelobe contamination via exclusion of data with poor viewing angles, potentially improving retrievals without any modifications to the system hardware.

This work seeks to broadly investigate these questions via experimentation on varying multistatic radar networks. Several sets of simulations are conducted to assess the sensitivity of multistatic multi-Doppler retrievals to the number of deployed receivers, the transmitted beam pattern, and the method of data exclcusion based on scattering geometry. Further, the general accuracy of 2D and 3D wind retrievals from the current prototype network is demonstrated to provide a baseline for the capabilities of a minimal multistatic network.

# Chapter 3

# Methods

## 3.1 Simulations

Given that several of the previous hypotheses require a large amount of yet-to-be built hardware to be tested in the real atmosphere, we will instead explore these with a multistatic radar simulation framework capable of incorporating varying strategies on transmit and receive. The simulator largely resembles that of Byrd et al. (2016); Byrd (2020), a Monte Carlo format where point scatterers are randomly distributed within the simulation domain. The meteorological variables ($u$,$v$,$w$,Z) are prescribed by model inputs from Cloud Model 1 (CM1) Bryan and Fritsch (2002), and are interpolated onto each scatterer. The input for the convective simulations is a 250 m isotropic CM1 simulation of an intense supercell. The configuration for this simulation is provided in Table 3.1. The base state for the simulation is from the 21 May 2019 00Z observed sounding from KOUN (Figure 3.1), while the sensitivity tests use uniform or patterned fields of $u$, $v$, $w$, and reflectivity. The I/Q data are computed for each scatterer through application of the bistatic radar equation, then summed to form a received signal at each receiver position. The simulator assumes no advection (i.e., weather is static) and dwell times are instantaneous. The antenna patterns for both transmit and receive are configurable. For our

| | |
|---|---|
| Grid points | 480x480x70 |
| Domain extent | 120 km x 120 km x 17.5 km |
| Grid spacing | $\Delta x, \Delta y, \Delta z = 250m$ |
| Microphysics | NSSL 2-moment |
| Initialization | 5 K warm bubble |

Table 3.1: CM1 configuration for the supercell simulation.

simulations, we have an approximation of a WSR-88D parabolic dish pattern with pronounced sidelobes (Figure 3.2), an equivalent-sized phased array pattern with unwhitened and whitened sidelobes (Figure 3.4), and an ideal pencil-beam pattern with no sidelobes (Figure 3.3). The phased array pattern has somewhat reduced sidelobes compared to the dish pattern, but both have the same effective aperture, so the results should be somewhat comparable with respect to a current WSR-88D system vs. a future optimized PAWR. Sidelobe whitening of the PAWR pattern is achieved via random selection of one of the 4 transmit phase patterns shown in Figure 3.5. The ideal pattern serves as a baseline both for interpretation of the degree of sidelobe contamination, and for the accuracy of the dual-Doppler syntheses. The antenna pattern for the simulated bistatic receivers is shown in Figure 3.6. This pattern is extremely broad in azimuth, even more so than the actual antennae used in the prototype system. However, this is acceptable for our purposes given that antenna positioning in azimuth is a relatively simple endeavor compared to proper network design.

The radar cross section in both polarizations is given by interpolation of pre-computed scattering tables for water and spongy ice spheroids Bohren and Battan (1982) using the T-matrix method Waterman (1965) implemented in Python via the pytmatrix package Leinonen (2014), rather than direct computation of Rayleigh scattering amplitudes as others (de Elía and Zawadzki (2000); Byrd et al. (2016,

2020)) have done in the past. This is justified because bistatic receivers are typically confined to convective observations due to low sensitivity, meaning that hydrometeors with non-Rayleigh scattering characteristics (large raindrops, hail, etc.) are more likely to be observed and would likely contribute to sidelobe contamination in many cases. Shedd et al. (2021) demonstrated the general tendency of hailstones to become more oblate and irregular in shape with increasing major axis length, implying more irregular Mie scattering characteristics, even at S-band frequencies. These resonance effects are more prevalent at higher frequencies (Kumjian et al., 2018), so inclusion of these scattering calculations is paramount. The effects of attenuation are neglected for our purposes, since the transmitting radar is S-band and thus would have minimal attenuation in most cases. However, the inclusion of bistatic path attenuation will likely be needed for simulations of higher frequency systems involving intense convection, as such systems would likely have severe attenuation. It is extremely likely that attempts at optimizing the layout of C-band or X-band networks would need to strongly consider the effects of attenuation given the use of low-gain antennae.

A major factor in the quality of bistatic observations is the position of the receiver. Thus, the positions of the simulated receiver networks are carefully controlled since they play a significant role in the bistatic observables and subsequent retrievals. To test the sensitivity of a bistatic network to increases in the number of receivers, the positions of the receivers must be roughly isotropic with respect to the transmitter while retaining multi-Doppler coverage over the domain of interest. A crude genetic algorithm, implemented in Python, using the bistatic location index (Equation 3.5) as a gain function was used to determine a general configuration for the receiver count sensitivity test. The best configuration for this test was found to be an equidistant locus of receivers around the transmitter, with the number of re-

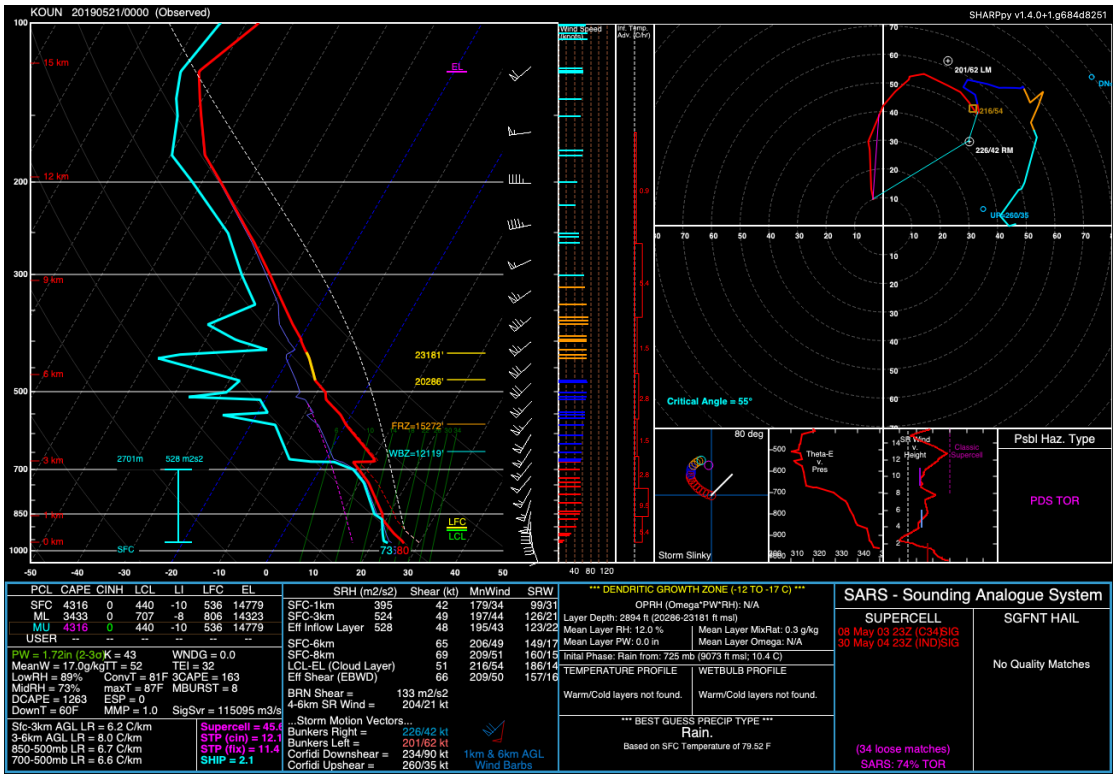


Figure 3.1: Base state sounding for the simulated supercell in CM1.

ceivers varying from 3 to 16. For the beam pattern tests with simulated convection, the receiver positions are nearly identical to those of the prototype system, with two receivers positioned SW and NW of the transmitter on 20 km baselines. Finally, to test the expansion of such a system, an additional four receivers are placed within the previous network, two equally spaced along each existing baseline. The transmitter configuration for all simulations practically matches a conventional WSR-88D in VCP 212 (ROC, 2021) at the lowest tilt ($0.5°$), aside from the variations in beam pattern.

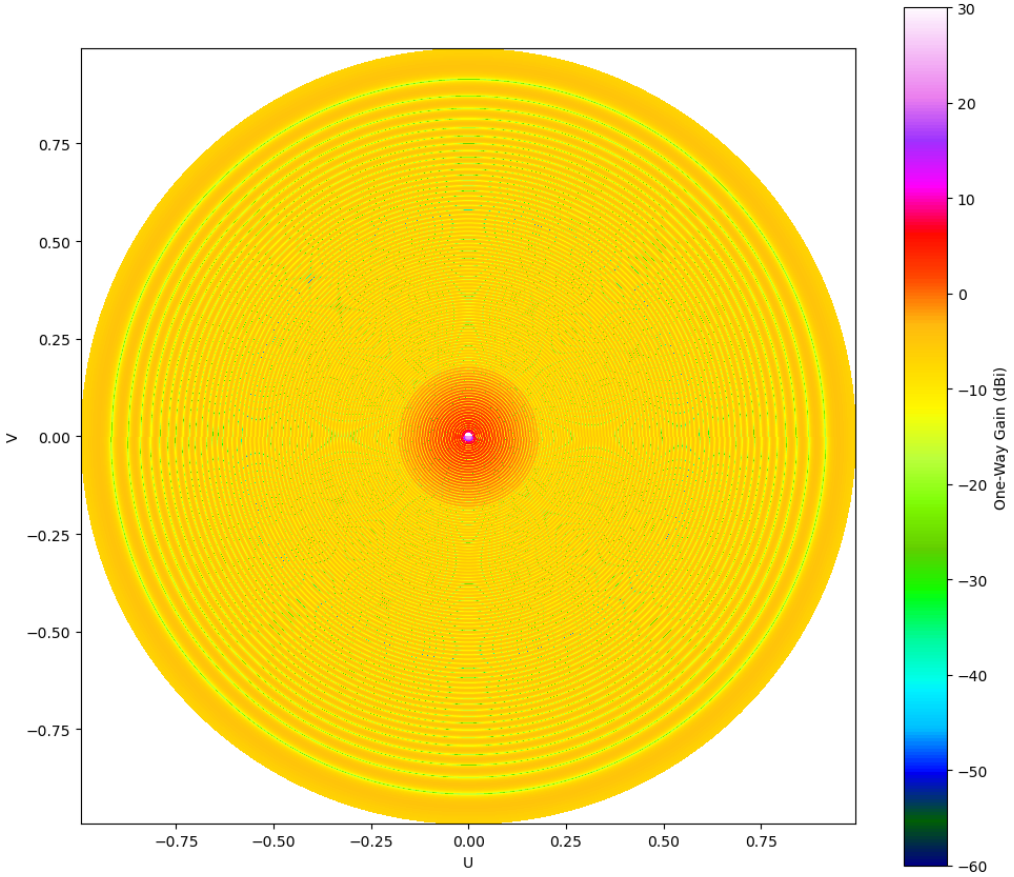


Figure 3.2: Emulated WSR-88D transmit beam pattern.

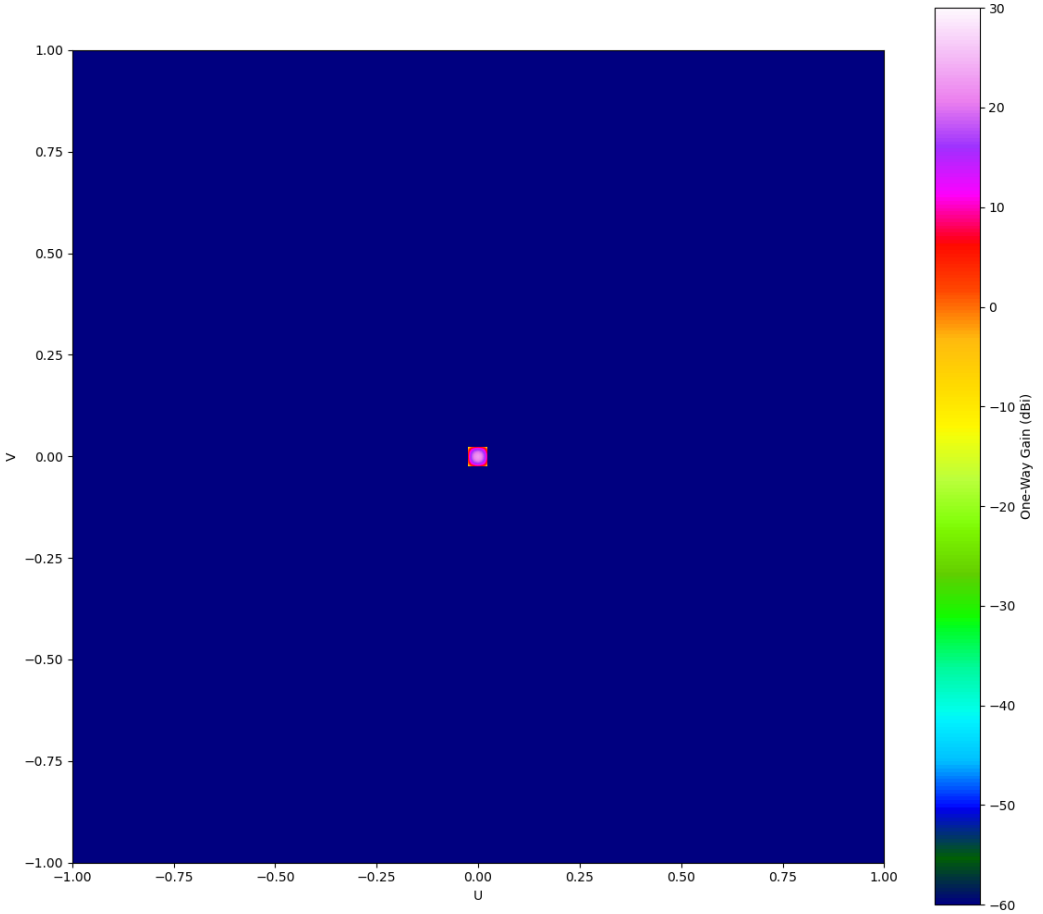


Figure 3.3: Ideal transmit beam pattern.

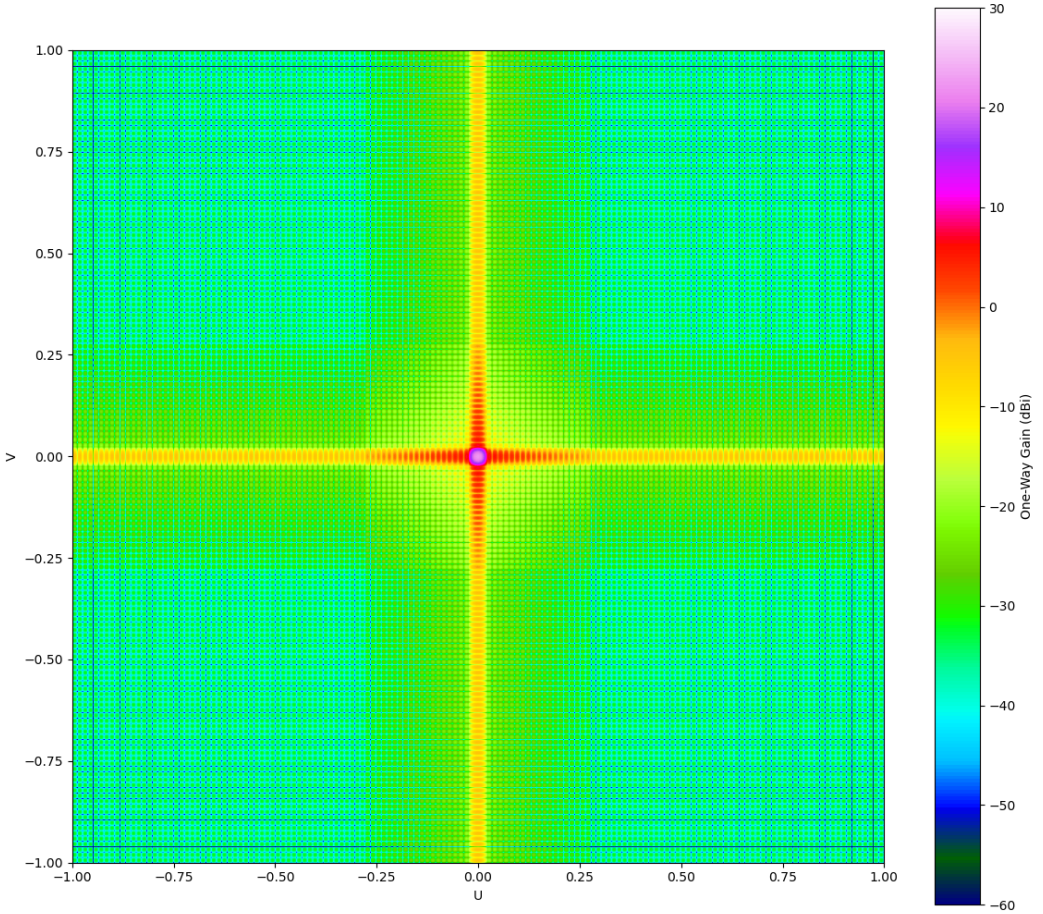


Figure 3.4: WSR-88D-equivalent PAWR transmit beam pattern.

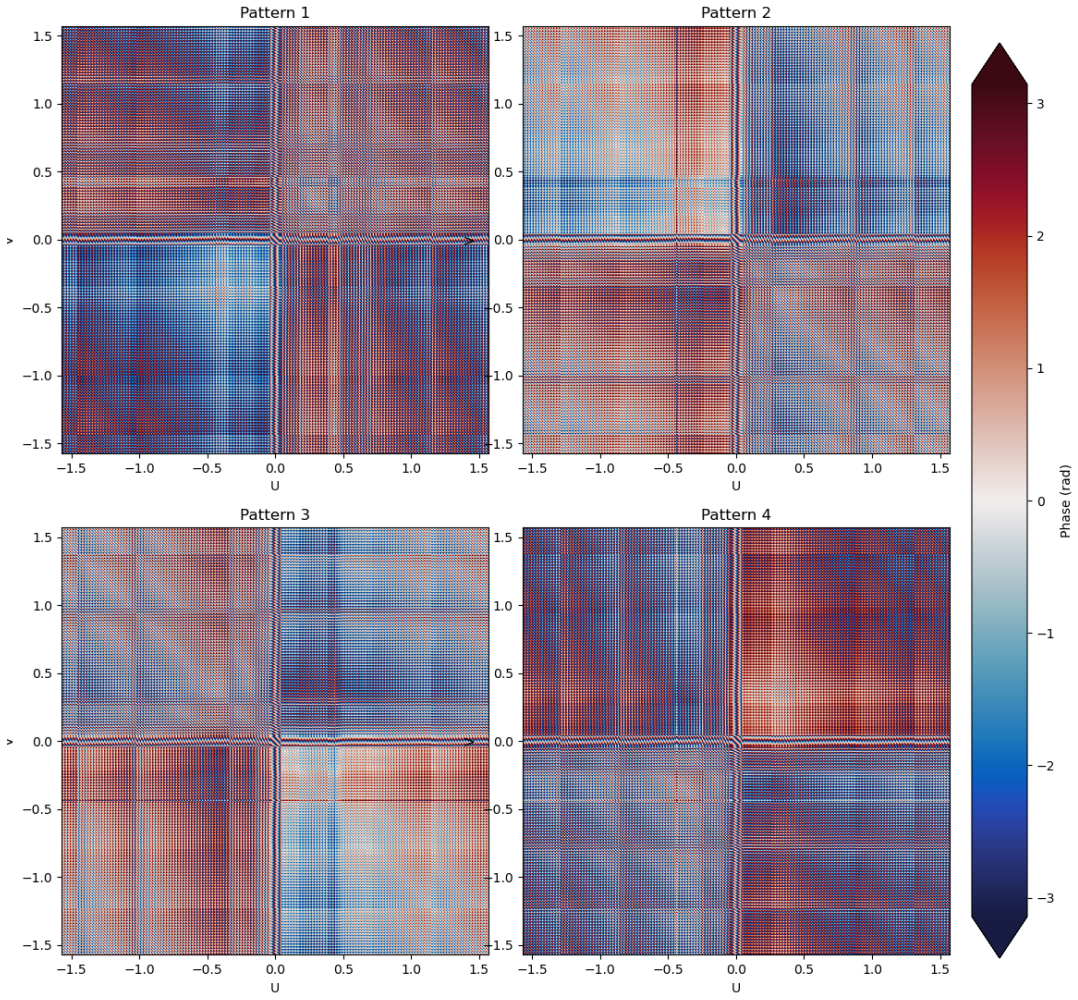


Figure 3.5: Transmit phase patterns for simulated sidelobe whitening.

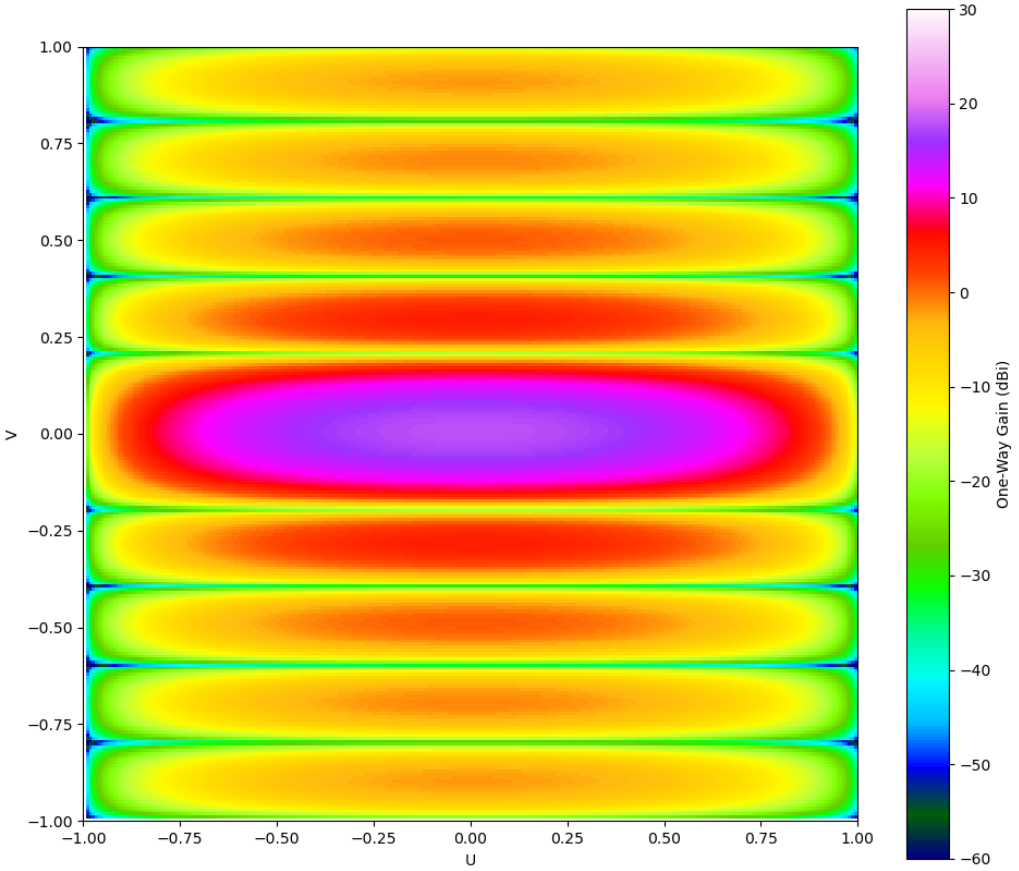


Figure 3.6: Receiving antenna beam pattern.

### 3.1.1 Experiments

As shown previously, the resolution volumes in a bistatic system vary in size with bistatic angle, meaning that care must be taken when analyzing these data onto a common Cartesian grid. The method employed here is similar to the beamwidth-based method used by the ARM Python Radar Toolkit (Py-ART) (Helmus and Collis, 2016), where the radius of influence is scaled based on the radial distance from the transmitting radar. However, an additional factor from the bistatic angle is used (Equation 3.1), which greatly increases the radius of influence for volumes with large bistatic angles (i.e. close to the baseline). The gates are weighted using a 2-pass Barnes weighting with a nominal bandwidth ($\kappa = 0.17km$).

Both the range-corrected power and bistatic velocity are gridded onto an isotropic Cartesian grid ($\delta x = 0.3km$) for further quality control and analysis. The gridded range-corrected power fields for all receivers are compared to reduce the effect of sidelobe echoes as much as possible. If two or fewer receivers have detectable power for a given grid cell, then the data for that cell are rejected from further analysis. Following the methods of de Elía and Zawadzki (2001), a location index for each receiver across the entire grid domain is computed (Equation 3.5). This index uses factors involving the estimated sensitivity of the receiver (Equation 3.2), the expansion factor of the bistatic resolution volumes (Equation 3.3), and the standard deviation of the beam-orthogonal wind (Equation 3.4) to yield an estimate of the quality of the measured bistatic velocity. The receivers are then ranked on a cell-by-cell basis to determine the best n receivers to include in the dual-Doppler analysis, where n can be a positive integer between two and the network's receiver count. For the purposes of this study, $n$ was either set to 3, which guarantees at least three receivers per grid point for smaller networks but limits the

number for larger networks, or to $N$, the total number of receivers, which utilizes all available data, regardless of the quality of said data. The reasoning for limiting the number of included receivers with larger networks is that receivers with comparatively worse location indices may have lower quality velocity data, which could be detrimental to an over-determined multi-Doppler synthesis.

Once the preferred sets of velocity data are selected, a simple least-squares multi-Doppler retrieval (Equation 2.3) is done on a cell-by-cell basis. Though the full three-dimensional wind field is retrievable with this process, the shallow scanning angle used in these simulations resolves little of the $w$ component of the particle velocity vector, so the direct retrieval results for $w$ are excluded. Further, $w$ could be better obtained through integration of vertical divergence given that the $u$ and $v$ fields are likely to be highly constrained, but the evaluation of $w$ from these additional steps falls out of the scope of this work, as these additional steps would likely introduce other systematic errors unrelated to the accuracy of the bistatic velocity data. Thus, we wish to focus on the accuracy of the directly retrieved velocities. To validate the retrieved $u$ and $v$ fields, the input model fields are linearly interpolated onto the coarser retrieval grid. The mean absolute error and root-mean squared error are then computed using the regridded model data as a truth field. Further intercomparison between the error characteristics of the retrievals is done via histograms of the errors.

$$ROI = \max\left(r_{min}, h\frac{z}{20} + \sqrt{x^2+y^2}\frac{\tan\theta_b}{2\cos\beta/2}\right) \tag{3.1}$$

$$\bar{P_r} = \frac{P_t G_t \lambda^2 \cos^2\gamma}{(4\pi)^3 r_{rx}^2 \cos^2\beta/2} Z \tag{3.2}$$

$$R_{vol} = \frac{1}{2}\cos^2 \beta/2 \tag{3.3}$$

$$\sigma_{v_t} = \sqrt{\left(\frac{1}{\tan \beta/2} + \tan \beta/2\right)^2 + \frac{1}{\tan \beta/2}} \tag{3.4}$$

$$I_l = aP_r + bR_{vol} - d\sigma_{v_t} \tag{3.5}$$

## 3.2 Observations

The prototype network used for these observations is identical in layout to that of Byrd et al. (2020), consisting of two bistatic receivers around the Oklahoma City, OK metropolitan area: one located on the University of Oklahoma campus at the Radar Innovations Lab, and another atop the OU Health Sciences Center. This results in two $\sim$20 km baselines emanating from the KTLX WSR-88D roughly perpendicular to one another, forming an excellent dual-Doppler region over the southern Oklahoma City metropolitan area. The design of the receiver unit is nearly identical to that of Byrd et al. (2020), with the exception of the digital transceiver, which has been replaced with an inexpensive, commercially available part (bladeRF micro 2.0). Operation of the prototype receiver is quite simple, consisting of a single manually-controlled continuous receive mode. The I/Q data are then stored on a local hard disk for post hoc DSP and analysis. The DSP is also quite similar to that of Byrd et al. (2020), but with a few tweaks to the PRF estimation algorithm and dual-Doppler analysis methods. The DSP process in short is as follows: the I/Q stream is filtered with a CFAR algorithm, then individual pulses are identified via a matched filter for a WSR-88D 1.57 $\mu s$ short pulse. The pulses are then

cross-correlated with the WSR-88D pointing angle data to roughly align the pulses with associated radials. Following this, the PRF and PRF mode are then estimated through a Fourier-based heuristic, allowing for a more precise time alignment for each pulse train. These pulse trains are then used to recreate an effective correlated I/Q signal from the raw I/Q data. A phase correction based on both the relative motion of the WSR-88D antenna's phase center and any detected SZ-2 phase coding is then applied. Next, pulse-pair processing is done on the resultant I/Q data to form the bistatic moments in the form of range-corrected power and bistatic Doppler shift. Finally, the pointing angle data are again used to localize the volumes in space and to convert the bistatic Doppler shifts into the bistatic Doppler velocity.

Once the moments are localized, the data from all available receivers are then gridded onto a common Cartesian grid with a horizontal grid spacing of 500 $\mathrm{m}$ and a vertical grid spacing of 250 $\mathrm{m}$. These grid spacings were chosen to best match the reduced spatial resolution of the bistatic receivers while still attempting to retain finer resolution, especially in the vertical dimension so as to better suit vertical integrations. The overall grid size used in the analyses were square or rectangular regions measuring 30–40 $\mathrm{km}$ in the horizontal and 12 $\mathrm{km}$ in the vertical, depending on the scale of the phenomenon of interest and the spatial extent of usuable bistatic data. Quality control is done on the bistatic moment data by filtering the observed bins based on SNR (10 dB) before gridding, then performing mutual exclusion based on received power between the grids for each receiver. This SNR threshold is above what is typically needed for proper Doppler velocity estimation, but does serve to reduce the amount of clear-air sidelobe returns ingested into the retrieval. A dual-Doppler analysis is then performed with the available bistatic data and the corresponding monostatic data from KTLX using the Pythonic Direct Data Assimilation (PyDDA) library Jackson et al. (2020), yielding a 2D or 3D wind retrieval,

depending on the number of bistatic receivers available. Validation of the multistatic wind retrievals is done by comparison to a contemporaneous multi-Doppler retrieval using several available monostatic radars. These validation retrievals follow the same procedure as the multistatic retrievals, and are mapped onto the same Cartesian grid. A direct numerical comparison between the two retrievals would be appropriate to characterize the exact nature of the error characteristics of the multistatic retrievals, but there is still enough uncertainty in both retrievals that doing so may underscore the relative quality of the multistatic retrievals, especially when factoring in the fundamental differences in observation times between the two and the relative cost of the multistatic method versus a multi-monostatic retrieval. Thus, the multistatic retrievals will be evaluated against the monostatic retrievals in a more qualitative sense, comparing both the directly-retrieved wind fields and computed fields like vertical vorticity. This will hopefully demonstrate the effectiveness of multistatic retrievals in a meteorological sense.

# Chapter 4

# Results

## 4.1 Simulations

### 4.1.1 Sensitivity Experiments

As described previously, a series of sensitivity experiments were conducted to test the marginal benefits of adding more receivers to a multistatic network. The experiments consist of several trials of simulations with an increasing number of receivers positioned equidistant from the transmitting radar in a circular fashion. The input weather fields ($u$, $v$, $w$, and $Z$) for the experiment were uniform and positive across the entire domain, and the transmitting radar used the ideal pencil-beam pattern (Figure 3.3), meaning that the only factor affecting the wind retrievals should be the number of receivers in the network.The results of the sensitivity experiments are summarized in Figures 4.1 to 4.4.

As receiver count increases —*ceteris paribus*— the quality of the multistatic retrievals in terms of root mean squared error improves up to $N = 6$ receivers, after which the quality remains essentially constant. It should be noted that the quality statistics are only computed on grid cells with retrieved values, meaning that such statistics could be skewed if the retrieved area is much smaller than the

input area. To quantify this, the coverage of the retrieval area relative to the input area is computed, shown in Figure 4.4. As one would expect, a network with few receivers will be constrained to retrieving only certain areas of the overall domain of interest, since all of the previously described metrics must be met by multiple receivers at each given point. As the number of receivers increases, the coverage also rapidly increases, reaching $\approx 95\%$ coverage at 6 receivers, and $100\%$ at 8 receivers. Both metrics show a rapid improvement between 3 and 6 receivers and little improvement beyond, suggesting that a bistatic network would need no more than 6 receivers for most use cases. If a larger domain is used, say 60 km x 60 km, the results remain largely the same, though the coverage becomes bound not by the number of receivers, but by the effective range and sensitivity of the receiving antenna. However, the overall error does marginally increase for all configurations, likely due to regions of inflated errors close to receiver sites. With these factors in mind, it is quite plausible that the use of antennae with higher gain and smaller receive apertures to extend the maximum effective range would necessitate a greater number of receivers, since such antennae would cover narrower regions than the horizontally-isotropic receive patterns used in these simulations. However, even a doubling of the number of needed receivers would still result in a decrease of the concentration of receivers per unit area of the analysis domain. This would likely hold true for a system covering a WSR-88D surveillance domain, since the requirement of sidelobe interception would limit the baselines to perhaps 60 km. A hypothetical system under this scenario would likely consist of two rings at 30 and 60 km range, with 6 and 9 receivers, respectively, which would cover an area roughly 90 km x 90 km.

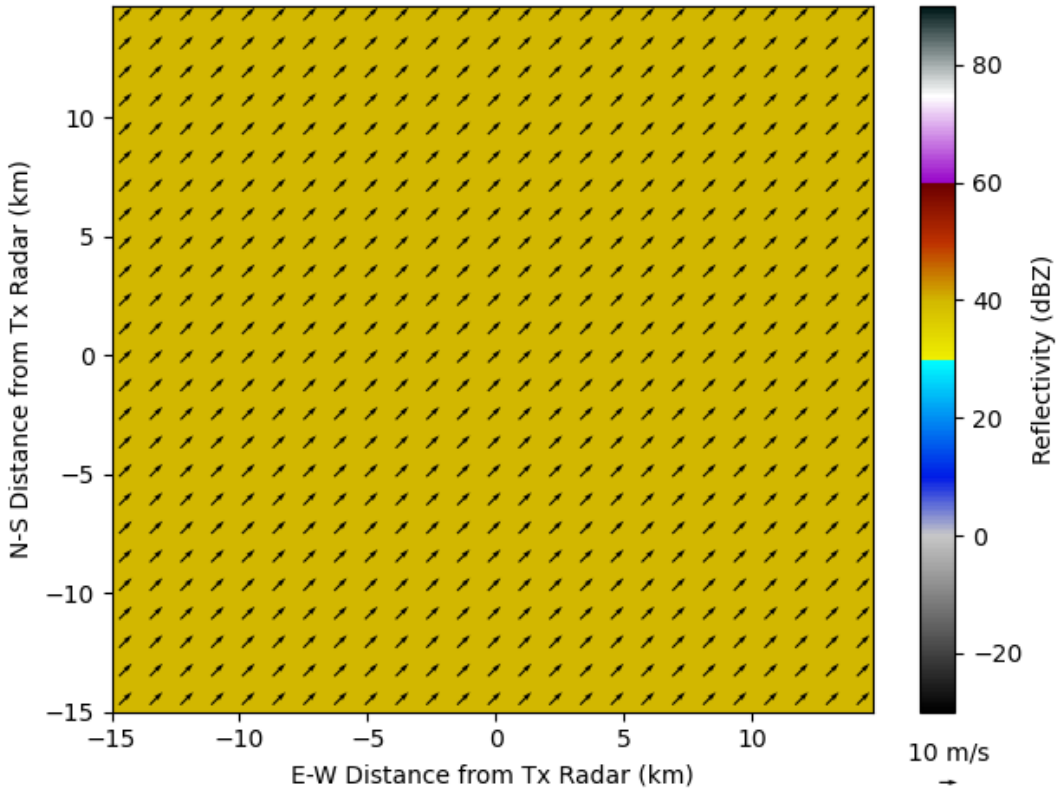


Figure 4.1: Schematic of the model input for the sensitivity test. All fields ($u$, $v$, $w$, Z) are uniform across the simulation domain.

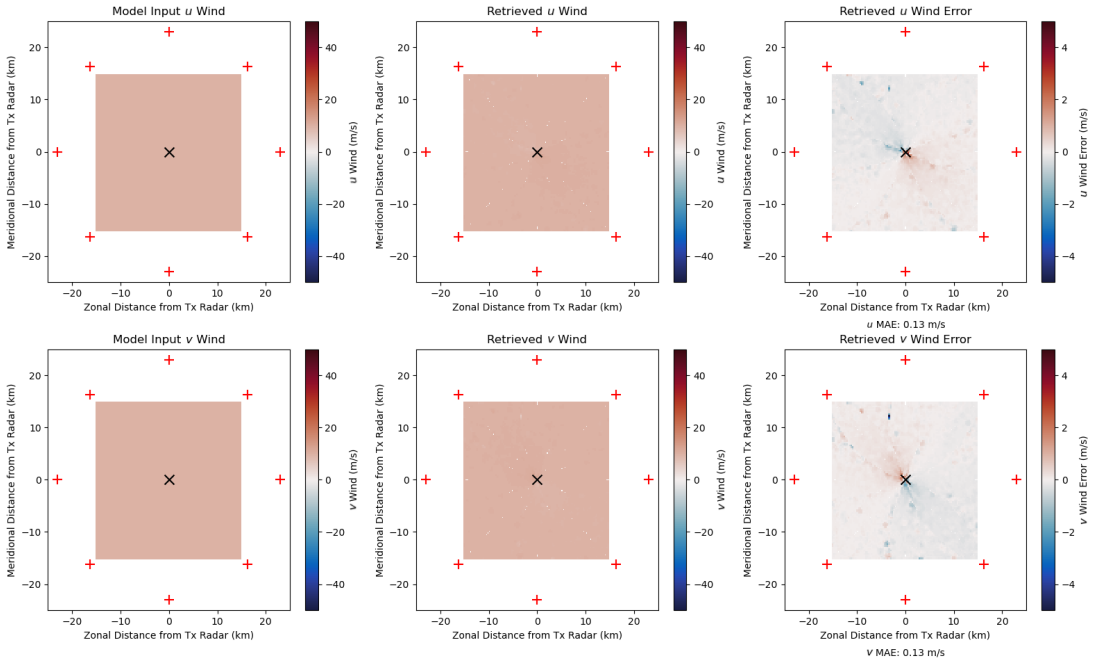


Figure 4.2: Sample results from $n = 8$ trial, demonstrating low error and a nearly spatially isotropic error distribution.

### 4.1.2 Beam Pattern Experiments

Since the previous experiments avoided the effects of sidelobe contamination by using a uniform reflectivity and wind field, we must introduce sidelobe contamination in a simple and understandable fashion. To accomplish this, the input fields to the simulation were altered to resemble Figure 4.5, consisting of a 40 dBZ background field with weak $u$ and $v$ flow regularly interspersed with square columns of 60 dBZ and much stronger $u$ and $v$ flow. Though this field has an infinitely sharp reflectivity gradient at the boundaries of each column, the grid spacing of the input data and spatial sampling of the simulated transmitting radar yields an effective reflectivity gradient of 50-60 dB/km, which Mueller (1977) notes is not uncommon in convective cells.

Figures 4.6 to 4.8 show that increasing receiver count while keeping the number

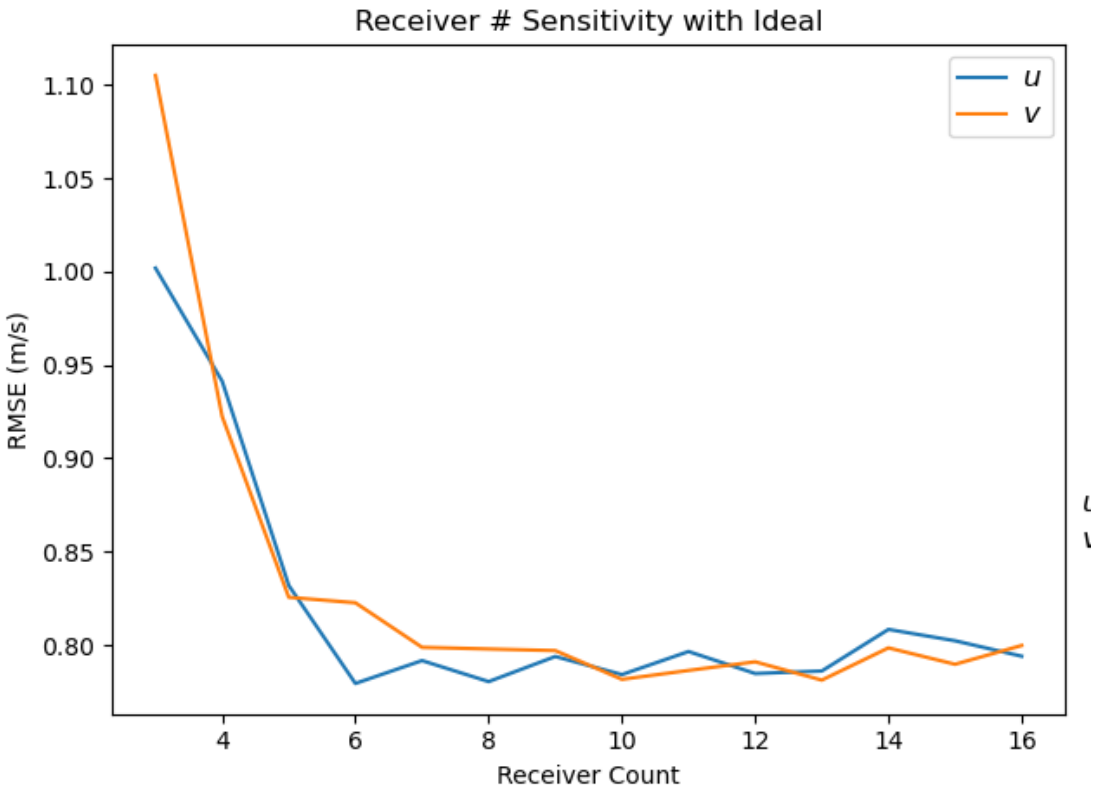


Figure 4.3: Line plot of the root mean squared error of the retrieved $u$ and $v$ components with increasing receiver count using an ideal beam pattern.

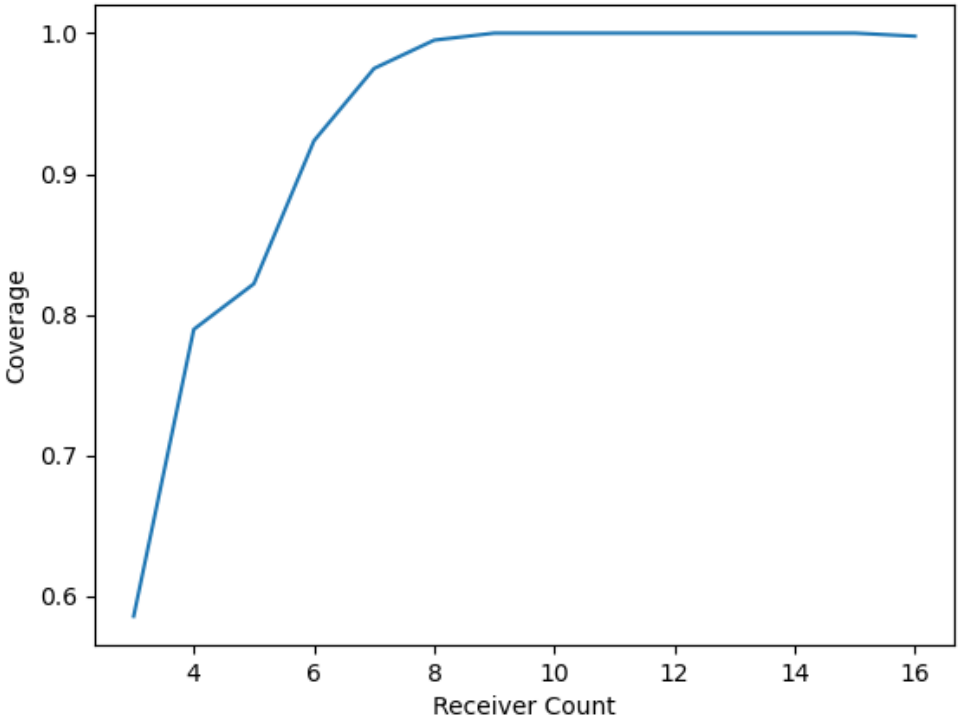


Figure 4.4: Line plot of the coverage of the effective retrieval area and receiver count.

of receivers under consideration constant seems to be the best method of reducing error compared to sidelobe whitening, though whitening does have a beneficial effect. This is most evident at low receiver counts, where most of the data are used in the retrieval, allowing the improvements in the moment data to appear. However, this degree of improvement does not continue at high receiver counts, as the retrieval appears to become degraded regardless of the beam pattern used. When the retrieval is forced to use data from all available receivers (i.e., highly over-determined), the improvement from more receivers is hardly noticeable after 5–6 receivers, and even decreases in quality after 8 receivers. This is likely due to the forced inclusion of data with significant sidelobe contamination. However, the system with sidelobe whitening is able to consistently outperform the unwhitened system by a small margin, and both are far superior to the conventional dish system. Interestingly, the retrievals which use only the data from the best-positioned receivers markedly outperform the retrievals which use all available data for the over-determined systems, suggesting that having the ability to select receiver data for inclusion could be as important as sidelobe whitening for improving retrieval quality. With that being said, it is evident that sidelobe whitening is still effective at decreasing the degree of sidelobe contamination in the moment data. The superiority of the PAWR performance compared to the dish system is expected due to lower sidelobe levels, but this does highlight the potential improvement when using a PAWR as a transmitter given their ability to use adaptable beam patterns.

### 4.1.3 Applications to Current Network

To test the utility of the previous hypotheses on a more realistic network, a similar series of experiments was carried out upon a 2-receiver network with nearly

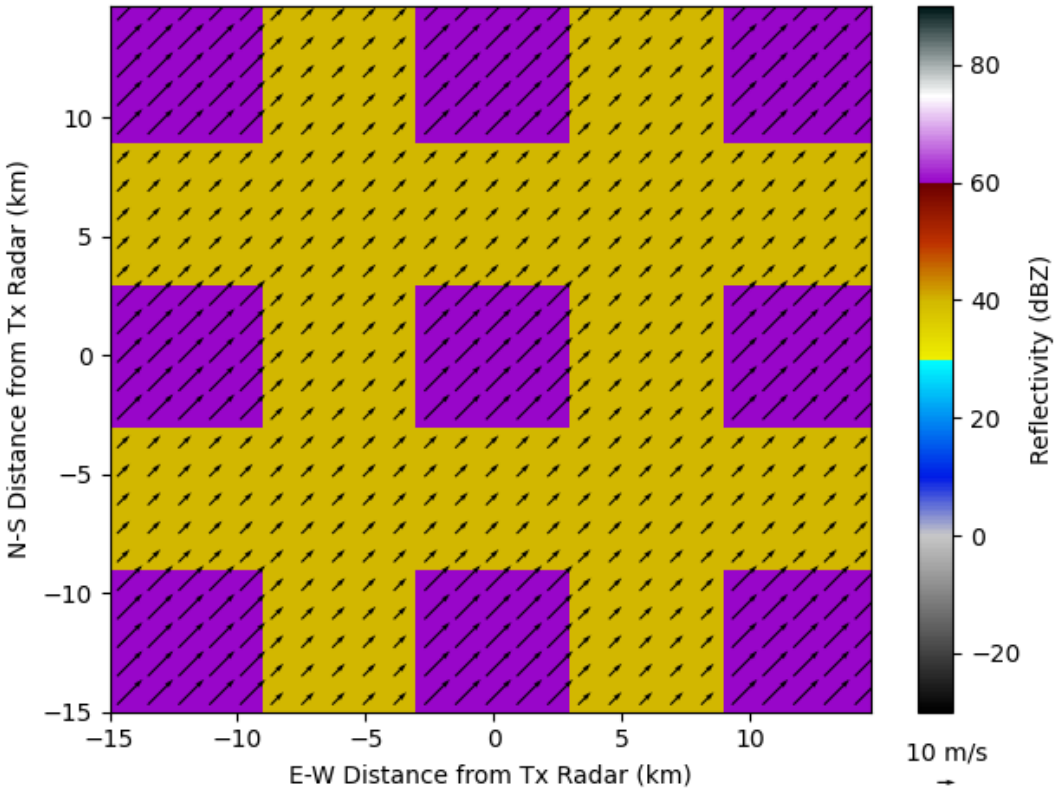


Figure 4.5: Schematic of the model input for the beam pattern sensitivity test. The fields are non-uniform in the horizontal, but are constant in the vertical.

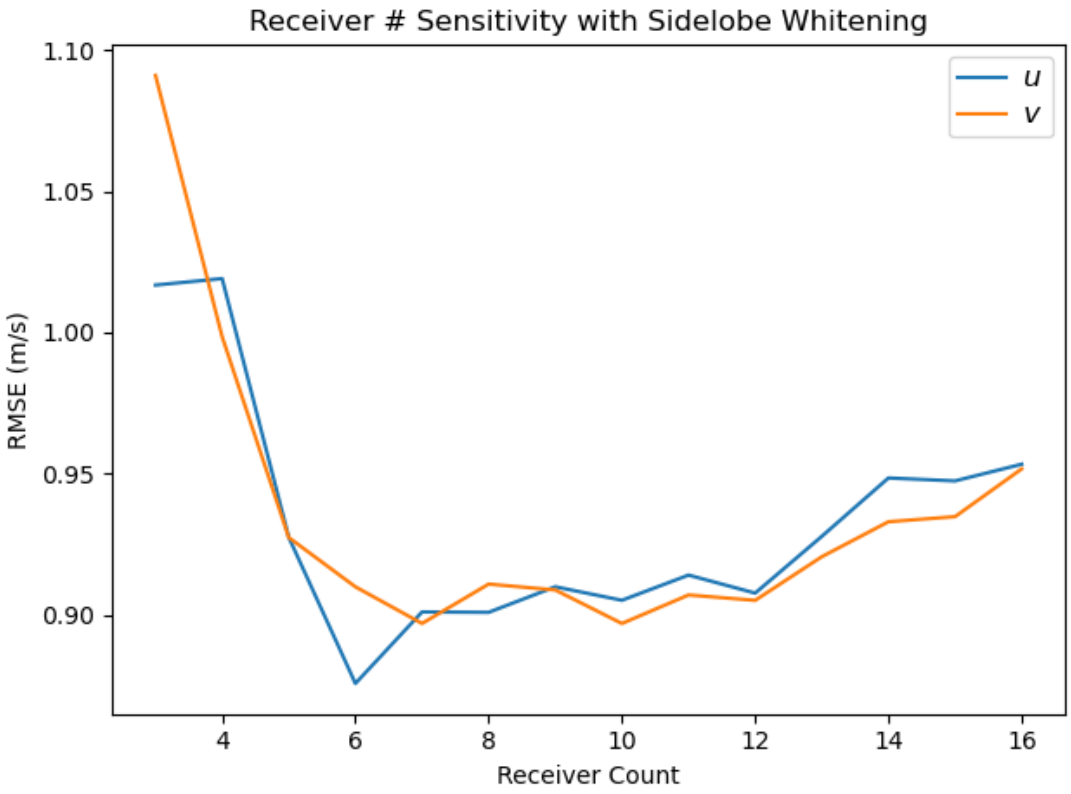


Figure 4.6: Similar to Figure 4.3, but utilizing a phased-array beam pattern with whitened sidelobes.

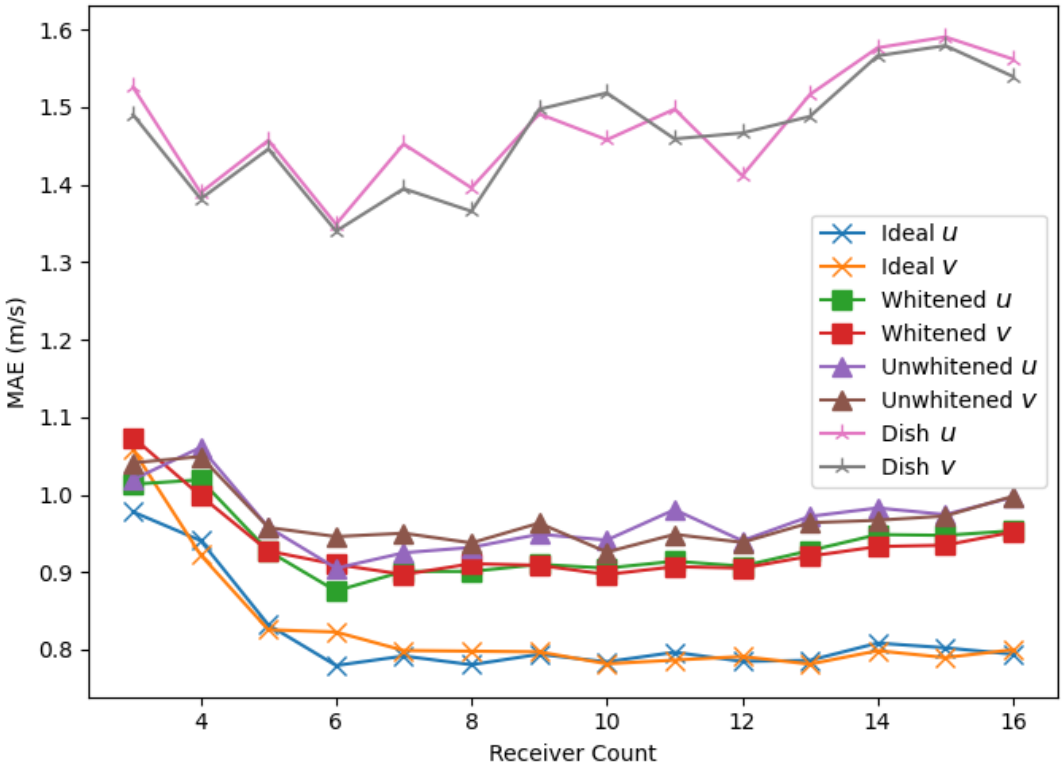


Figure 4.7: Plot of mean absolute error of retrieved $u$ and $v$ as a function of total receiver count, using the 3 best receivers at each retrieval point.

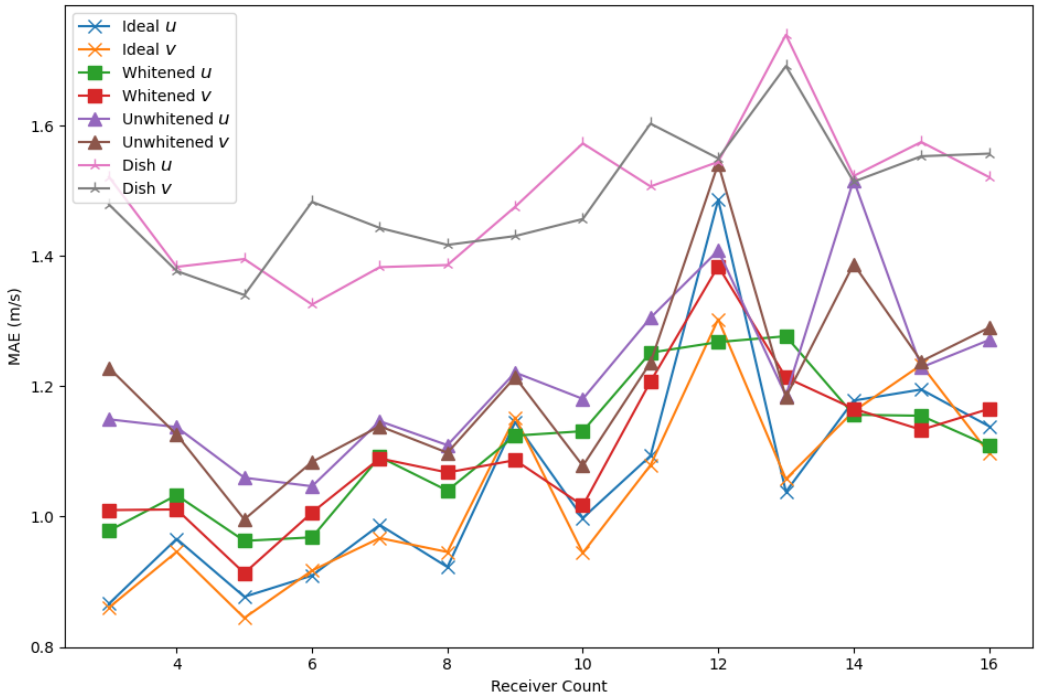


Figure 4.8: Similar to Figure 4.7, but using all receivers at each retrieval point.

identical characteristics as the current prototype network ($\sim$20 km baselines in a NW-SW orientation). Instead of a relatively uniform precipitation and wind field, the input fields for observation are a simulated supercell with an intense ongoing tornado-like vortex (TLV). As before, the transmit beam pattern is varied between an emulated parabolic dish, a phased array with and without sidelobe whitening, and an ideal pencil beam. Additional receivers are equally spaced along the two baselines to create an expanded 6-receiver network.

The retrieval results for the baseline 3-receiver network are shown in Figures 4.9 to 4.12. The 3-receiver network utilizing the ideal beam pattern fares quite well, with the only significant errors occurring in close proximity to the TLV, where the geometric dilution of precision limits the effective resolution of the analyzed wind field. The 3-receiver network with the emulated dish pattern (closest to the real-world network) fares the worst in terms of retrieval performance, which is expected given the prominent sidelobes in the pattern. The areas with the highest degrees of sidelobe contamination are in the forward flank region of the supercell, which is common for WSR-88Ds (Nai et al., 2020; Boettcher and Bentley, 2022). The sidelobe contamination is so severe that even some clear-air areas are not properly rejected, leading to regions of spurious retrievals. As is typical in supercells, the sidelobe contamination in this case is a combination of azimuthal and elevation effects, where the precipitation overhang of the supercell is strong enough to manifest across all receivers, regardless of viewing angle. The SNR threshold of 10 dB does help to some degree, but the high sidelobe levels of the dish pattern coupled with the strong reflectivity gradient are sufficient to generate a remarkably strong sidelobe echo. Increasing the SNR threshold would certainly cut down on this artifact, but regions of true weather echo would also be pared away. However, the deleterious effects of sidelobe contamination also extend from the forward flank region into the

mesocyclone, manifesting as retrieval errors as high as $10\ \mathrm{m\,s^{-1}}$ within this region. The TLV is still resolved, albeit with a weaker circulation and is surrounded by spurious horizontal winds. If only 3 receivers are available, data from all receivers must be used regardless of quality (outside of obvious clear-air sidelobe contamination), so the benefits of sidelobe whitening are particularly evident in this case. Further, the area of multi-Doppler coverage is somewhat limited, highlighting the importance of data quality within the region of interest.

As expected, both the unwhitened (Figure 4.11) and whitened (Figure 4.12) beam patterns yield better error characteristics than the dish pattern due to the lower intrinsic sidelobe levels of those patterns. The improvement appears to stem from less inclusion of clear-air sidelobe contamination, as well as less contamination within the true weather echoes. As with the other patterns, the largest errors are concentrated around the TLV, which is reasonably well-resolved compared to the ideal beam pattern. Most importantly, the retrieval using sidelobe whitening does again outperform the unwhitened system by a small margin. The difference in errors between the two retrievals is not immediately apparent, aside from a shift in the small region of clear-air sidelobe contamination. Further inspection shows a slight improvement with the whitened system within the forward flank region on the order of $0.5\ \mathrm{m\,s^{-1}}$, which would make sense given the propensity for severe sidelobe contamination in weather echoes within this region and the expected effects of sidelobe whitening. However, the TLV is virtually identical in terms of error between the two, suggesting that the errors in this region are either due to the intrinsic geometric dilution of precision of the multistatic receivers, or extremely tight and coupled gradients in reflectivity and velocity that are too sharp for even the narrow transmitting beam to resolve. Either way, it would appear that sidelobe whitening is not a panacea for instantly improving multistatic retrievals.

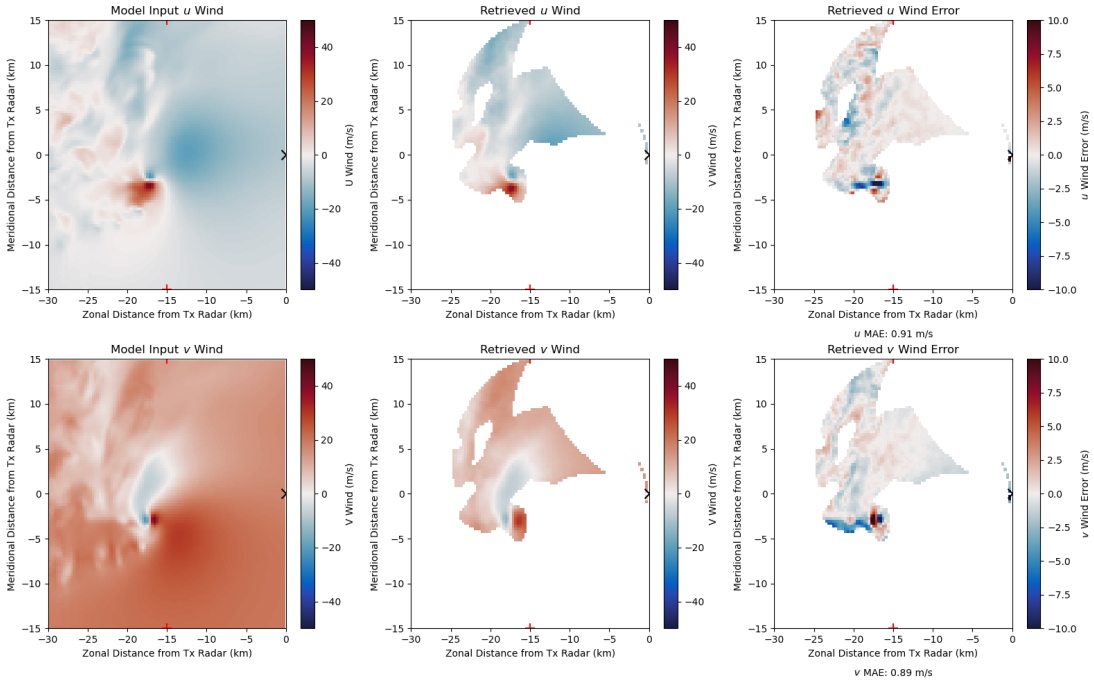


Figure 4.9: Retrieval results ($u$ top, $v$ bottom) for a 3-receiver network using an ideal beam pattern. Left column is the input wind fields, center is the retrieved wind fields, and right is the difference between the two. Retrieval points with low SNR and/or poor geometry are excluded.

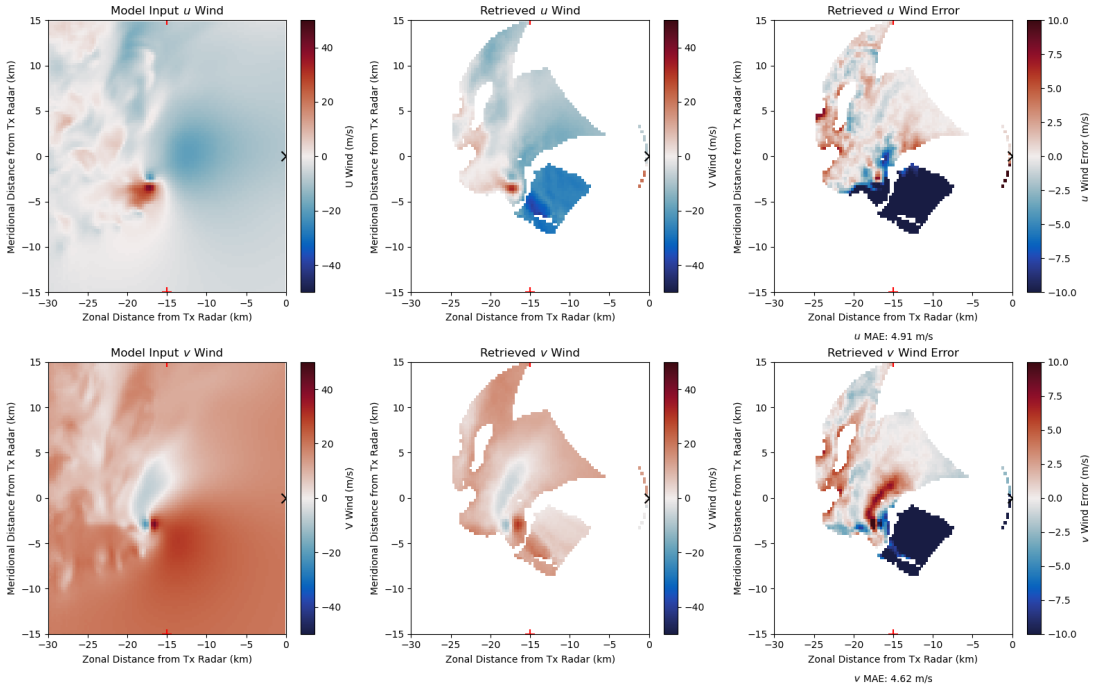


Figure 4.10: Similar to Figure 4.9, but using an emulated dish beam pattern.

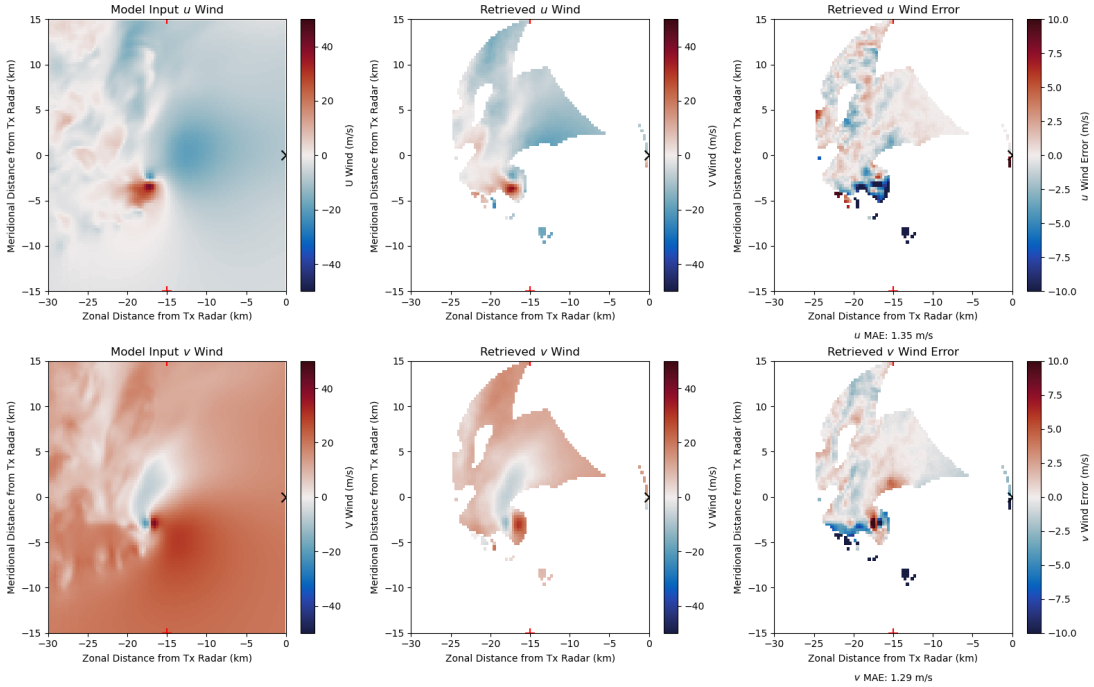


Figure 4.11: Similar to Figure 4.9, but using an emulated phased array pattern without sidelobe whitening.

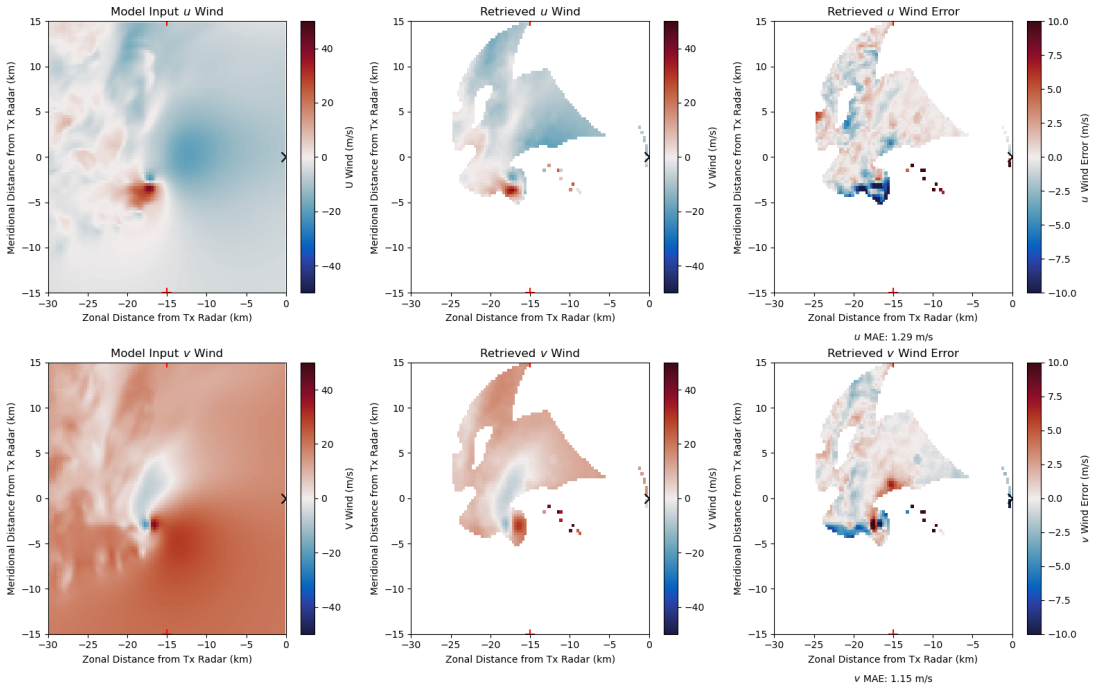


Figure 4.12: Similar to Figure 4.9, but using an emulated phased array pattern with sidelobe whitening.

In contrast to the previous minimal 3-receiver network, the 6-receiver network shown in Figures 4.13 to 4.15 has much better coverage, resolving essentially all of the supercell. The network using the ideal beam pattern yields even better retrieval results than the 3-receiver network, with mean absolute errors around $0.8\ \mathrm{m\,s^{-1}}$ across the domain. Much like the smaller network, the largest errors are again near the TLV, likely due to the degraded spatial resolution. Using the emulated dish pattern still yields a large region of poor retrieval quality due to sidelobe contamination, though the domain-mean errors are somewhat better than the 3-receiver network. In particular, the TLV does appear to be much better resolved by this network, manifesting as a clear couplet in both $u$ and $v$. When the analysis is done using the location index filtering technique, the results improve drastically in terms of the domain-mean error, though the improvement comes chiefly from the removal

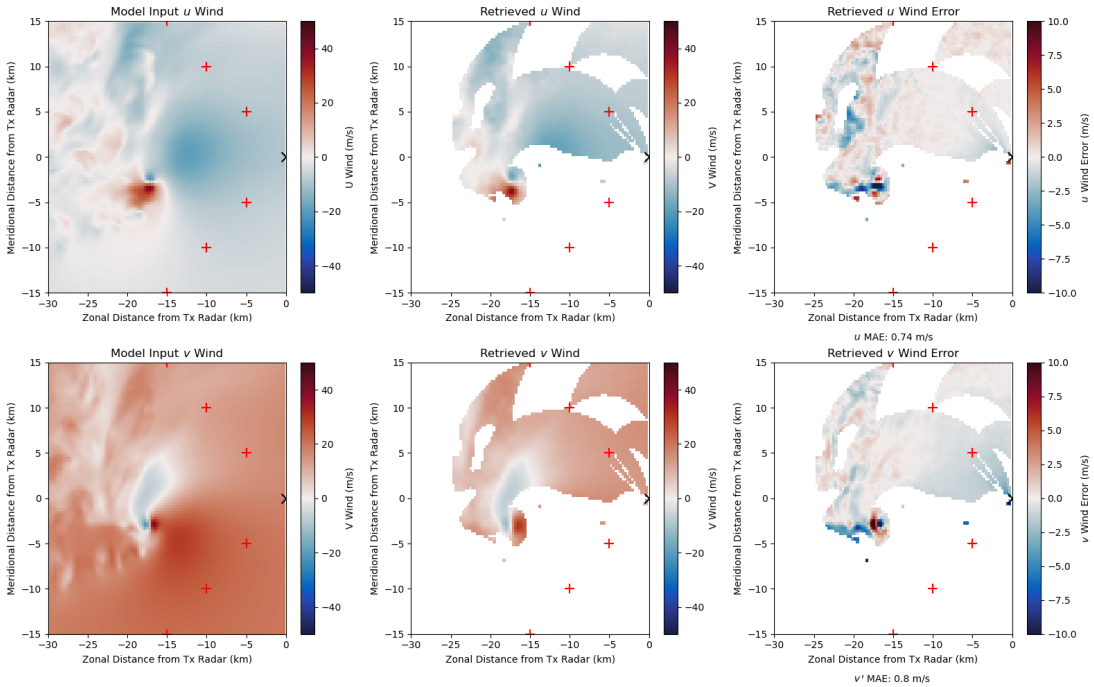


Figure 4.13: Similar to Figure 4.9, but with a network of 6 bistatic receivers.

of clear-air echoes. This improvement can be better quantified via Figures 4.16 and 4.17, which show the general distribution of the absolute error of the two analysis techniques and the difference of the two distributions, respectively. Overall, the change in analysis technique yields an average improvement of $0.5\ \mathrm{m\,s^{-1}}$ when using the location-based filter vs. no filtering. This is in line with the results of 4.1.2, suggesting that amelioration of sidelobe contamination can be achieved by increasing receiver count and applying an appropriate filter.

Comparing the results for the PAWR pattern with (Figures 4.20 and 4.21) and without sidelobe whitening (Figures 4.18 and 4.19) shows a small, but marked improvement in domain-mean results with whitening enabled. Unlike the gains in the dish vs. ideal comparison, this change appears to be purely from the true reduction of sidelobe return in regions of weather echoes, rather than the elimination of spurious clear-air sidelobe echoes. This is not particularly surprising, but the improve-

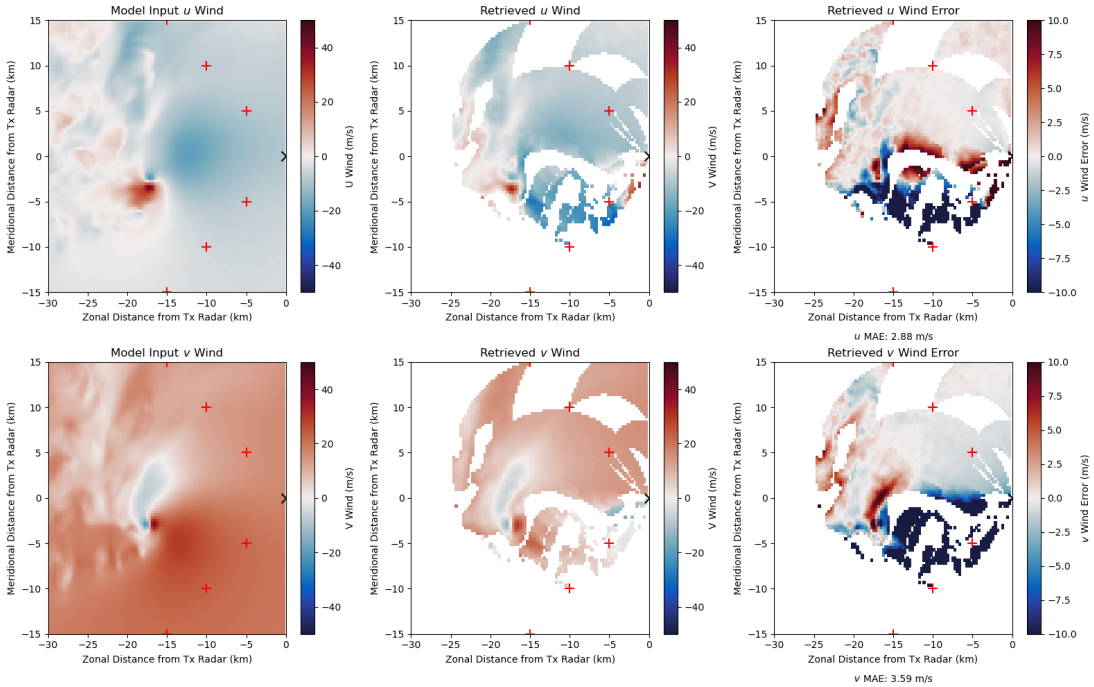


Figure 4.14: Similar to Figure 4.13, but using an emulated dish beam pattern.

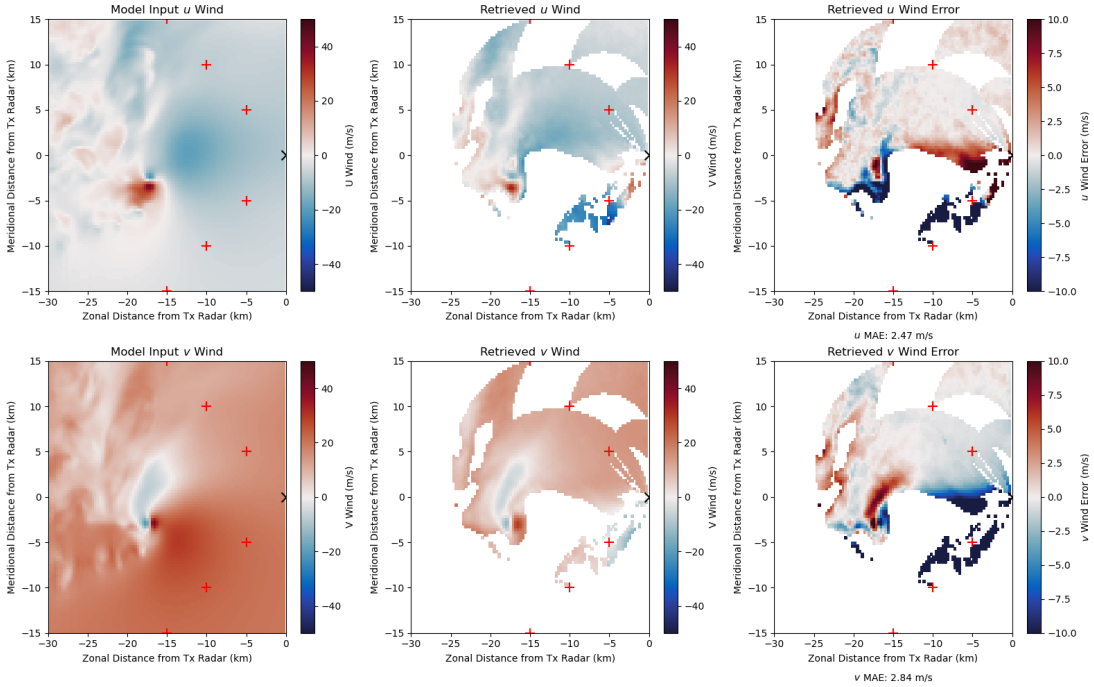


Figure 4.15: Similar to Figure 4.14, but retrieved using data from the 3 best receivers per grid point per Equation 3.5.

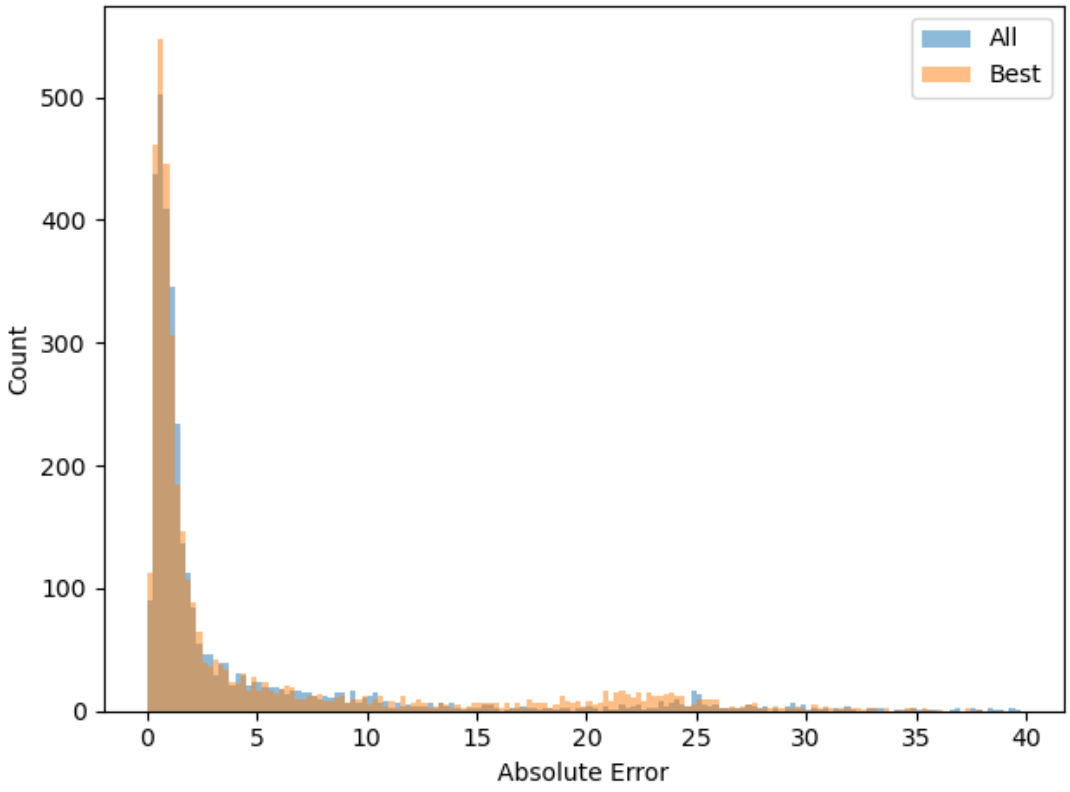


Figure 4.16: Histograms of point-by-point absolute errors associated with the retrievals using all available bistatic data (blue, Figure 4.14) and data from the 3 best receivers (red, Figure 4.15).

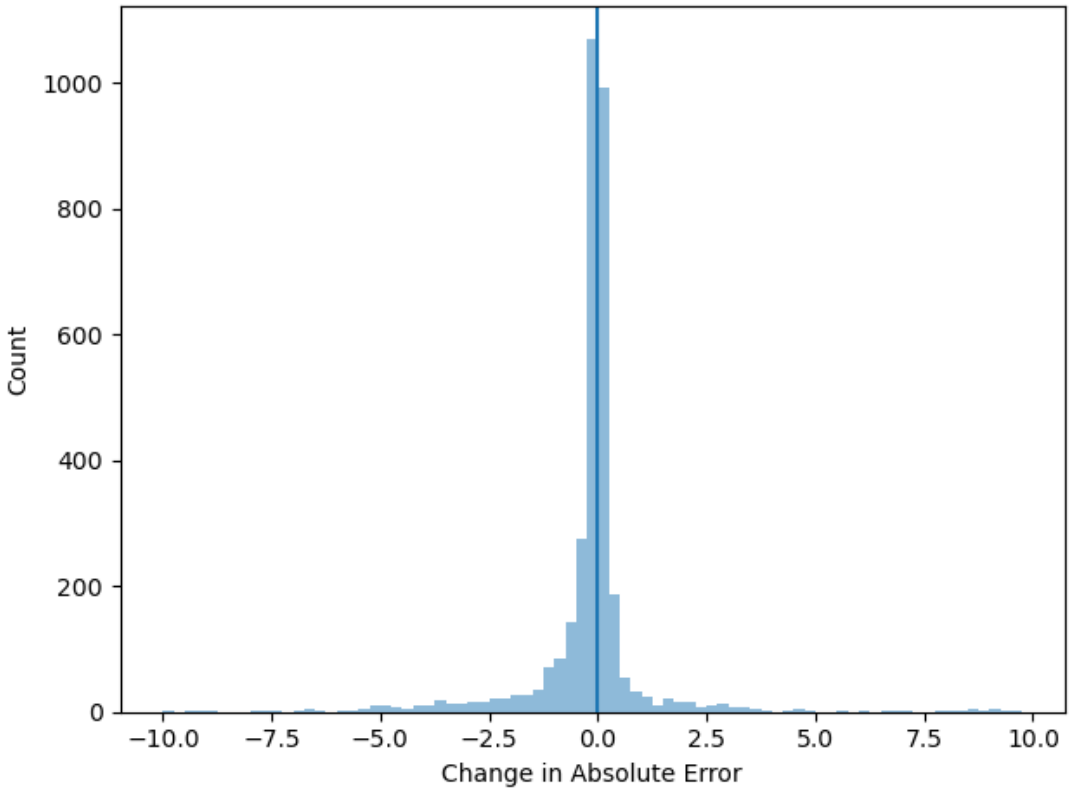


Figure 4.17: Histogram of the point-by-point difference in error between the selective method and utilizing all data.

ment achieved by whitening is notably larger in magnitude ($0.25\ \mathrm{m\,s^{-1}}$) compared to the approximate average change ($0.1\ \mathrm{m\,s^{-1}}$) from the beam pattern sensitivity experiments in Section 4.1.2, plausibly due to more gradual gradients in $u$, $v$, and Z in the simulation data. When comparing the results from using the location-based filter Figures 4.22 and 4.23, the improvement in the unwhitened network ($0.2\ \mathrm{m\,s^{-1}}$) is less than what is achieved by the same method in the dish-based network. Further, the difference between whitening with and without filtering Figures 4.24 and 4.25 is negligible, suggesting that the improvements gained by selecting the best receivers based on bistatic geometry is indeed tied to reduction of sidelobe contamination. Thus, the findings of Sections 4.1.1 and 4.1.2 become relevant, as it is possible that being more selective in determining which data to include in the multi-Doppler retrieval could be as important as the transmit pattern when comparing the accuracy of the 3D wind retrievals. Considering the sizable hardware and software requirements for implementing sidelobe whitening with a PAWR (element-level control, phase pattern synthesis, etc.) and the marginal benefits gained in the end product, it would appear that sidelobe whitening should not necessarily be leaned upon for the reduction of sidelobe contamination within multistatic networks, at least if the per-receiver unit cost is reasonably low.

### 4.1.4 Caveats

As noted before, the results gained from these simulations are subject to some caveats. First, the simulated receiver pattern is nearly isotropic in azimuth, which greatly simplifies the exact positioning of the receivers, but is not exactly realistic compared to the actual beam pattern of the receive antennae employed in the current system. It may be desirable to incorporate a more realistic receiver beam pattern

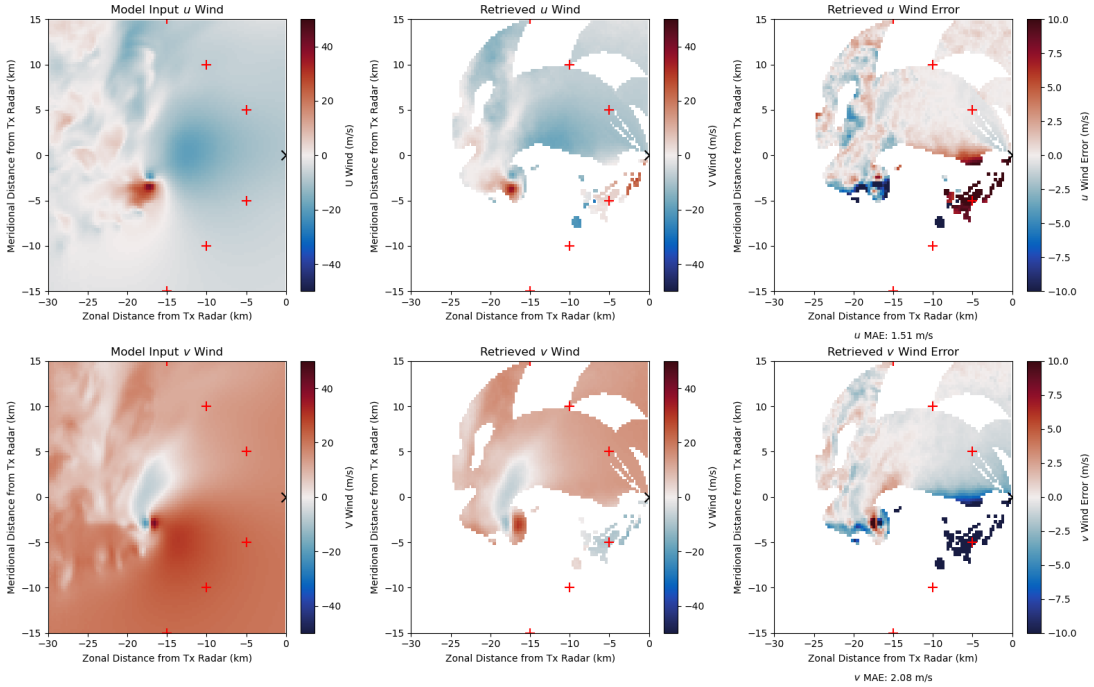


Figure 4.18: Similar to Figure 4.14, but using an emulated phased-array pattern without sidelobe whitening.

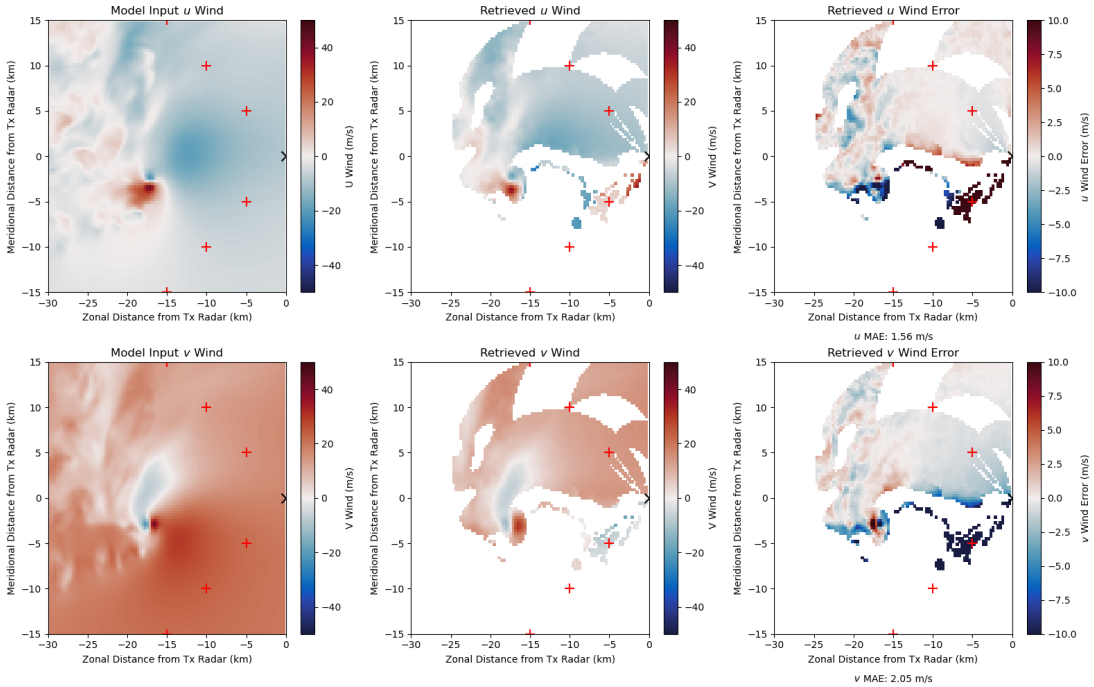


Figure 4.19: Similar to Figure 4.18, but retrieved using data from the 3 best receivers per grid point per Equation 3.5.

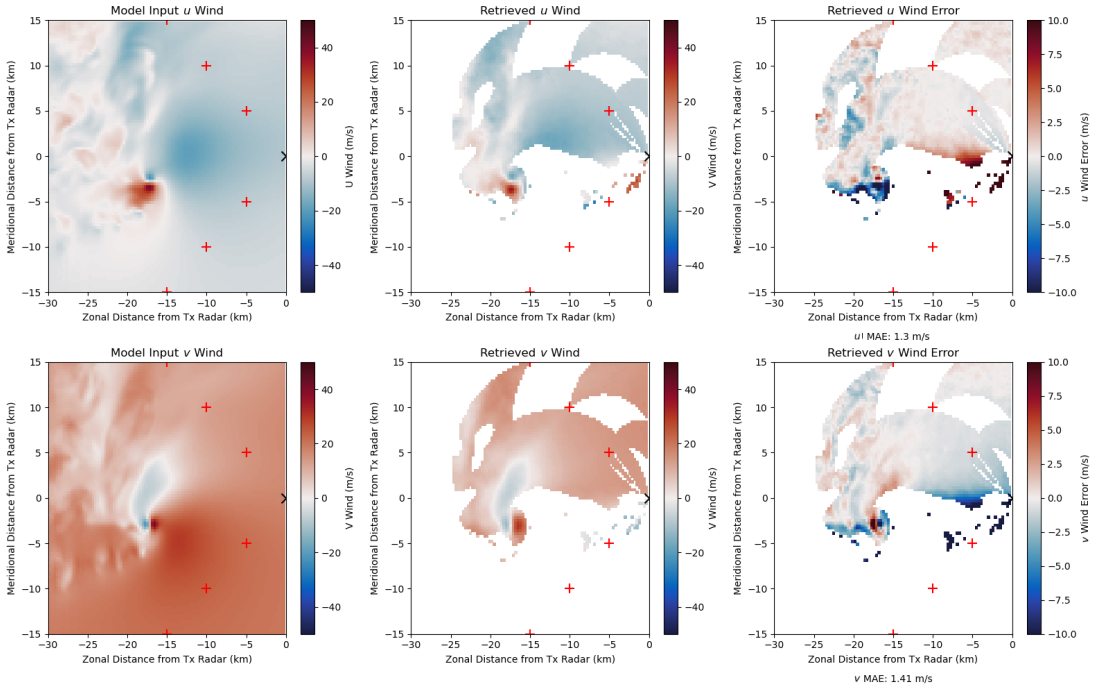


Figure 4.20: Similar to Figure 4.18, but with sidelobe whitening.

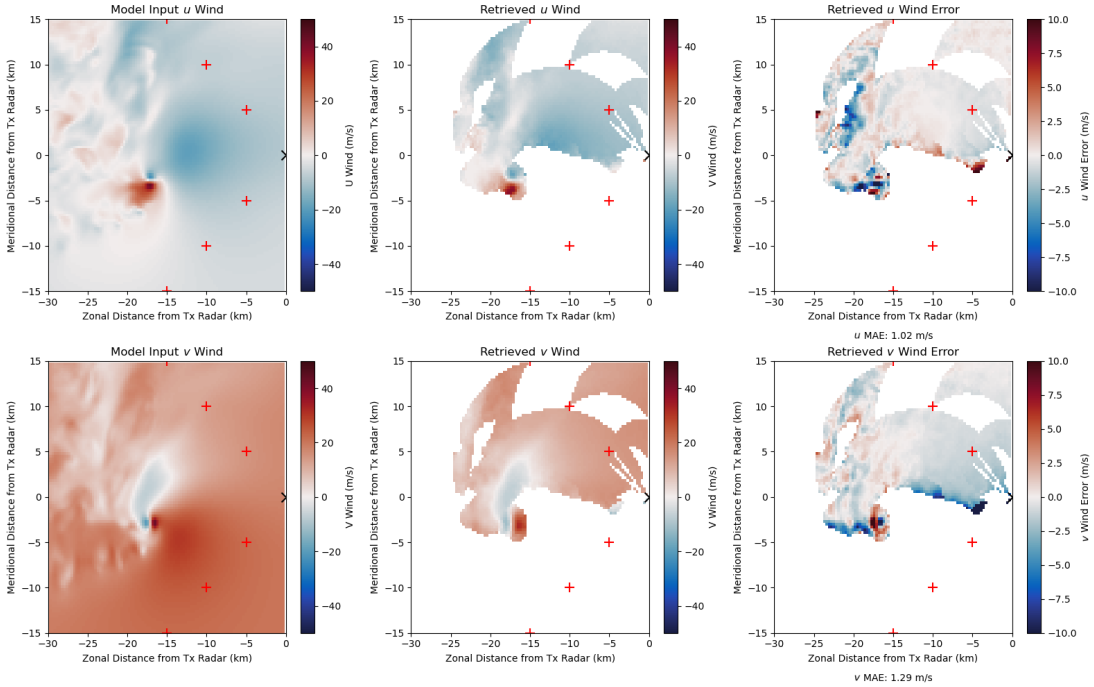


Figure 4.21: Similar to Figure 4.20, but retrieved using data from the 3 best receivers per grid point per Equation 3.5.

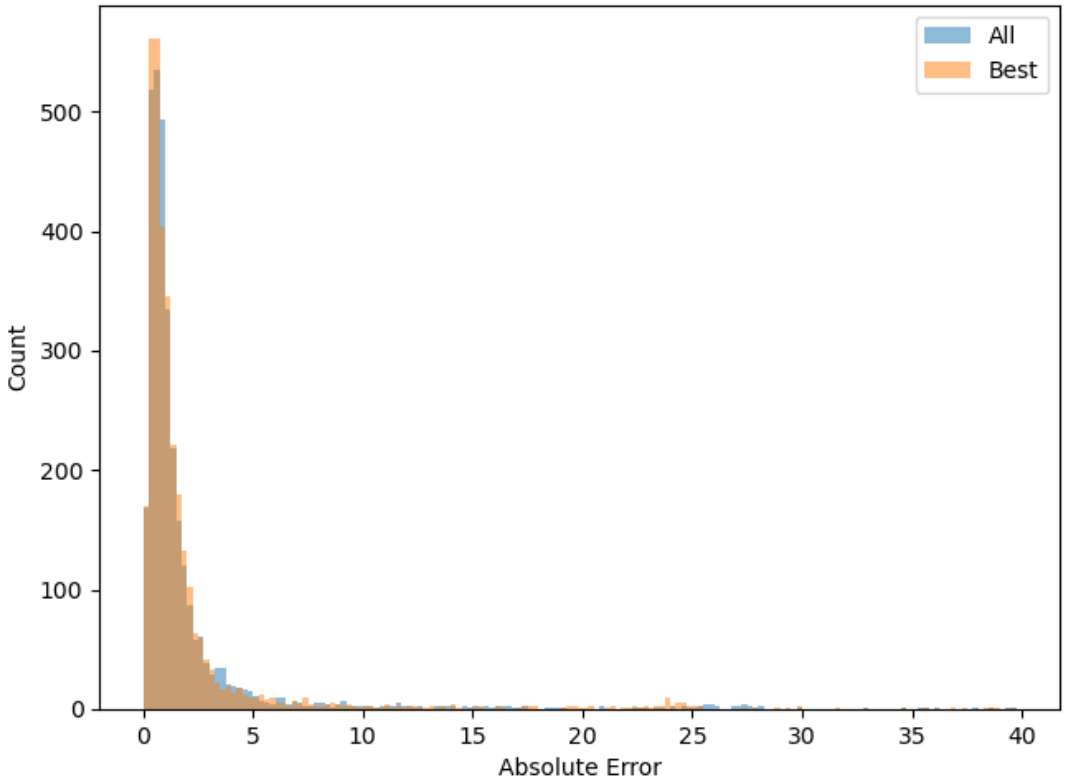


Figure 4.22: Similar to Figure 4.16, but using an unwhitened phased-array pattern.

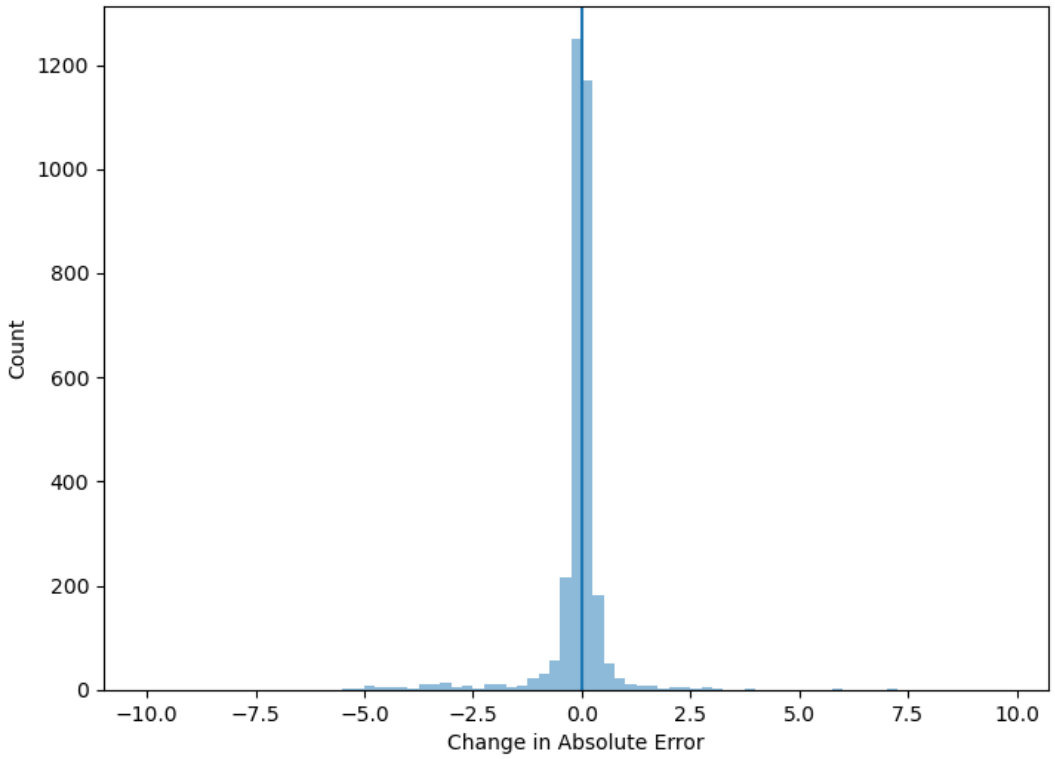


Figure 4.23: Similar to Figure 4.17, but using an unwhitened phased-array pattern.

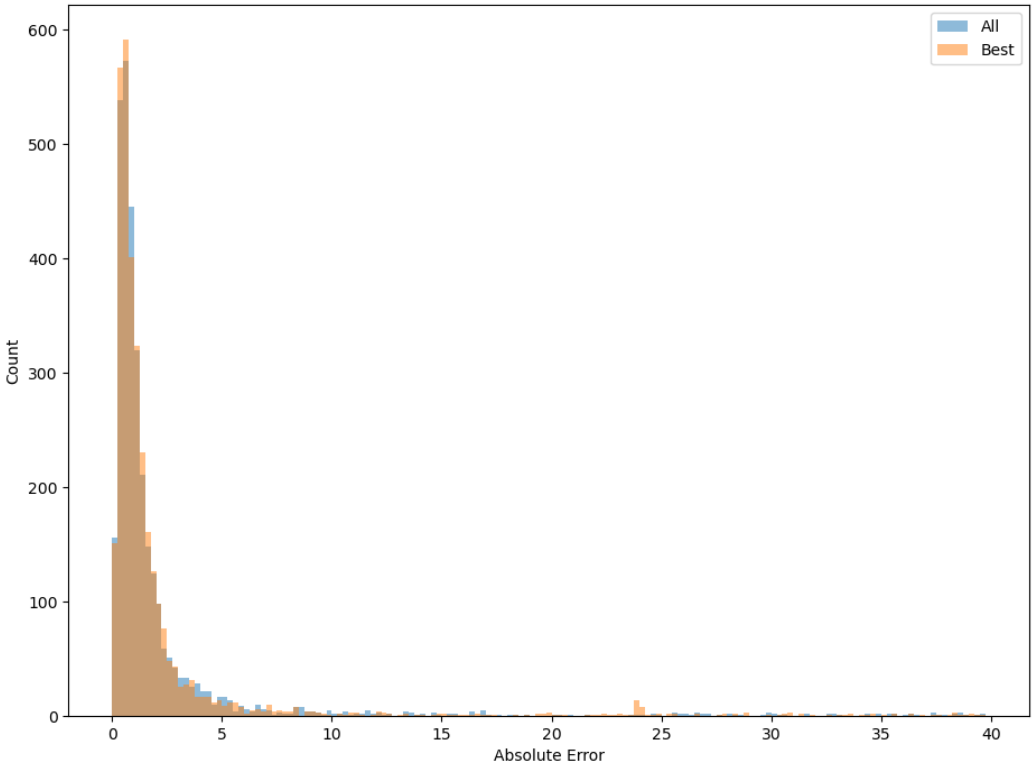


Figure 4.24: Similar to Figure 4.22, but with sidelobe whitening.

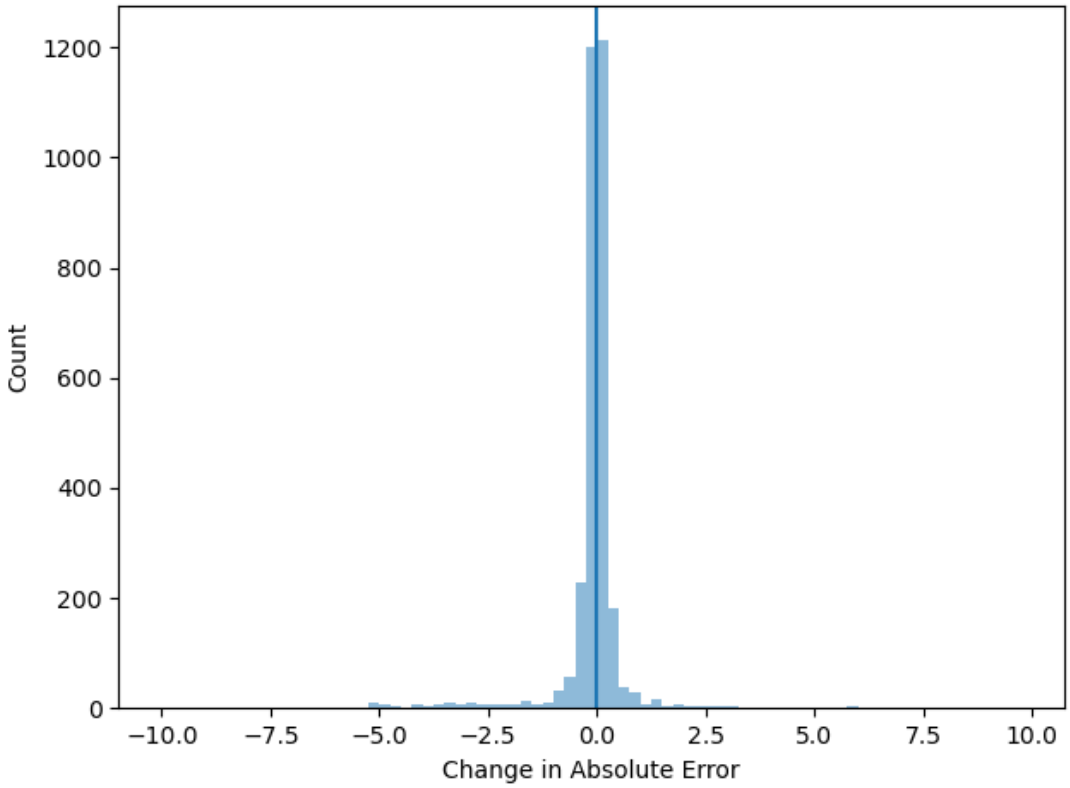


Figure 4.25: Similar to Figure 4.23, but with sidelobe whitening.

and angular beam positioning in the bistatic radar simulator for future studies exploring exact network layouts. However, it is not anticipated that the anomalously broad beam pattern on receive will affect the overall generality of these results. Second, the sidelobe test pattern (Figure 4.5) does not vary in elevation, meaning that the only contributions to sidelobe contamination would be in azimuth. In the real atmosphere, sidelobe contamination can arise from reflectivity gradients in both azimuth and elevation, so the magnitude of contamination would be underestimated by excluding gradients in elevation. However, the radial symmetry of all transmit patterns about the main beam axis means that the magnitude of sidelobe contamination in azimuth should be quite similar to that from elevation, so any results under this symmetry should hold with respect to receiver geometry in general. Finally, these experiments neglect the direct retrieval of vertical velocity due to the shallow scanning angles of the transmitting radar, which yield little of the vertical component of velocity. It is entirely possible that a ground-based multistatic system optimized for highly-constrained direct retrievals of vertical velocity could have a different layout than what is presented here; the necessity of a bistatic angle close to 90 $^{\circ}$ in the range-height plane would likely require the baseline(s) to contract in length, though this would also limit the horizontal limits of the retrieval domain. However, it stands to reason that a system with numerous receivers could simply nest a subset of receivers dedicated for vertical velocity measurements within a larger network used for horizontal wind measurements.

## 4.2 Observations with Multistatic Radar

As noted before, a prototype multistatic system of two bistatic receivers has been deployed for several years in the Oklahoma City, Oklahoma metropolitan area, cen-

tering on the KTLX WSR-88D as a transmitter of opportunity. The previous simulations of a three-receiver (1 Tx/Rx, 2 Rx) network showed that reasonable 2D wind retrievals are achievable, even with a dish antenna as an illuminator. We now seek to demonstrate the capabilities of such a network in practice via observations of convective events. Three notable cases with sufficient bistatic data to produce a 2D or 3D wind retrieval will be shown, along with an additional case having insufficient bistatic data for a retrieval, but which is still informative to the capabilities of the current bistatic receivers.

### 4.2.1 Notable Retrievals

#### 25 May 2019 Mesoscale Convective System

The evening of 25 May 2019 brought a weakening mesoscale convective system (MCS) through the Oklahoma City metropolitan area, which produced a few reports of severe winds. The MCS progressed through the multistatic retrieval domain Figure 4.26 in a direct W-to-E fashion, providing an excellent test for retrieving a nearly uniform zonal wind field. Data from both receivers was available for a period of approximately 15 minutes, along with corresponding monostatic data from the KTLX and KCRI WSR-88Ds. Thus, the bistatic retrieval in this case will only address the horizontal wind field, as the corresponding dual-monostatic retrieval would be less-suited for a full 3D retrieval. The results of the three analysis periods homologous to the three KTLX volumes are shown in Figures 4.27 to 4.29. All three retrievals demonstrate the general agreement between the multistatic and dual-monostatic retrievals in the horizontal wind field in the lowest 3 km of the atmosphere, as all show a strong westerly wind field, generally around $10\ \mathrm{m\,s^{-1}}$ in magnitude, which backs to southerly with height at the same magnitude. This verti-

cal pattern in the wind field is persistent though the observed evolution of the MCS, even as the leading edge passes over KTLX. The most glaring difference between the retrievals occurs in the lowest 1 km, where the multistatic retrieval has much stronger flow near the western edge of the domain, whereas the dual-monostatic remains similar to the rest of the domain. This could be explained by poor bistatic dealiasing in the lowest WSR-88D tilts, particularly the 0.5 degree tilt, as the effective Nyquist velocity of the surveillance scan at this elevation is low. Otherwise, the data quality of this case is high, given good bistatic geometries across the domain and little apparent sidelobe contamination, since the spatial gradients in reflectivity and velocity should be minimal within the trailing stratiform region of the MCS.

**28 April 2020 Supercell Complex**

On the afternoon of 28 April 2020, a series of closely-spaced supercells developed along a southward-advancing cold front through central Oklahoma. As the supercells congealed into a QLCS and progressed southeast across the Oklahoma City metro, many instances of severe hail were observed. One particular cell in the western part of the region produced several instances of baseball-sized (2.75-3") hail along a path from Mustang to west of Norman Figure 4.30. A considerable time series of full bistatic data spanning 6 WSR-88D volumes ($\sim$50 minutes) was collected during this period of hail production, allowing for some characterization of the evolution of the embedded supercell's 3D wind structure. Plan position plots Figures 4.31, 4.32, 4.36, 4.39 and 4.40 and vertical cross-sections Figures 4.34 and 4.37 show a consistent region of intense upward motion oriented along the convective line and positioned towards the rear flank of the line. This corresponds to the ascending branch of an elongated rotor-like feature within the line, clearly seen in the cross-section plots. Wurman (1994) analyzed a remarkably similar feature

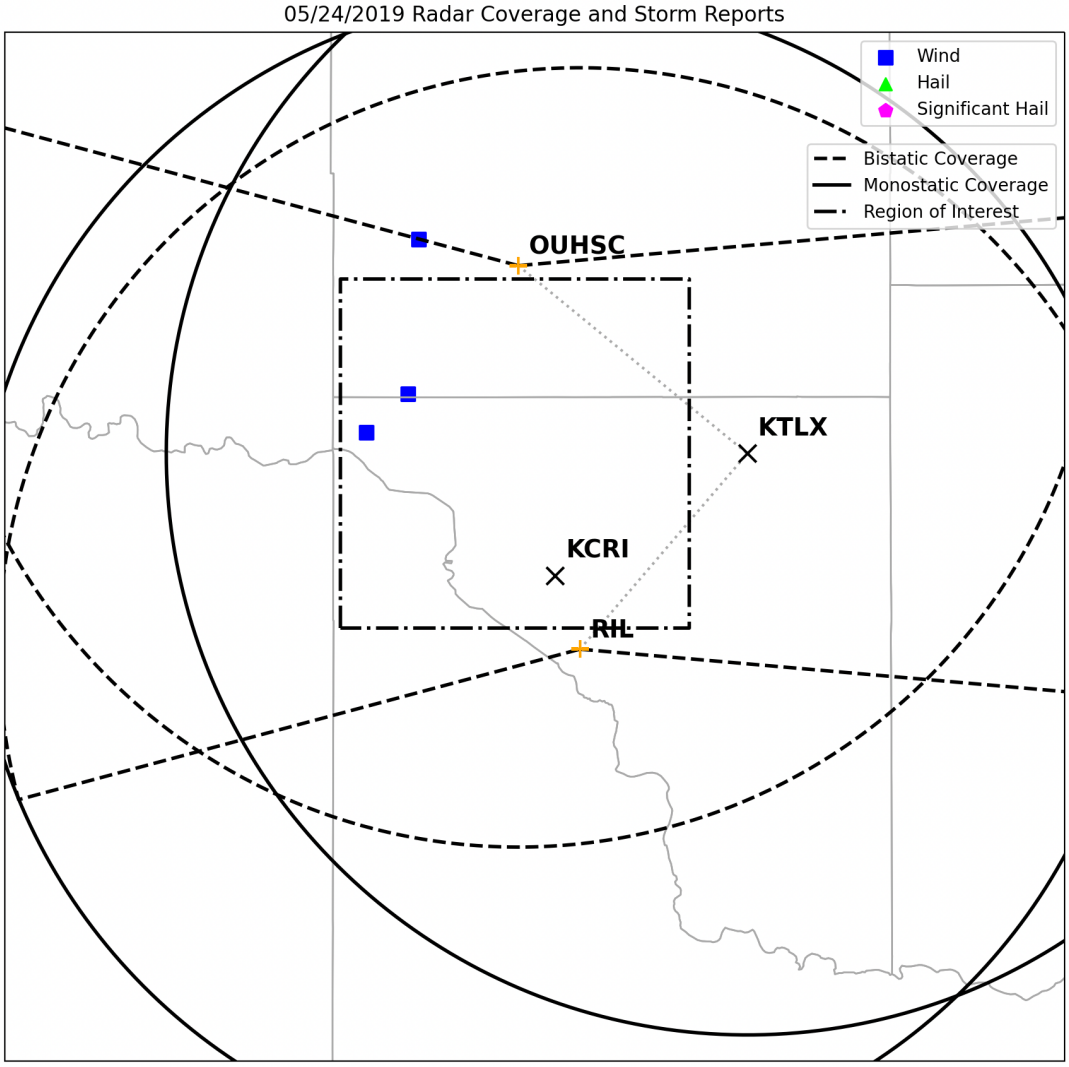


Figure 4.26: Locations of the monostatic radars (solid black), bistatic receivers (dashed black), multi-Doppler region of interest (dit-dashed black), and local storm reports for the 25 May 2019 MCS case.

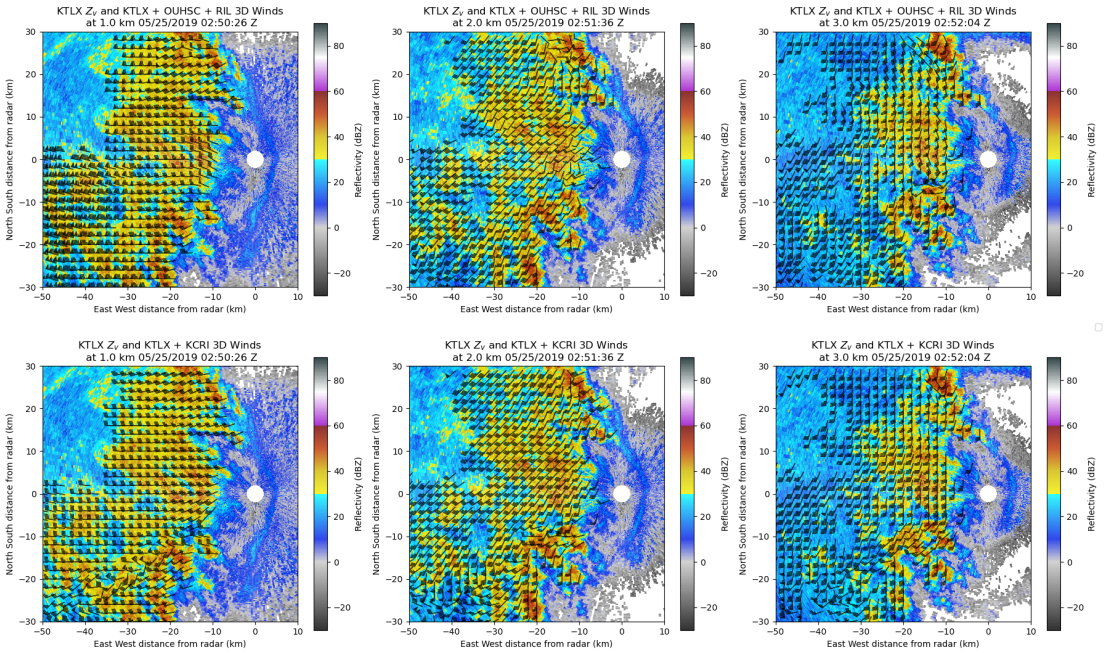


Figure 4.27: KTLX reflectivity and retrieved horizontal winds at 1 km (left), 2 km (center), and 3 km (right), valid at 0250Z on 25 May 2019. Retrievals in the top row are from the RIL and OUHSC bistatic data combined with the KTLX monostatic data, and the bottom row is derived from the KCRI and KTLX monostatic data.

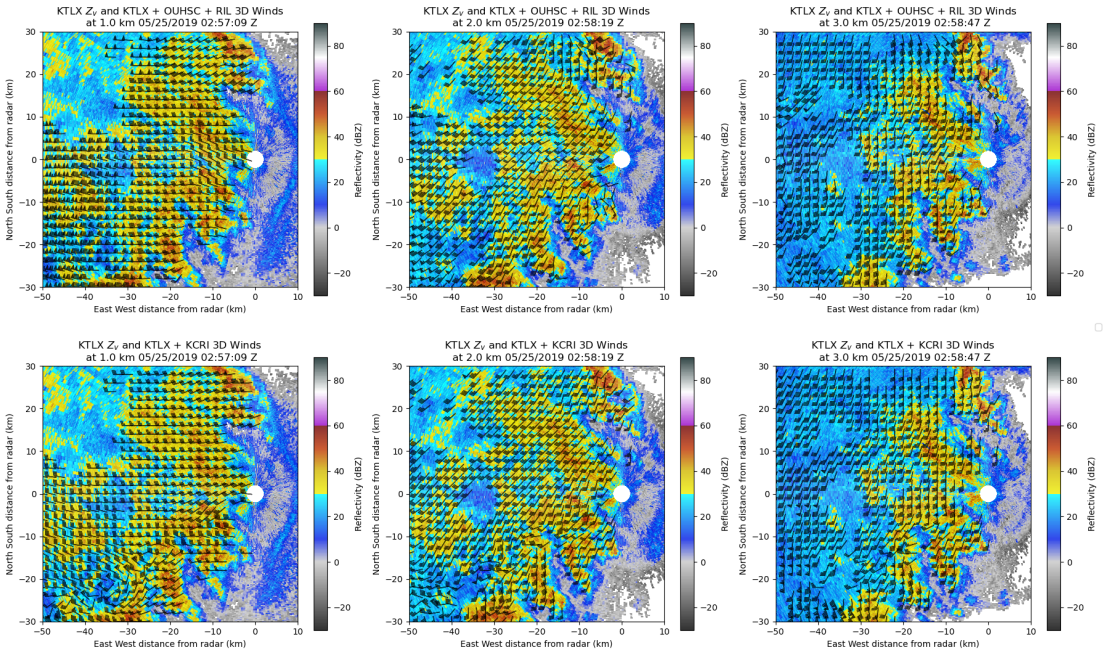


Figure 4.28: Similar to Figure 4.27, but valid at 0257Z on 25 May 2019.

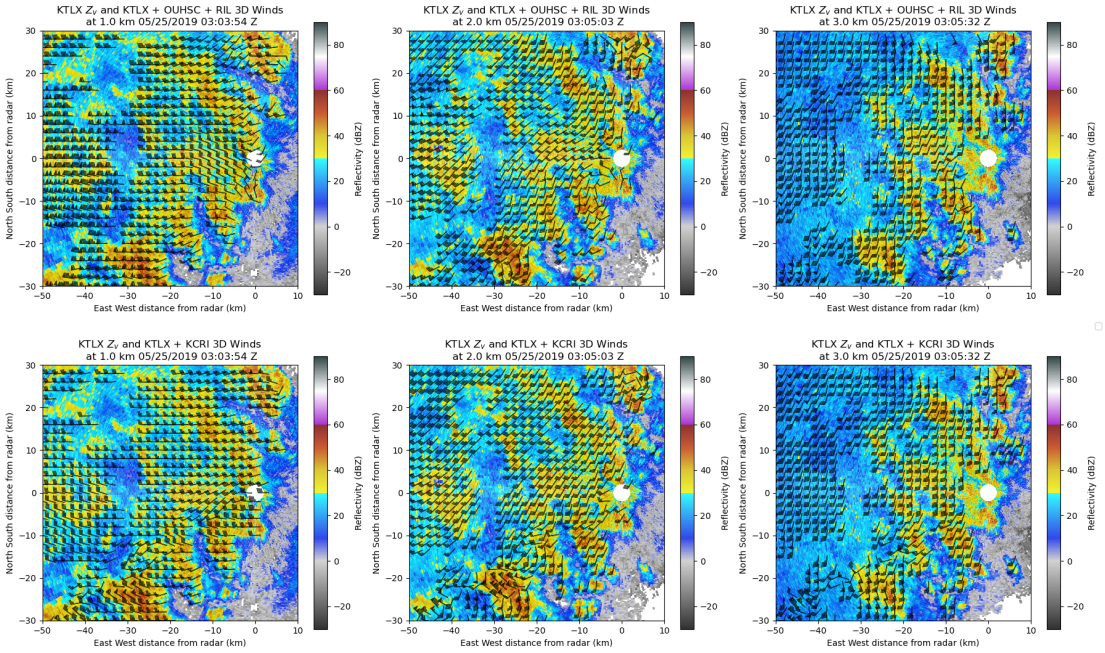


Figure 4.29: Similar to Figure 4.28, but valid at 0303Z on 25 May 2019.

within a hail-producing storm, albeit much weaker in magnitude. However, the updraft within this line is also likely tied to the presence of a series of mesocyclones within the mid-levels, as evidenced by a distinct alternating pattern of strong cyclonic and anticyclonic vertical vorticity analyzed in that layer. The structure of the updraft is fairly consistent through the analysis period, remaining elongated along a southwest to northeast axis on the rear flank of the line. The intensity of the updraft fluctuates from relatively weak at the beginning of the period (Figure 4.31), to fairly intense (Figure 4.36), then weakening towards the end of the period (Figure 4.40). This cyclic pattern of intensification and weakening appears to roughly align spatiotemporally with the reports of severe hail (Figure 4.30), where the beginning of the analysis period corresponds to the weak phase after the significant hail production in the far northern portion of the domain, and the second weakening phase corresponds to the severe hail reports in the southern half of the domain. Confir-

mation of these trends with respect to hail production would likely necessitate the computation of hail trajectories, which Brook et al. (2021) demonstrated as being effective in nowcasting hail production and size.

A detailed quantitative analysis of the storm features is not quite feasible here, given the coarse vertical resolution of the WSR-88D volume coverage pattern (VCP), which in turn limits the vertical resolution of the bistatic data and subsequent wind retrieval. Thus, the reader is cautioned that the updraft magnitudes developed within this and other syntheses from this system could be spurious, since the boundaries of the vertical integration of the continuity equation are not well constrained. Nevertheless, the sheer quantity of significant hail and agreement with conventional multi-monostatic Doppler retrieval leads to reason that the persistent, intense region of upward motion developed in the bistatic retrieval is likely genuine. It remains unknown how much sidelobe contamination is present within these observations, and it seems likely that there should be some contamination given the sheer volume and size of hail present. However, there is little evidence of any clear-air sidelobe contamination in the received power, suggesting that the only regions of sidelobe contamination are within the weather regions and are thus extremely difficult to discern, perhaps due to the orientation of the convective line relative to the bistatic baselines. The lack of obvious sidelobe contamination could also be explained by differences in hail production and characteristics between this complex case and cases involving more typical hail-producing convection (i.e., single-cell and discrete supercell storms), though this is quite speculative and would require further investigation.

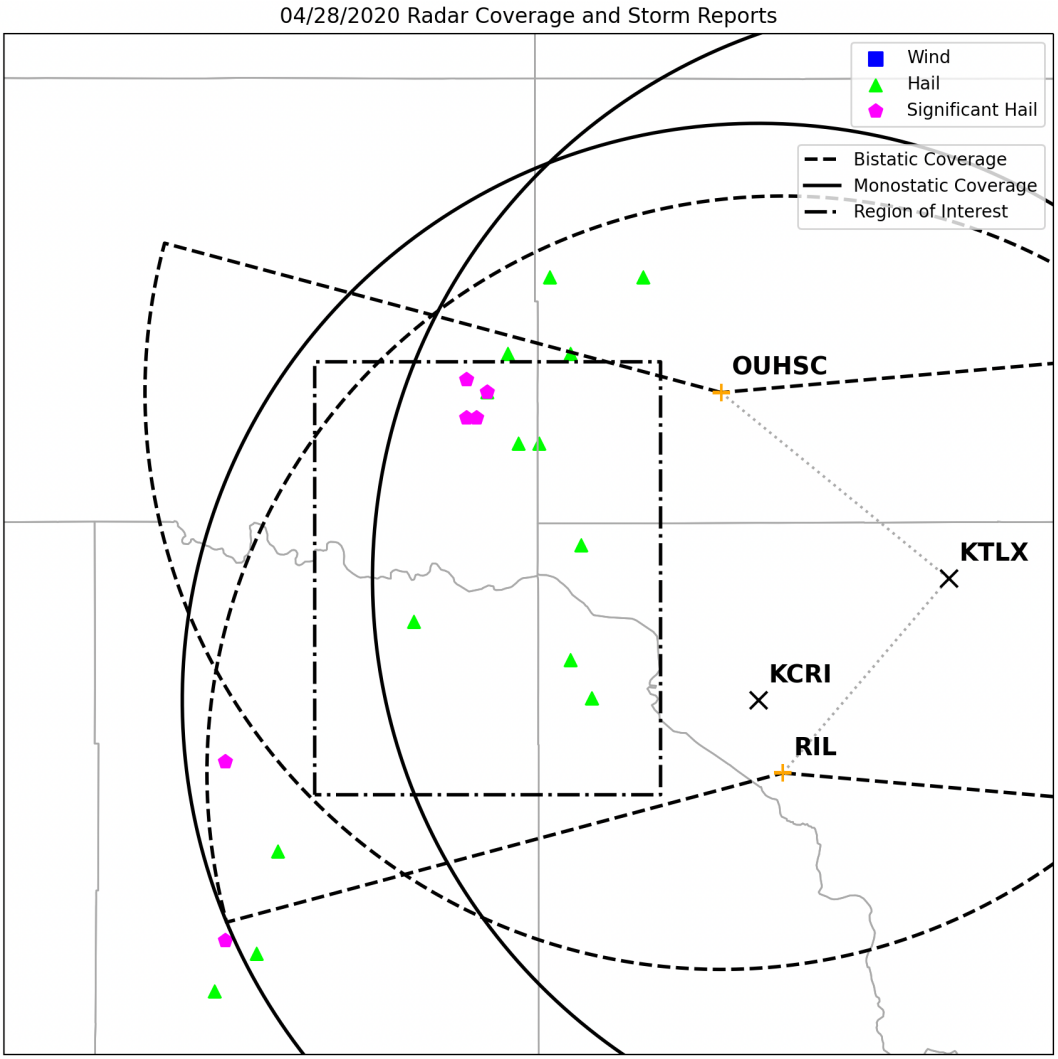


Figure 4.30: Similar to Figure 4.26, but for the 28 Apr 2020 case.

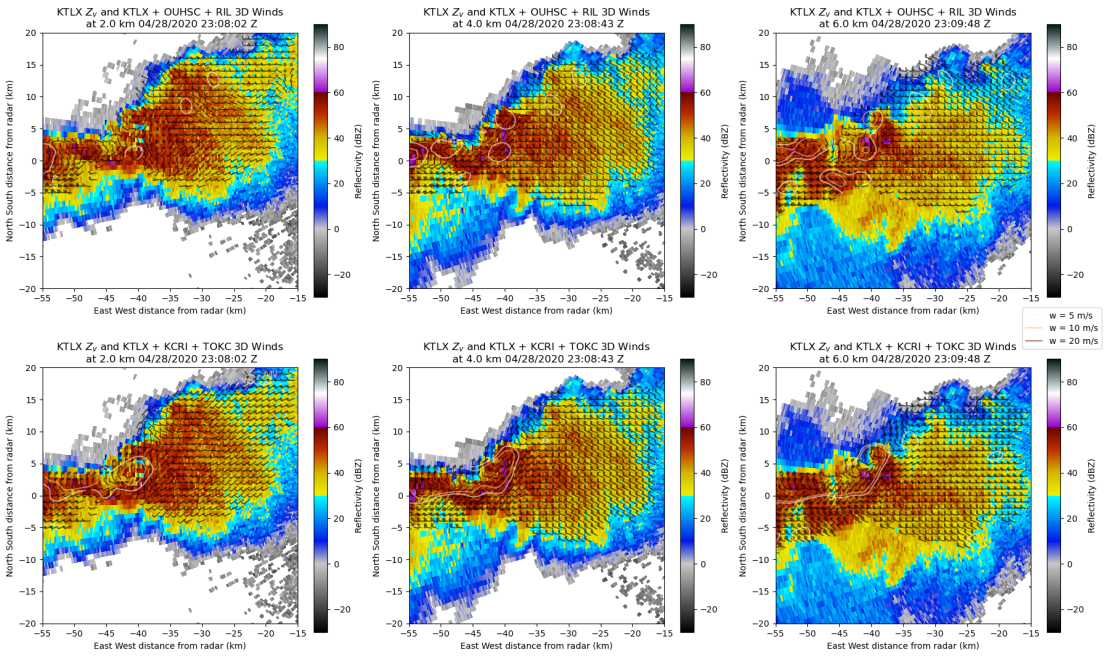


Figure 4.31: KTLX reflectivity and retrieved horizontal winds at 1 km (left), 2 km (center), and 3 km (right), valid at 2308Z on 28 April 2020. Retrievals in the top row are from the OUHSC bistatic data combined with the KTLX monostatic data, and the bottom row is derived from the PX-1000, TOKC, and KTLX monostatic data.

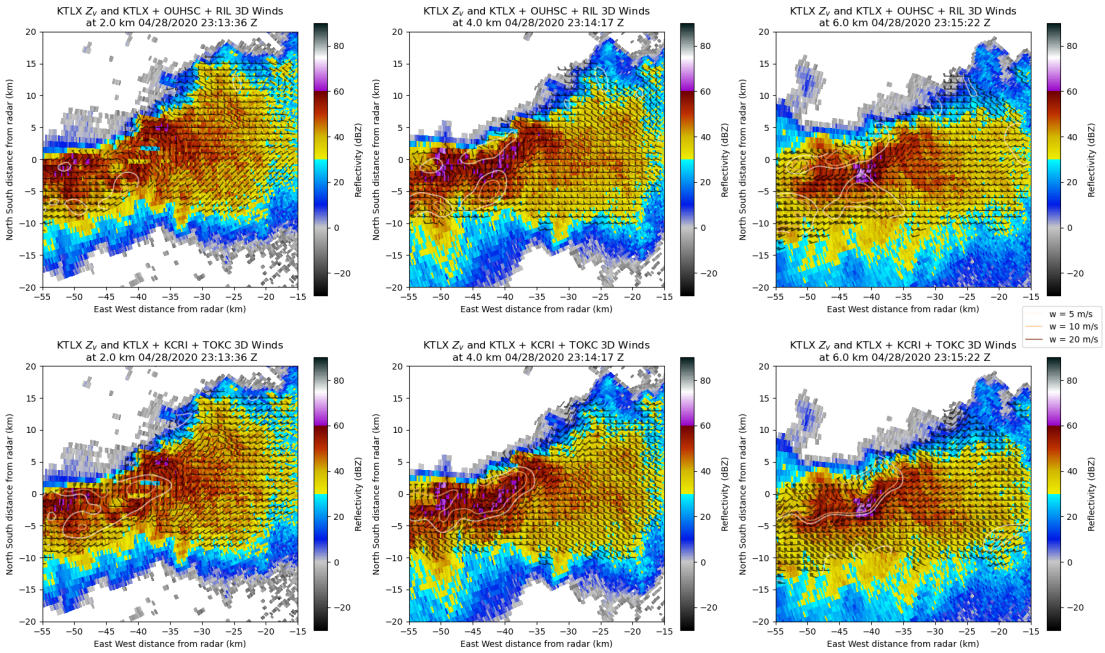


Figure 4.32: Similar to Figure 4.31, but valid at 2313Z 28 April 2020.

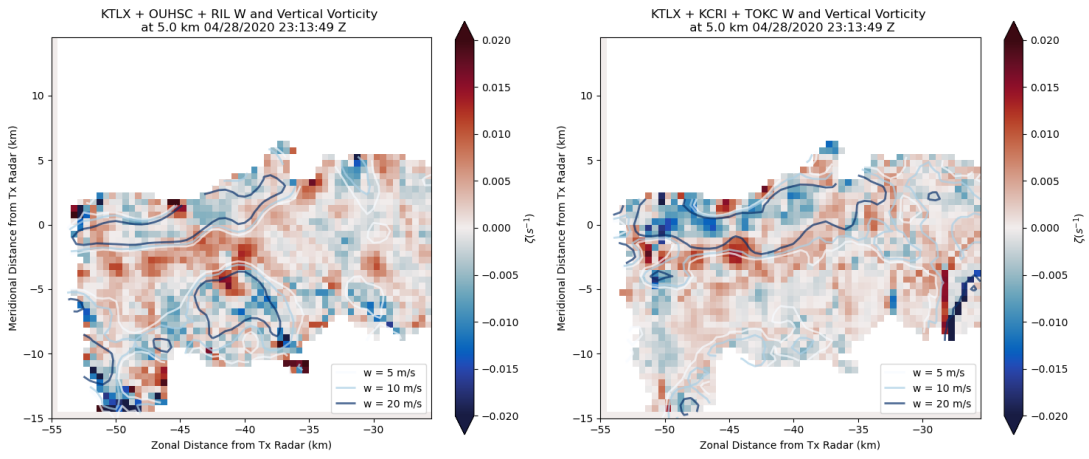


Figure 4.33: Horizontal cross-sections of retrieved $\zeta$ (fill) and $w$ (contours) at 5 km ARL. The bistatic retrieval is on the left, and the multi-monostatic retrieval is on the right.

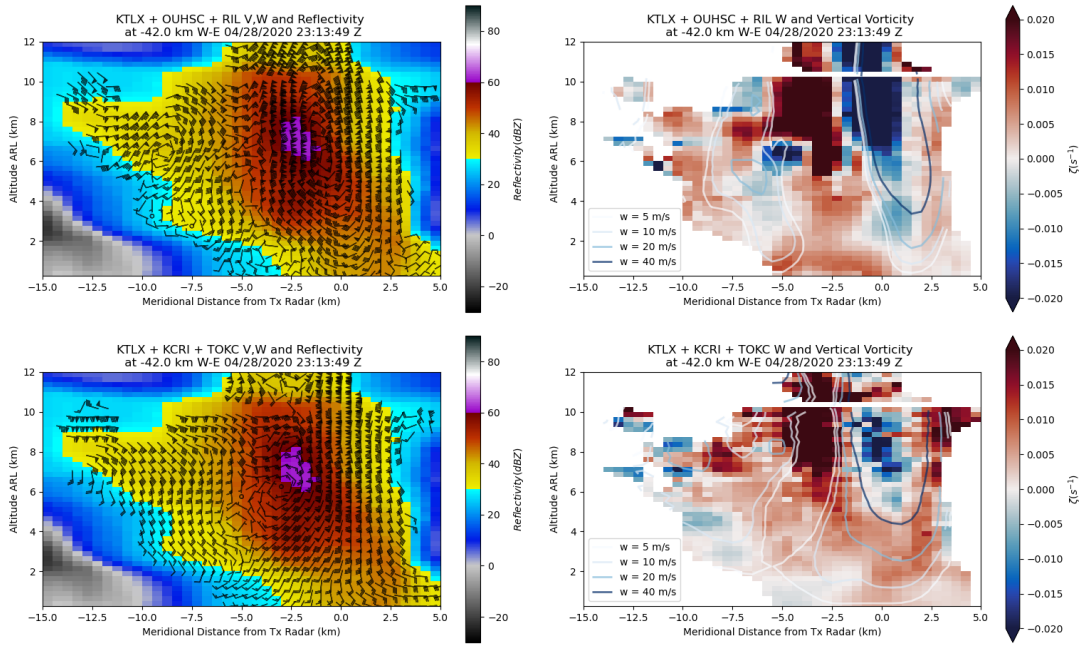


Figure 4.34: N-S cross sections of retrieved $\zeta$ (fill) and $w$ (contours) located 43.5 km west of KTLX. The bistatic retrieval is on the left, and the multi-monostatic retrieval is on the right.

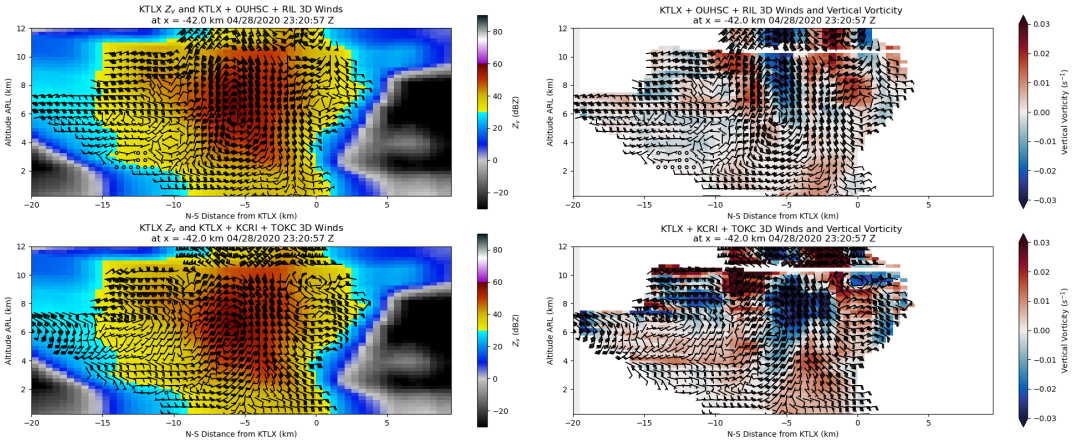


Figure 4.35: N-S cross sections of retrieved $\zeta$ (fill) and $w$ (contours) located 43.5 km west of KTLX. The bistatic retrieval is on the left, and the multi-monostatic retrieval is on the right.

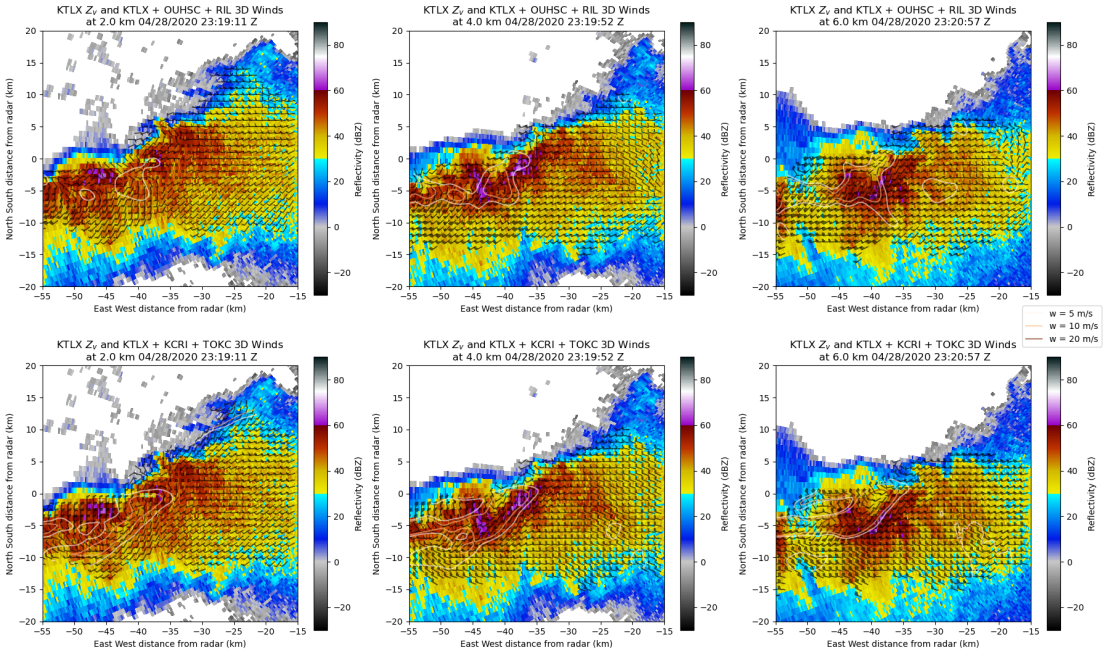


Figure 4.36: Similar to Figure 4.31, but valid at 2320Z 28 April 2020.

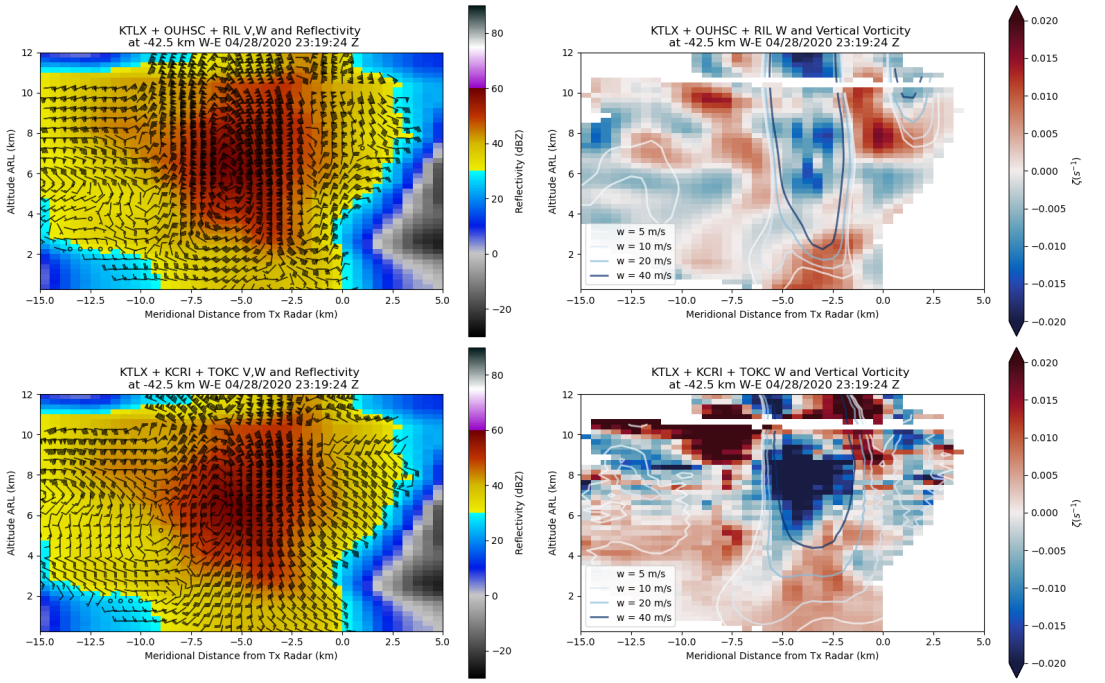


Figure 4.37: N-S cross sections of retrieved $\zeta$ (fill) and $w$ (contours) located 43.5 km west of KTLX. The bistatic retrieval is on the left, and the multi-monostatic retrieval is on the right.

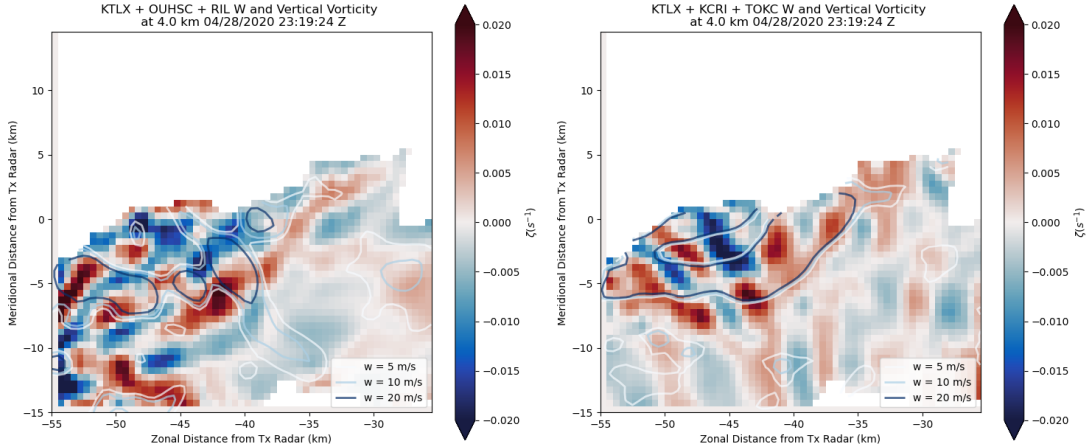


Figure 4.38: Similar to Figure 4.33

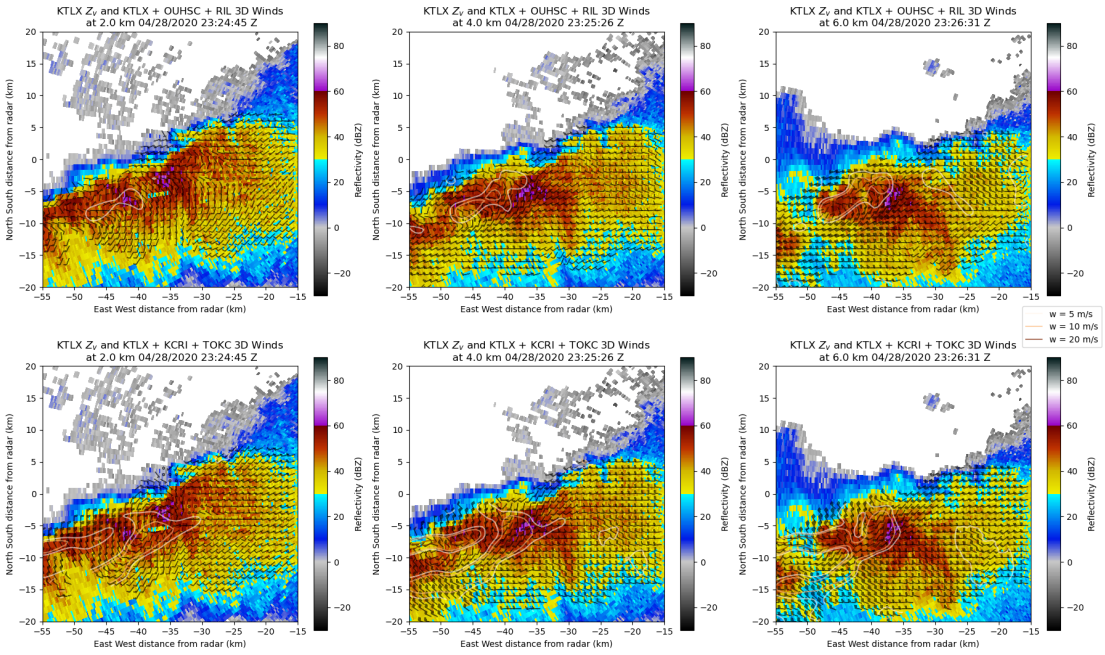


Figure 4.39: Similar to Figure 4.31, but valid at 2324Z 28 April 2020.

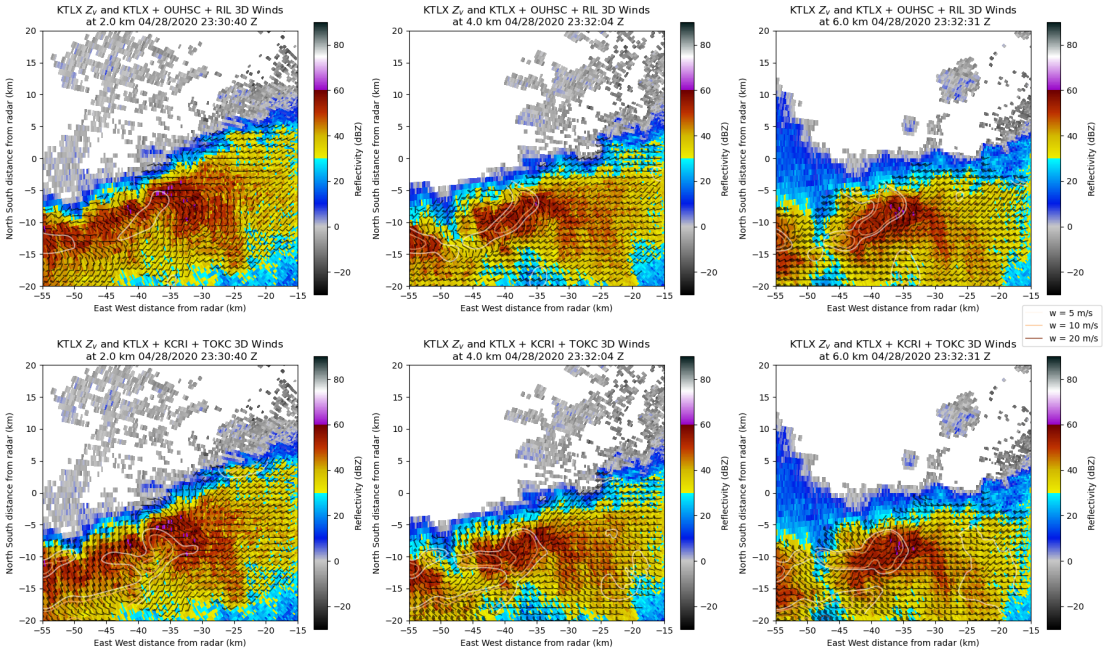


Figure 4.40: Similar to Figure 4.31, but valid at 2330Z 28 April 2020.

### 31 August 2020 Supercell

On the afternoon of 31 August 2020, a mature supercell with a history of significant hail production entered the Norman area around 2200 UTC, moving slowly to the east. Over the next 90 minutes, the storm produced copious amounts of hail over Norman and points to the south and east, with several reports of 2-inch hailstones noted. Given that the storm tracked directly over the RIL bistatic site, data from that receiver was generally unusable due to extremely poor bistatic geometries. As a result, a dual-Doppler analysis was only possible between KTLX and the OUHSC bistatic receiver over a limited region, though the supercell is fully within the region. Regardless, the quality of this retrieval is somewhat suspect given bistatic angles at or below 30° . Additionally, the bistatic data collected only spans approximately 30 minutes due to connectivity issues during the event. Thankfully, there was a plethora of monostatic radar data available for this case from the KTLX and

KCRI WSR-88Ds, the TOKC TDWR, and the ARRC's PX-1000 radar (Cheong et al., 2013). Taken together, this group of radars is able to provide a robust multi-Doppler retrieval over the same area as the bistatic retrieval Figure 4.41. Much like the previous case, the bistatic and monostatic multi-Doppler retrievals Figures 4.42 and 4.43 agree in a qualitative sense, with both showing an intense mesocyclone in a three-dimensional sense (high vertical vorticity coupled with a strong updraft). This is further bolstered by comparisons of horizontal cross-sections (Figure 4.45) and vertical cross-sections (Figures 4.45 and 4.46), which all show broad agreement in the structure and intensity of vertical vorticity. The evolution of the updraft is difficult to fully discern over only two analysis periods, but there does appear to be a notable increase in updraft intensity between 2223z and 2233z, which corresponds to a definite improvement in the supercell's appearance in reflectivity. The cross-sectional analyses also support this, depicting a noticeable increase in the maximum updraft magnitude in the 6-8 km AGL layer within the mesocyclone. As with the previous case, this increase in updraft magnitude does precede the production of large hail, as evidenced by the apparent hail core aloft (Figure 4.47) and later reports of large hail in the Norman area.

The bistatic retrieval does have a stark region of sidelobe contamination jutting out azimuthally from the hail core aloft, especially at higher elevation angles Figure 4.47. This manifests in the bistatic wind retrieval as a region of anomalously strong horizontal winds within the bounded weak echo region (BWER), which appears to yield an anomalously strong updraft, albeit in the correct location. The primary cause of this degree of sidelobe contamination is clearly a high concentration of large hail aloft As with the previous case, the magnitudes of the bistatic retrieved vertical velocities are likely suspect. However, the asynchronous nature of the monostatic data could yield significant errors in the exact placement and in-

tensity of the updraft, meaning that the true intensity of the updraft may very well lie in between the multistatic and monostatic retrievals. Regardless, the utility of such retrievals cannot be understated from a forecasting perspective, as even a basic indication of a strong updraft and mesocyclone would be highly beneficial to effective nowcasting of convective threats.

### 4.2.2 Other Notable Cases

#### 26 May 2019 QLCS

On the evening of 26 May 2019, a severe QLCS impacted the Oklahoma City metropolitan area, producing many instances of severe winds and a handful of brief tornadoes. One of these tornadoes occurred within the bistatic domain Figure 4.48, in extreme western Cleveland County, Oklahoma. This tornado was weak (rated EF0) and short-lived, but occurred nearly simultaneously with a low-level WSR-88D scan. While data were available from both receivers during this event, the data from the RIL receiver was significantly degraded due to receiver beam blockage from buildings located west and northwest of the receiver. As a result, a dual-Doppler analysis of this case was not attempted, but the data still warrants examination. The OUHSC data clearly depict an appendage in the range-corrected power field, which corresponds to a weak circulation in the bistatic velocity field. The fact that the receiver is able to resolve this circulation is notable, since QLCS misocyclones are typically small, fast-moving, and ahead of most precipitation. In addition, this may be among the first-ever observations of a tornadic circulation with a bistatic weather radar.

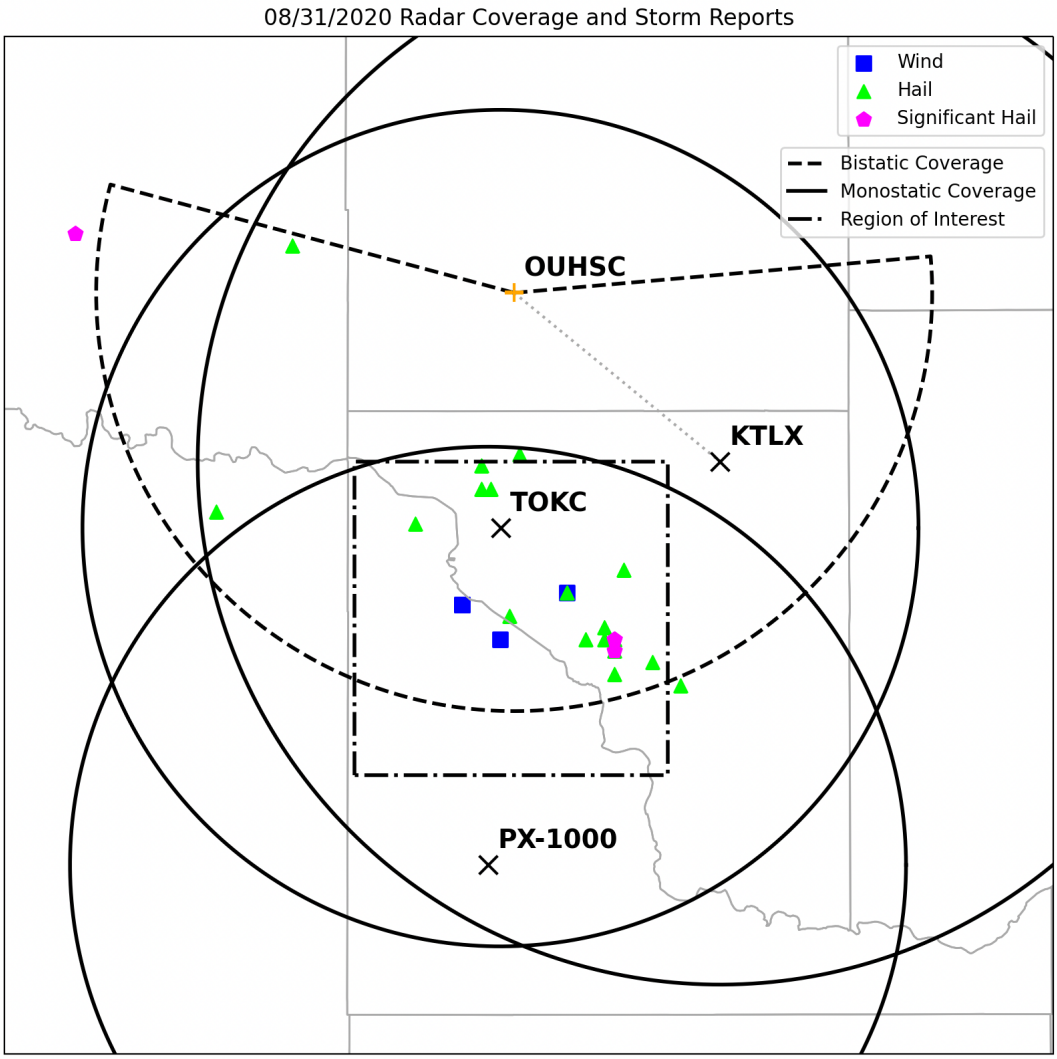


Figure 4.41: Similar to Figure 4.30, but for the 31 Aug 2020 case.

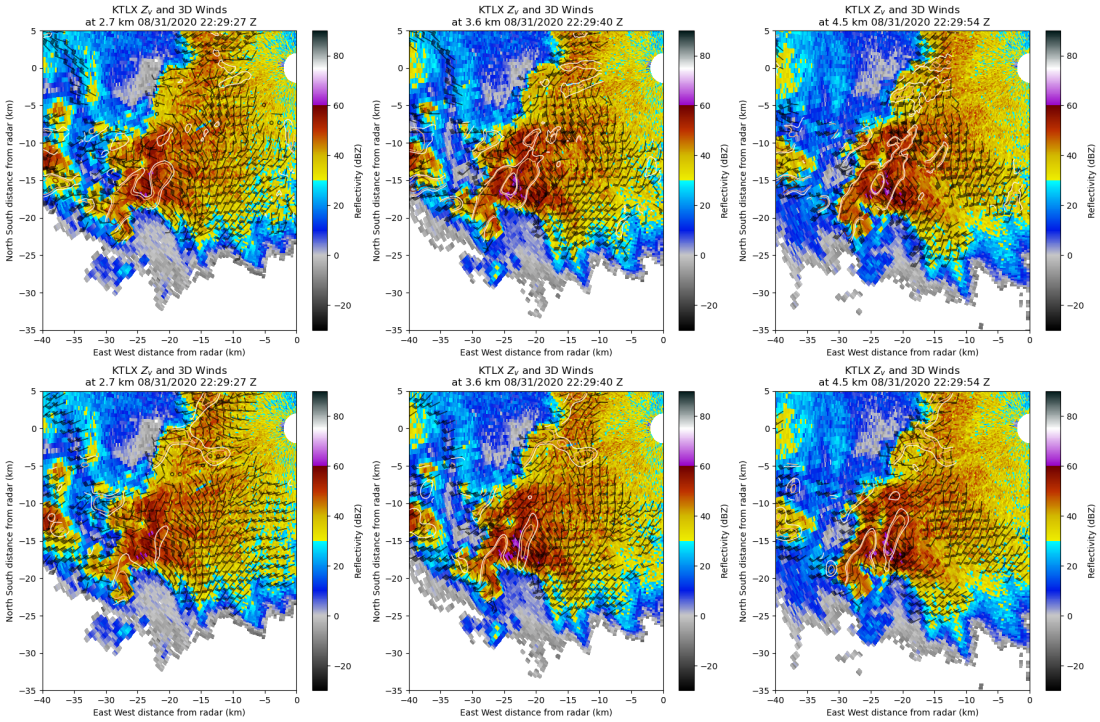


Figure 4.42: KTLX reflectivity and retrieved horizontal winds at 3.6 km (left), 4.5 km (center), and 5.4 km (right), valid at 2223Z on 31 August 2020. Retrievals in the top row are from the OUHSC bistatic data combined with the KTLX monostatic data, and the bottom row is derived from the PX-1000, TOKC, and KTLX monostatic data.

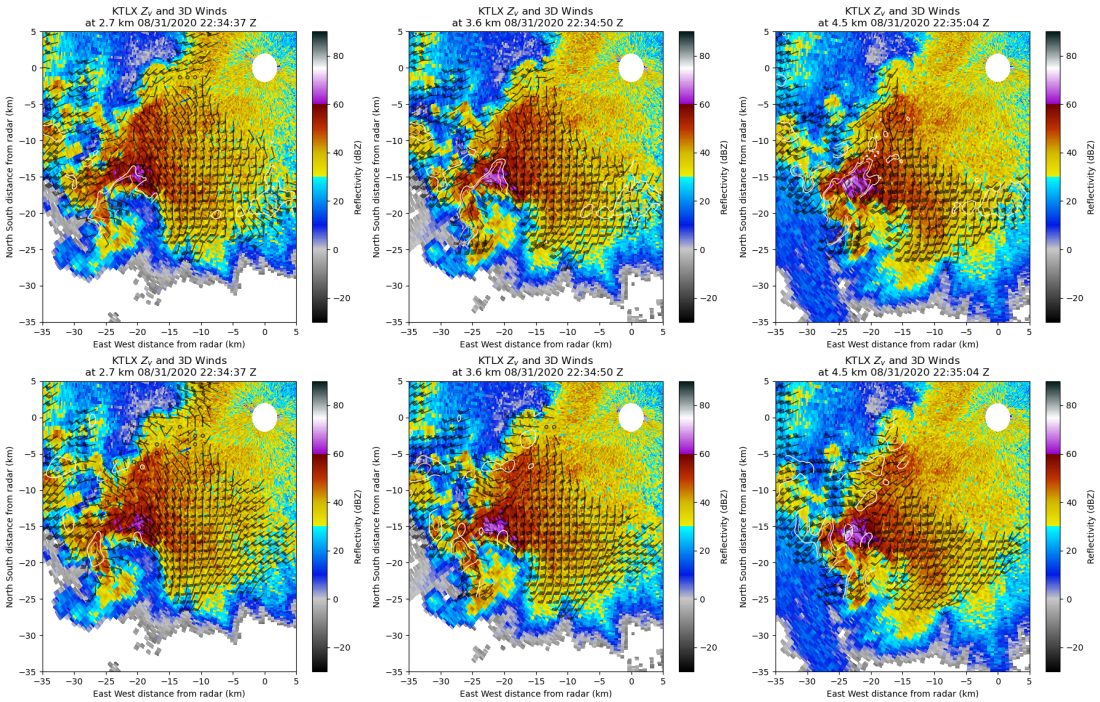


Figure 4.43: Similar to Figure 4.42, but valid at 2233Z 31 August 2020.

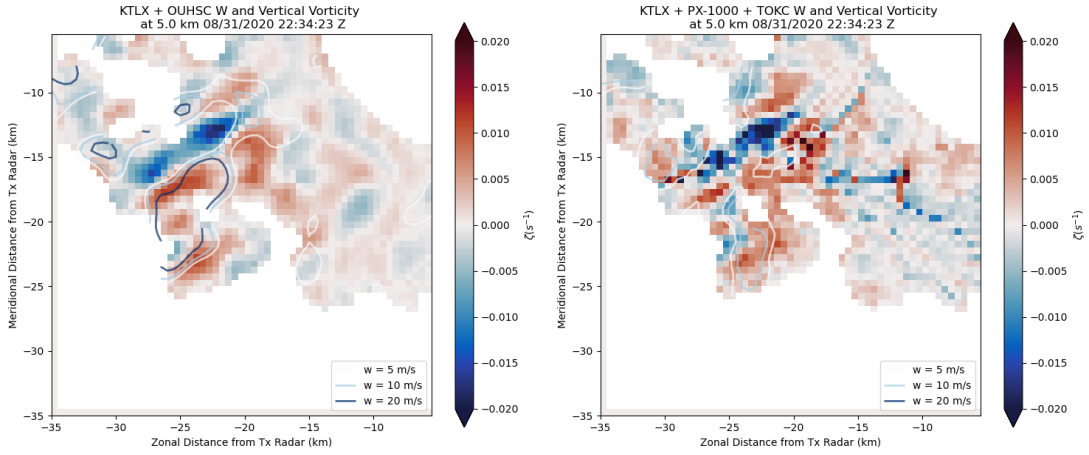


Figure 4.44: Horizontal cross-sections of retrieved $\zeta$ (fill) and $w$ (contours) at 5 km ARL. The bistatic retrieval is on the left, and the multi-monostatic retrieval is on the right.

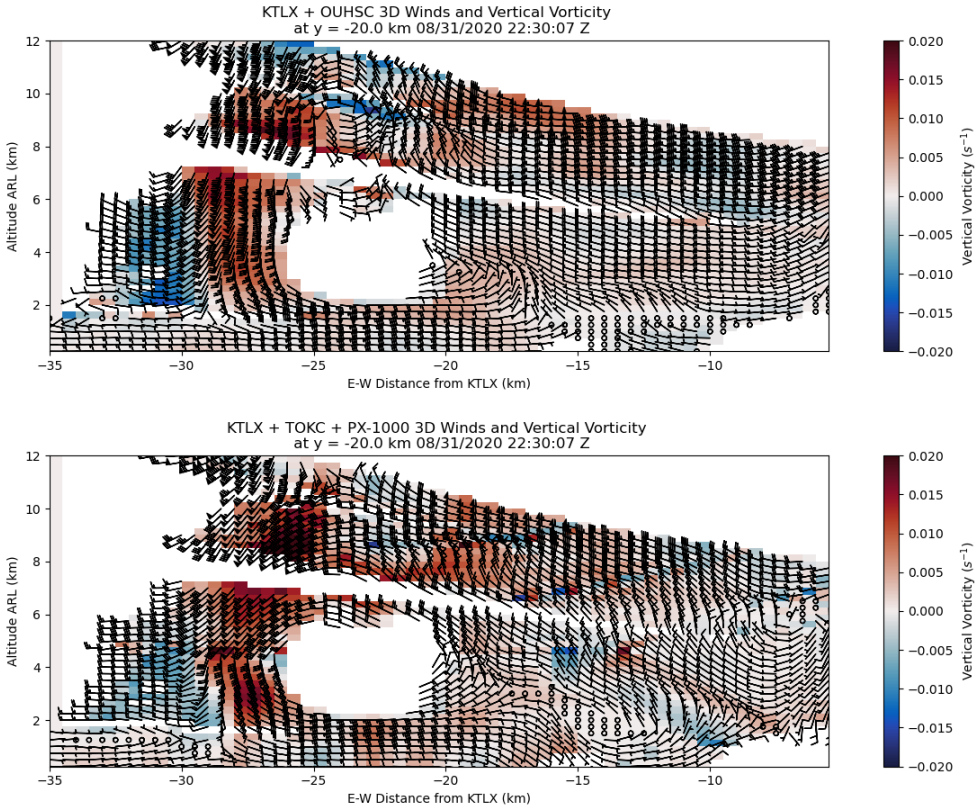


Figure 4.45: E-W cross sections of retrieved $\zeta$ (fill) and $u$, $w$ (barbs) located 20 km south of KTLX, valid at 2230Z 31 Aug 2020. The bistatic retrieval is on the top, and the multi-monostatic retrieval is on the bottom.

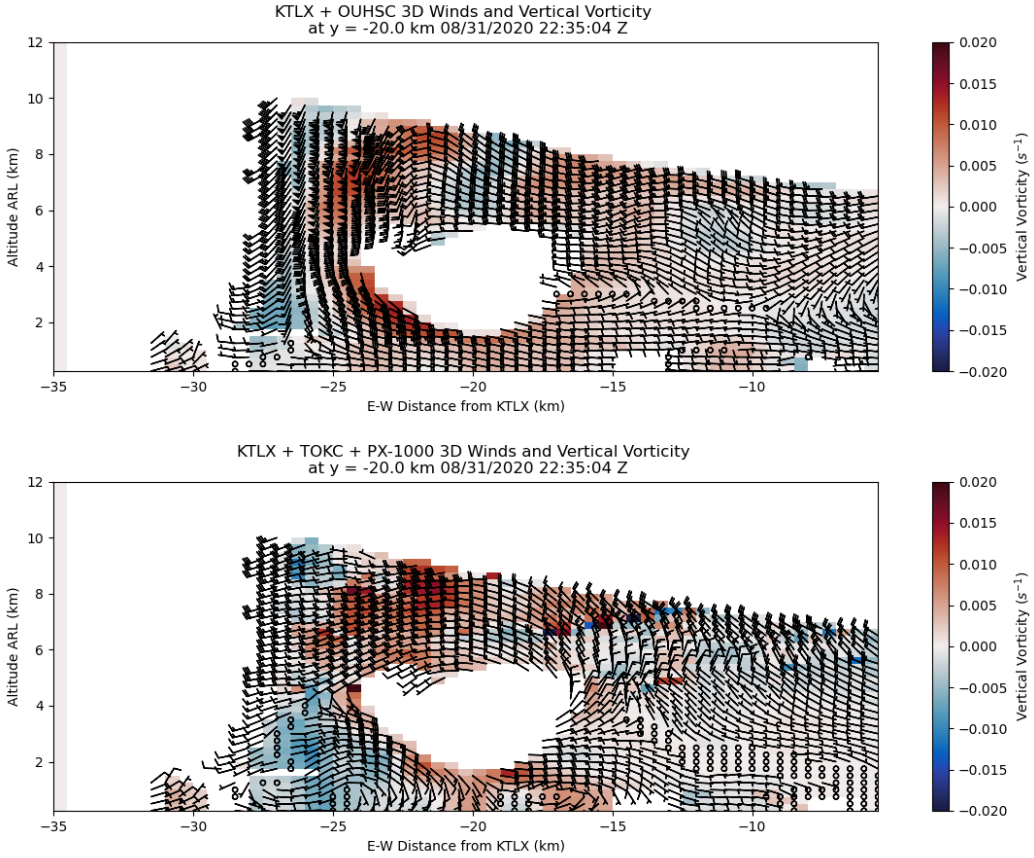


Figure 4.46: Similar to Figure 4.45, but valid at 2235Z 31 Aug 2020.

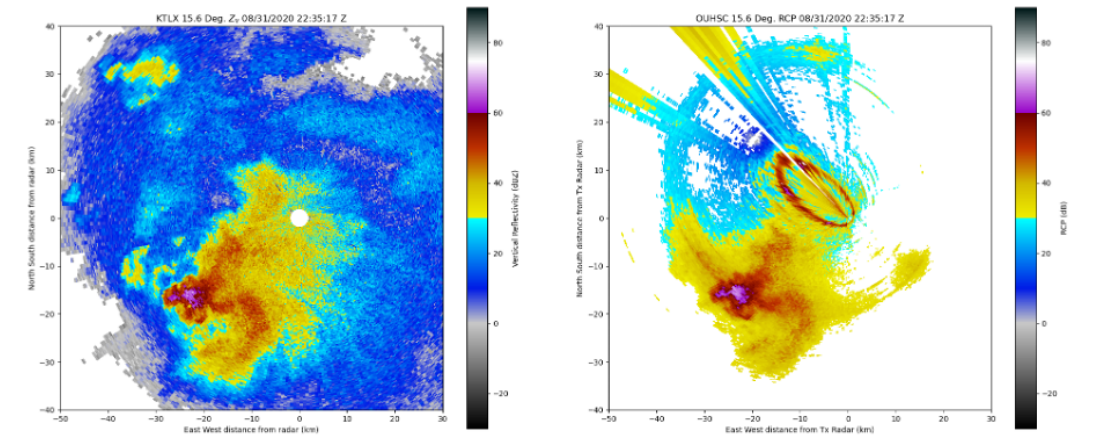


Figure 4.47: Reflectivity PPIs at 15.4 degree elevation from KTLX (left) and the OUHSC receiver (right) of the 31 Aug 2020 supercell.

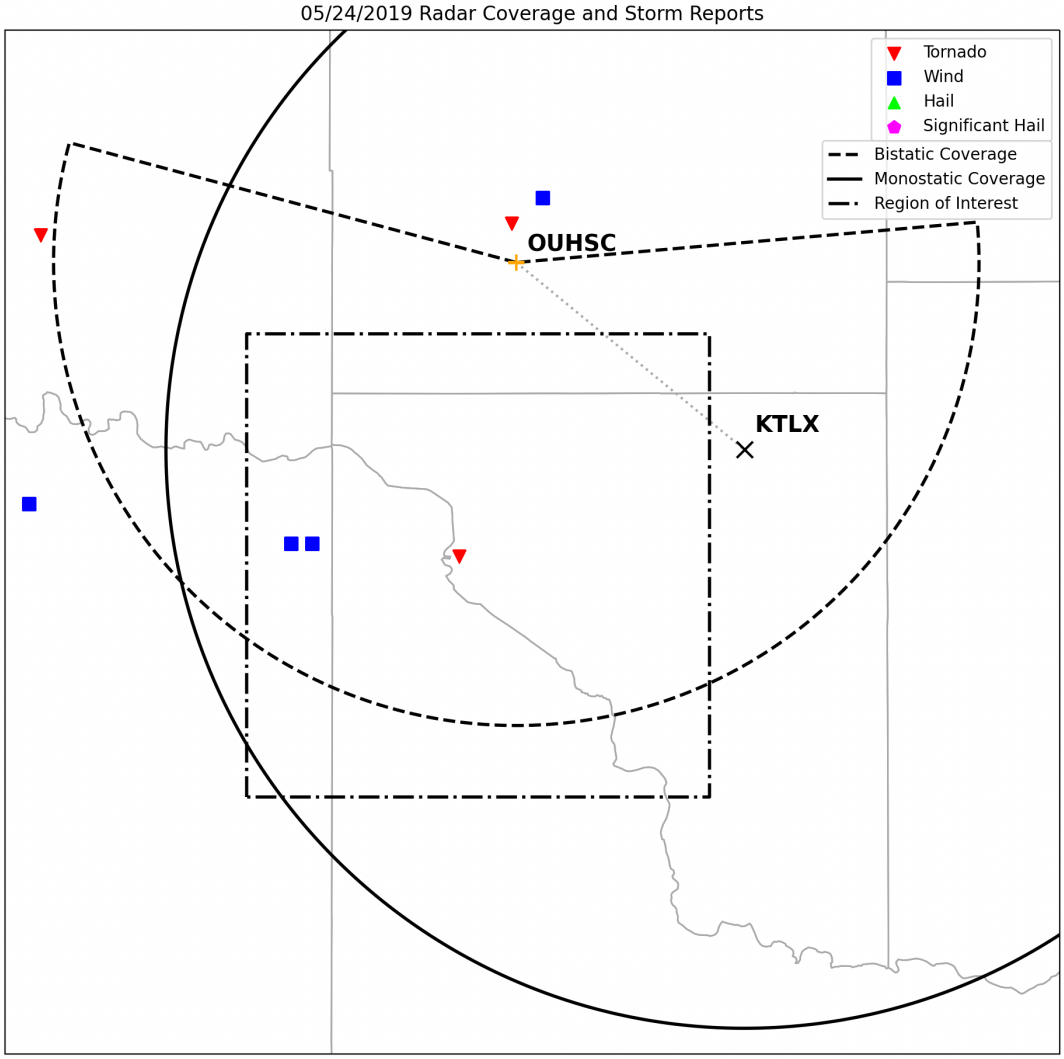


Figure 4.48: Similar to Figure 4.41, but for the 26 May 2019 case.

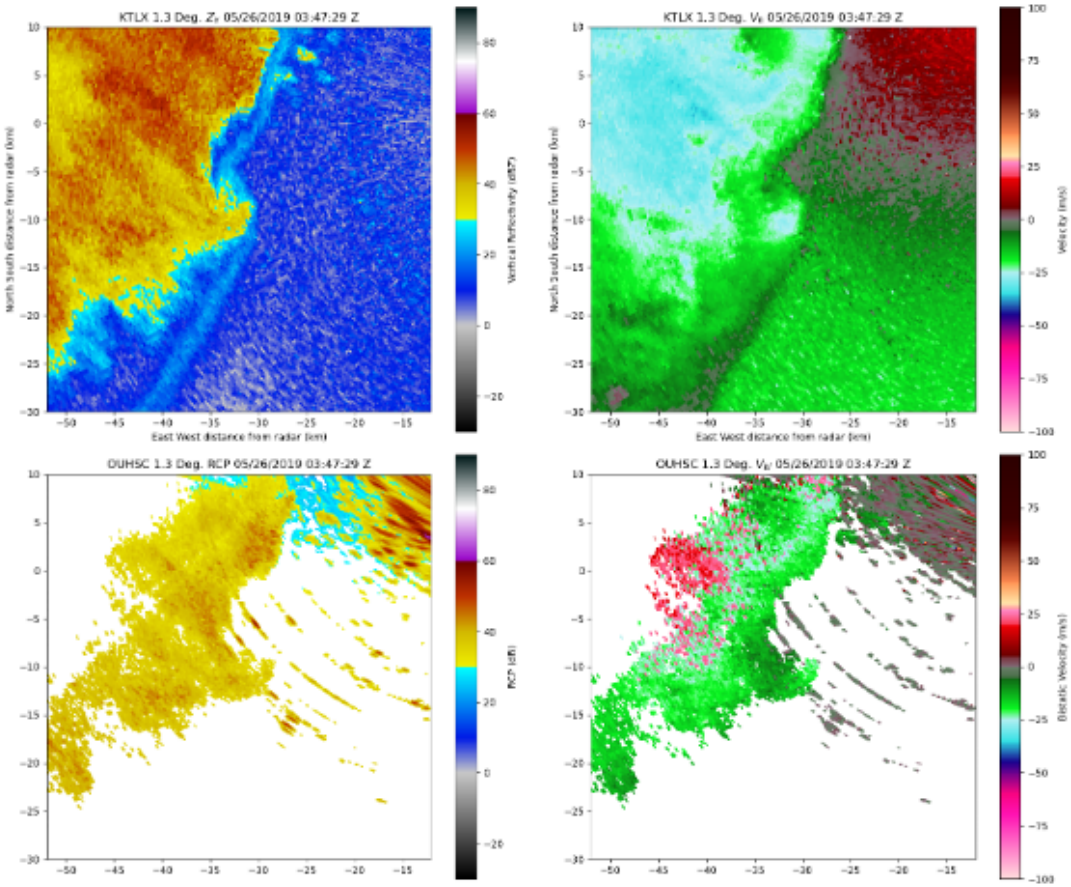


Figure 4.49: Reflectivity (left) and radial velocity (right) PPIs at 1.3 degree elevation from KTLX (top) and the OUHSC receiver (bottom)

# Chapter 5

# Conclusions and Future Work

## 5.1 Conclusions

Given the previous analysis results, observations of convection with the current prototype multistatic network are quite promising. The retrievals of horizontal wind fields are plausibly accurate when compared to multi-monostatic retrievals, and 3D wind retrievals do seem feasible, even with sub-optimal scanning strategies and a small network. Features across scales, from broad cold pools to mesocyclones to even miscyclones are resolvable and analyzable within the bistatic moment data. The implications of this ability are broad, especially when considering that the current network only consists of two receivers and the extremely low unit cost per receiver (generally less than $5,000 in the worst case).

The multi-Doppler analyses performed with bistatic data are comparable to simultaneous multi-Doppler analyses done with monostatic radars when comparing horizontal wind fields and general structures of vertical winds and derived fields. However, the poor vertical resolution of the illuminating monostatic radar fundamentally limits the retrieval capabilities of the current network. Sidelobe contamination is apparent in some cases, especially those with known occurrences of large hail. The primary limitations to the current multistatic network are low sensitivity,

sidelobe contamination, and few receivers. This motivates how to improve the network, particularly how to expand the network and how to reduce sidelobe contamination, as improving sensitivity would likely necessitate higher costs from a larger receiving antenna. Simulations of isotropic networks with increasing numbers of receivers show that improvements in network coverage and retrieval performance occur up to six receivers, after which there is little to no improvement. Simulations of a fixed network with varying beam patterns show that sidelobe whitening is able to provide some benefit to retrieval quality via reduction of sidelobe contamination, but this improvement is marginal, at least compared to the improvements from increasing receiver counts. Once receiver coverage reaches the point where most analysis points are highly over-determined, it is suggested that a location-based filter could further improve retrieval results by selecting the best subset of receivers based on theoretical bistatic data quality. This technique does improve overall retrieval results by narrowing the distribution of errors via reduction of sidelobe contamination effects. However, the exact filtering method used here is likely suboptimal, implying that further reductions in retrieval error could be possible if a more in-depth strategy is developed. A combination of the previous experiments on a realistic supercell case show that sidelobe whitening and location-based filtering both improve retrieval results through the reduction of sidelobe effects, though the improvements gained by each technique are not mutually exclusive, reinforcing the idea that reducing sidelobe contamination can be achieved without sidelobe whitening.

Taken together, these results imply that further work with dish-based systems could still be fruitful in terms of yielding high-quality bistatic data and wind retrievals, though such systems will require several receivers to achieve tolerable error characteristics across a broad surveillance domain. In addition, a dish-based system

seeking 3D wind retrievals will need an optimized volumetric scanning strategy to ensure proper vertical resolution, as the retrievals done with the coarse vertical resolution of WSR-88D VCPs are not well-constrained at the upper levels, yielding anomalously strong vertical motions. However, if a PAWR-based system is developed, these concerns would be assuaged, given the intrinsic rapid-scan and fine vertical sampling capabilities of such a system. Sidelobe whitening could be explored as a means of reducing the effects of sidelobe contamination. However, if the results of the simulations shown before are to be believed, the improvements gained by sidelobe whitening may be minor compared to the improvements made by increasing receiver count for a given area.

## 5.2 Future Work

Given that the primary method to improve retrieval quality for a dish-based network is to increase the number of bistatic receivers, the immediate focus for future work on the ARRC's S-band bistatic network is to do so, with at least 3 additional receiver units planned for implementation in the near future. This network will primarily be illuminated by the KTLX WSR-88D (2910 MHz), though the ability to be illuminated by the KCRI WSR-88D (2995 MHz) is possible with no modifications. A multistatic network capable of operating with multiple monostatic illuminators would be able to change bistatic geometries in an adaptable manner if each site is limited to one receiver, or could operate in a true multistatic manner if each site has a receiver for each monostatic illuminator, both of which would further enhance the retrieval capabilities of such a network. Furthermore, a slight modification to the receiving antennae to an operating frequency around 2700 MHz would allow for illumination by the Advanced Technology Demonstrator, a S-band PAWR adjacent

to KCRI, as well as KOUN, the testbed polarimetric WSR-88D operated by the National Severe Storms Laboratory. This could allow for demonstrations of sidelobe whitening techniques coupled with rapid-scan strategies optimized for a multistatic network. The ARRC's Horus radar, an upcoming all-digital polarimetric mobile PAWR, will also be used for multistatic studies. It is still unknown how certain scanning strategies unique to PAWRs (imaging, beam multiplexing, etc.) would impact multistatic observations, so studies through simulations and real-world testing will be needed.

At the same time, the development and deployment of another set of similar receivers operating at X-band frequencies is anticipated. It is envisioned that these receivers will be mobile, allowing for use with the ARRC's mobile X-band radar systems (RaXPol, PX-1000, and PX-10k). Observations with these systems could include some of the first-ever bistatic dual-Doppler observations of high-impact weather phenomena like tornadoes. Further exploration into detection of turbulent clear-air scattering could be done at frequencies ranging from S- to X-band based on the results of Tulu et al. (2006), though antennae with higher gain would likely have to be employed. Aside from sidelobe whitening, the potential uses of a PAWR with a multistatic network are numerous. Adaptive beamforming on transmit (Nai et al., 2020) would yield the ability to control the amplitude and positioning of sidelobes. The use of a more sophisticated receiving antenna with element-level control could also allow for some form of 1D beamforming, akin to that used in Isom et al. (2013).

Another parallel effort will be to make these and future multistatic systems capable of polarimetric observations, which could open new avenues of microphysical retrievals by utilizing previously unheralded bistatic polarimetric moments and the multiple viewing angles of a multistatic network. Even in a minimal case, a polari-

metric multistatic network should be readily capable of differentiation between rain and hail (Aydin et al., 1998). Any microphysical retrievals would dovetail nicely with established 3D wind retrievals, yielding a system capable of rapid contemporaneous dynamical and microphysical measurements with a remarkably low-unit cost and ease of operation. With enough receivers, attempts at exotic techniques like multistatic radar tomography (Tran et al., 2018) could be undertaken, leveraging the considerable attenuation characteristics of X-band systems. The computation of bistatic dual-polarimetric spectral densities (DPSDs) could allow for discrimination of signal constituents (Bachmann and Zrnić, 2007; Umeyama et al., 2017; Wang et al., 2019), potentially creating a novel method of reducing sidelobe contamination.

Finally, these products and retrievals will require accompanying simulations to be properly understood and validated. Thus, further development of the multistatic simulator to polarimetric capabilities will be undertaken. In addition, experimental validation of the current network's multistatic retrievals will be attempted via rapid-scan observations and zenith scans, giving a better observational constraint on the horizontal and, most importantly, the vertical wind field. The hope is that a true quantitative assessment of the multistatic retrievals coupled with a substantial amount of observed cases will firmly cement the multistatic method as an effective, low-cost avenue of obtaining three-dimensional wind data.

## Bibliography

Atlas, D., K. Naito, and R. E. Carbone, 1968: Bistatic Microwave Probing of a Refractively Perturbed Clear Atmosphere. *Journal of the Atmospheric Sciences*, **25**, 257–268.

Aydin, K., S. H. Park, and T. M. Walsh, 1998: Bistatic Dual-Polarization Scattering from Rain and Hail at S-and C-Band Frequencies. *Journal of Atmospheric and Oceanic Technology*, **15**, 1110–1121.

Bachmann, S. M. and D. Zrnić, 2007: Spectral Density of Polarimetric Variables Separating Biological Scatterers in the VAD Display. *Journal of Atmospheric and Oceanic Technology*, **24**, 1186–1198, doi:10.1175/JTECH2043.1.

Boettcher, J. B. and E. S. Bentley, 2022: WSR-88D Sidelobe Contamination: From a Conceptual Model to Diagnostic Strategies for Improving NWS Warning Performance. *Weather and Forecasting*, doi:10.1175/WAF-D-21-0155.1.

Bohren, C. F. and L. J. Battan, 1982: Radar Backscattering of Microwaves by Spongy Ice Spheres. *Journal of the Atmospheric Sciences*, **39**, 2623–2628.

Brook, J. P., A. Protat, J. Soderholm, J. T. Carlin, H. McGowan, and R. A. Warren, 2021: HailTrack—Improving Radar-Based Hailfall Estimates by Modeling Hail Trajectories. *Journal of Applied Meteorology and Climatology*, **60**, 237–254, doi:10.1175/JAMC-D-20-0087.1.

Bryan, G. H. and J. M. Fritsch, 2002: A Benchmark Simulation for Moist Nonhydrostatic Numerical Models. *Monthly Weather Review*, **130**, 2917–2928.

Byrd, A., 2020: Multistatic Passive Weather Radar. Ph.D. thesis, University of Oklahoma.

Byrd, A. D., I. R. Ivić, R. D. Palmer, B. M. Isom, B. L. Cheong, A. D. Schenkman, and M. Xue, 2016: A Weather Radar Simulator for the Evaluation of Polarimetric Phased Array Performance. *IEEE Transactions on Geoscience and Remote Sensing*, **54**, 4178–4189, doi:10.1109/TGRS.2016.2538179.

Byrd, A. D., R. D. Palmer, and C. J. Fulton, 2020: Development of a Low-Cost Multistatic Passive Weather Radar Network. *IEEE Transactions on Geoscience and Remote Sensing*, **58**, 2796–2808, doi:10.1109/TGRS.2019.2955606.

Cheong, B. L., R. Kelley, R. D. Palmer, Y. Zhang, M. Yeary, and T. Y. Yu, 2013: PX-1000: A Solid-state Polarimetric X-Band Weather Radar and Time-Frequency Multiplexed Waveform for Blind Range Mitigation. *IEEE Transactions on Instrumentation and Measurement*, **62**, 3064–3072, doi:10.1109/TIM.2013.2270046.

Chong, M., N. Lamrani, and M. Hagen, 2008: A Variational Correction Method as an Alternative to Forced Rejection of Sidelobe-contaminated Bistatic Doppler Measurements. *Journal of Atmospheric and Oceanic Technology*, **25**, 1939–1954, doi:10.1175/2008JTECHA1117.1.

Crane, R. K., 1974: Bistatic Scatter From Rain. *IEEE Transactions on Antennas and Propagation*, **22**, 312–320, doi:10.1109/TAP.1974.1140766.

de Elia, R., 2000: Performance Study of a Bistatic Radar Network.

Ph.D. thesis, McGill University, 156 pp., URL https://login.ezproxy.lib.ou.edu/login?url=https://www.proquest.com/dissertations-theses/performance-study-bistatic-radar-network/docview/304660146/se-2?accountid=12964.

de Elía, R. and I. Zawadzki, 2000: Sidelobe Contamination in Bistatic Radars. *Journal of Atmospheric and Oceanic Technology*, **17**, 1313–1329.

de Elía, R. and I. Zawadzki, 2001: Optimal Layout of a Bistatic Radar Network. *Journal of Atmospheric and Oceanic Technology*, **18**, 1184–1194.

Dibbern, J., 1987: Dependence of Radar Parameters on Polarization Properties of Rain for Bistatic CW Radar. *Radio Science*, **22 (05)**, 769–779, doi:10.1029/RS022i005p00769.

Doherty, L. H., 1964: Z-R Relationships Deduced from Forward Scatter Doppler Measurements. *Journal of the Atmospheric Sciences*, **21**, 683–697.

Doviak, R. J., J. Goldhirsh, and A. R. Miller, 1972: Bistatic-Radar Detection of High-altitude Clear-air Atmospheric Targets. *Radio Science*, **7 (11)**, 993–1003, doi:10.1029/RS007i011p00993.

Doviak, R. J. and C. M. Weil, 1972: Bistatic Radar Detection of the Melting Layer. *Journal of Applied Meteorology and Climatology*, **11**, 1012–1016.

Doviak, R. J. and D. S. Zrnić, 1993: *Doppler Radar and Weather Observations*. Elsevier, doi:10.1016/C2009-0-22358-0.

Feng, Y. C. and F. Fabry, 2016: The Imperfect Phase Pattern of Real Parabolic Radar Antenna and Data Quality. *Journal of Atmospheric and Oceanic Technology*, **33**, 2655–2661, doi:10.1175/JTECH-D-16-0143.1.

Friedrich, K. and O. Caumont, 2003: Dealiasing Doppler Velocities Measured by a Bistatic Radar Network during a Downburst-Producing Thunderstorm. *Journal of Atmospheric and Oceanic Technology*, **21**, 717–729.

George, J., D. Brunkow, and V. Chandrasekar, 2006: Networking CSU-CHILL and CSU-Pawnee to Form a Bistatic Radar System. *International Geoscience and Remote Sensing Symposium (IGARSS)*, Institute of Electrical and Electronics Engineers Inc., 660–663, doi:10.1109/IGARSS.2006.172.

Hagen, M., P. Meischner, J. Wurman, M. Randall, and C. Burghart, 1999: A C-Band Bistatic Doppler Radar System At DLR Oberpfaffenhofen. *29th International Conference on Radar Meteorology*, American Meteorological Society, 813–814.

Helmus, J. J. and S. M. Collis, 2016: The Python ARM Radar Toolkit (Py-ART), a Library for Working with Weather Radar Data in the Python Programming Language. *Journal of Open Research Software*, **4**, doi:10.5334/jors.119.

Isom, B., et al., 2013: The Atmospheric Imaging Radar: Simultaneous Volumetric Observations Using a Phased Array Weather Radar. *Journal of Atmospheric and Oceanic Technology*, **30**, 655–675, doi:10.1175/jtech-d-12-00063.1.

Jackson, R., S. Collis, T. Lang, C. Potvin, and T. Munson, 2020: Py-DDA: A Pythonic Direct Data Assimilation framework for wind retrievals. Zenodo, URL https://doi.org/10.5281/zenodo.3942686, doi:10.5281/zenodo.3942686, URL https://doi.org/10.5281/zenodo.3942686.

Kumjian, M. R., Y. P. Richardson, T. Meyer, K. A. Kosiba, and J. Wurman, 2018: Resonance Scattering Effects in Wet Hail Observed with a Dual-X-Band-Frequency, Dual-Polarization Doppler on Wheels Radar. *Journal of Applied*

*Meteorology and Climatology*, **57**, 2713–2731, doi:10.1175/JAMC-D-17, URL https://doi.org/10.1175/JAMC-D-17-.

Leinonen, J., 2014: High-level Interface to T-matrix Scattering Calculations: Architecture, Capabilities and Limitations. *Opt. Express*, **22 (2)**, 1655–1660, doi:10.1364/OE.22.001655, URL http://opg.optica.org/oe/abstract.cfm?URI=oe-22-2-1655.

Mueller, E. A., 1977: Statistics of High Radar Reflectivity Gradients. *Journal of Applied Meteorology*, **16**, 511–513.

Nai, F., J. Boettcher, C. Curtis, D. Schvartzman, and S. Torres, 2020: The Impact of Elevation Sidelobe Contamination on Radar Data Quality for Operational Interpretation. *Journal of Applied Meteorology and Climatology*, **59**, 707–724, doi:10.1175/JAMC-D-19-0092.1.

Nakagawa, K., H. Hanado, S. Satoh, and T. Iguchi, 2002: Development of the CRL Okinawa Bistatic Polarimetric Radar. *Communications Research Laboratory Review*, **48 (2)**, 203–209.

Nishimura, K., E. Gotoh, and T. Sato, 2006: Fine Scale 3D Wind Field Observation With a Multistatic Equatorial Atmosphere Radar. *Journal of the Meteorological Society of Japan*, **84**, 227–238.

Protat, A. and I. Zawadzki, 1999: A Variational Method for Real-Time Retrieval of Three-Dimensional Wind Field from Multiple-Doppler Bistatic Radar Network Data. *Journal of Atmospheric and Oceanic Technology*, **16**, 432–449.

Ray, P. S. and K. L. Sangren, 1983: Multiple-Doppler Radar Network Design. *Journal of Climate and Applied Meteorology*, **22**, 1444–1454.

ROC, 2021: *Interface Control Document for the RDA/RPG*.

Sachidananda, M., R. J. Doviak, and D. S. Zrnić, 1985: Whitening of Sidelobe Powers by Pattern Switching in Radar Array Antenna. *IEEE Transactions on Antennas and Propagation*, **33**, 727–735, doi:10.1109/TAP.1985.1143661.

Sachidananda, M. and D. S. Zrnic, 1999: Systematic Phase Codes for Resolving Range Overlaid Signals in a Doppler Weather Radar. *Journal of Atmospheric and Oceanic Technology*, **16**, 1351–1363.

Shedd, L., M. R. Kumjian, I. Giammanco, T. Brown-Giammanco, and B. R. Maiden, 2021: Hailstone Shapes. *Journal of the Atmospheric Sciences*, **78**, 639–652, doi:10.1175/JAS-D-20-0250.1.

Soh, H. S., S. Y. Kim, P. M. Kosro, and A. L. Kurapov, 2018: Do Nonorthogonally and Irregularly Sampled Scalar Velocities Contain Sufficient Information to Reconstruct an Orthogonal Vector Current Field? *Journal of Atmospheric and Oceanic Technology*, **35**, 763–795, doi:10.1175/JTECH-D-17-0062.1.

Takaya, Y. and M. Nakazato, 2002: Error Estimation of the Synthesized Two-Dimensional Horizontal Velocity in a Bistatic Doppler Radar System. *Journal of Atmospheric and Oceanic Technology*, **19**, 74–79.

Takaya, Y. and M. Nakazato, 2003: Anisotropic Error Distributions in a Bistatic Doppler Radar System. *Journal of Atmospheric and Oceanic Technology*, **20**, 833–844.

Testud, J. and M. Chong, 1983: Three-Dimensional Wind Field Analysis from Dual-Doppler Radar Data. Part I: Filtering, Interpolating and Differentiating the Raw Data. *Journal of Applied Meteorology and Climatology*, **22**, 1204–1215.

Tran, H.-T., E. Heading, and B. Ng, 2018: Multi-Bistatic Doppler Radar Tomography for Non-Cooperative Target Imaging. *2018 International Conference on Radar (RADAR)*, 1–6, doi:10.1109/RADAR.2018.8557242.

Tulu, Z. C., S. J. Frasier, R. Janaswamy, and D. J. McLaughlin, 2006: Considerations for Bistatic Probing of Clear-air Winds in the Atmospheric Boundary Layer. *Radio Science*, **41**, doi:10.1029/2005RS003293.

Umeyama, A. Y., S. M. Torres, and B. L. Cheong, 2017: Bootstrap Dual-Polarimetric Spectral Density Estimator. *IEEE Transactions on Geoscience and Remote Sensing*, **55**, 2299–2312, doi:10.1109/TGRS.2016.2641385.

Wang, Y., T. Y. Yu, A. V. Ryzhkov, and M. R. Kumjian, 2019: Application of Spectral Polarimetry to a Hailstorm at Low Elevation Angle. *Journal of Atmospheric and Oceanic Technology*, **36**, 567–583, doi:10.1175/JTECH-D-18-0115.1.

Waterman, P., 1965: Matrix Formulation of Electromagnetic Scattering. *Proceedings of the IEEE*, **53 (8)**, 805–812, doi:10.1109/PROC.1965.4058.

Wurman, J., 1994: Vector Winds from a Single-Transmitter Bistatic Dual-Doppler Radar Network. *Bulletin of the American Meteorological Society*, **75**, 983–994.

Wurman, J., S. Heckman, and D. Boccippio, 1993: A Bistatic Multiple-Doppler Radar Network. *Journal of Applied Meteorology and Climatology*, **32**, 1802–1814.

Wurman, J., M. Randall, and C. Burghart, 2001: Bistatic Radar Networks. *30th International Conference on Radar Meteorology*, 130–133.

Wurman, J., M. Randall, C. L. Frush, E. Loew, and C. L. Holloway, 1994: Design of a Bistatic Dual-Doppler Radar for Retrieving Vector Winds Using One Trans-

mitter and a Remote Low-Gain Passive Receiver. *Proceedings of the IEEE*, **82**, 1861–1872, doi:10.1109/5.338075.